ISSN 2738-0971
eISSN 2738-1013

Bulletin of Natural Sciences Research

Vol. 11, Nº 1, 2021.

BULLETIN OF NATURAL SCIENCES RESEARCH

Published by
Faculty of Sciences and Mathematics, University of Priština in Kosovska Mitrovica
Republic of Serbia

Focus and Scope

Bulletin of Natural Sciences Research is an international, peer-reviewed, open access journal, published semiannually, both online and in print, by the Faculty of Sciences and Mathematics, University of Priština in Kosovska Mitrovica, Republic of Serbia. The Journal publishes articles on all aspects of research in biology, chemistry, geography, geoscience, astronomy, mathematics, computer science, mechanics and physics.

Technical Secretary

Danijel B. Đošić

Editorial Office

Ive Lole Ribara 29; 38220, Kosovska Mitrovica, Serbia, e-mail: editor@bulletinnsr.com, office@bulletinnsr.com; fax: +381 28 425 397

Printed by

Sigraf, Ćrila i Metodija bb, 37000 Kruševac, tel: +38137427704, e-mail: stamparijasigraf@gmail.com

Available Online

This journal is available online. Please visit http://www.bulletinnsr.com to search and download published articles.

BULLETIN OF NATURAL SCIENCES RESEARCH

Vol. 11, N^{o} 1, 2021.

CONTENTS

BIOLOGY

CHEMISTRY

Milenko Ristić, Biljana Dekić, Niko Radulović, Marija Aksić

SYNTHESIS, COMPLETE ASSIGNMENT OF 1H- AND 13C-NMR SPECTRA AND ANTIOXIDANT ACTIVITY OF NEW AZINE DERIVATIVE BEARING COUMARIN MOIETY ….....…. 9-16

Danijela Ilić Komatina, Aleksandra Minić Jančić, Jovana Bugarinović, Dragana Stevanović

THE PREPARATION AND CHARACTERIZATION OF SOME NOVEL FEROCENIL DERIVATIVES .....…….....…….....….....….....

MATHEMATICS, COMPUTER SCIENCE AND MECHANICS

PHYSICS

Bulletin of Natural Sciences Research
Vol. 11, No. 1, 2021, pp. 1-5.

DOI: https://doi.org/10.5937/bnsr11-24644
Original Scientific Paper

PHARMACEUTICALS AND ENDOCRINE-DISRUPTING COMPOUNDS: ACCUMULATION IN THE TISSUE OF SKADAR LAKE FISH

DRAŽANA RADONJIĆ[1]

[1]Biology Department, Faculty of Natural Sciences and Mathematics, University of Montenegro, Podgorica, Montenegro

ABSTRACT

Determining the presence of pharmaceuticals and endocrine-disrupting compounds in fish tissues has been carried out in Montenegro for the first time in Moraca river and Skadar lake. Skadar lake, Montenegro, is the largest of the Balkan lakes and has a surface area which fluctuates seasonally from approximately 370 to 600 km2. During the spring time of 2016, in the time of high water levels of the lake, fish were fetched in triplets and identified. Determining the presence of pharmaceuticals and endocrine-disrupting compounds in fish tissues has been carried out in Montenegro for the first time. Their muscle tissue was separated, grinded, feezed, and then lyophilized. Prepared samples were analyzed with liquid chromatography coupled to tandem mass spectrometry to determine the presence of pharmaceuticals and endocrine-disrupting compounds. Obtained results are under the border of detection, out of 38 tested distributes, only the tissue of *Alburnus scoranza* showed the presence of triclosan.

Keywords: Endocrine-disrupting compounds, Lyophilized, Liquid chromatography coupled to tandem mass spectrometry, *Alburnus scoranza*, Triclosan.

INTRODUCTION

In recent years, potential risks associated with the release of Endocrine Disrupting Compounds (EDCs) into the aquatic environment have become an increasingly important issue for environmental regulators. Several investigations have shown that the substances of pharmaceutical origins are often not eliminated during wastewater treament, and are not biodegradable as well (Ternes, 1998; Daughton et al., 1999; Zwiener et al., 2004). Due to the conservative nature of physiological processes, chemicals affect several aquatic species (e.g. algae, invertabrate and fish) in a manner similar to their affect on humans due to comparable target molecules (Fent et al., 2006). Many contaminants have been detected in wastewater effluents and surface waters in recent years, including pharmaceuticals (PhACs) and (EDCs). Many of these compounds are not completely removed in the wastewater treatment plants (WWTPs) and are released to the environment (Gros et al., 2009). EDCs are designed to modify physiological or biochemical functions in target organisms but can have severe consequences when non-target organisms are under their exposure.

Better understanding of how these compounds are transferred from water to the biota could help to determine potential ecosystem damage associated with the WWTP effluent discharge contaminants. It is generally accepted that substances with octanol-water partition coefficient (log KOW) values higher than or equal to 3 have the potential to bioaccumulate in biological tissues. Many PhACs and EDCs have a log KOW < 3, and thus are not expected to bioaccumulate. However, some of these compounds are lipid soluble and therefore potentially bioaccumulative in the environment (Huerta et al., 2013) and fish tissue. Moreover, when considering bioaccumulation of PhACs and EDCs in aquatic organisms, one must take other factors into consideration, such as the different rates of metabolism in various organisms, how their metabolites accumulate, and the uptake and depuration kinetics.

Situated along the Montenegro-Albanian border, Lake Skadar is the largest lake of the Balkan Peninsula with unique characteristics, wide range of endemic and rare or endagered plant and animal species, recognized as a wetland site of international significance according to the RAMSAR Convention (2002). In spite of its importance, inflowing waters from the Moraca river and other regional rivers contaminated by the industry, municipal and agricultural activities in the area influence the Lake. Therefore, the Lake has been the subject of various physical, chemical, biological and toxicological examinations (Beeton & Karaman, 1981; Rastall et al., 2004; Rakocevic-Nedovic & Hollert, 2005; Stesevic et al., 2007; Perovic et al., 2012; Kastratovic et al., 2014; Vemic et al., 2014; Petrovic et al., 2016, Perovic et al., 2019). In this study, we assessed the level of bioaccumulation of ECDs and PhACs in aquatic organisms (fish tissues) *Rutilus prespensis* (Karaman, 1924), *Squalius platyceps* (Zupancic et al., 2010), *Scardinius knezevici* (Bianco & Kottelat, 2005), *Chondrostoma ohriadunum* (Karaman, 1924), *Cyprinus carpio* (Linnaeus, 1758) and *Alburnus scoranza* (Bonaparte, 1845).

* Corresponding author: i.radonjic99@gmail.com

EXPERIMENTAL

Area of study and sampling

The research location belongs to the area of Skadar lake and its tributaries. Locations are marked on the Figure 1.

Figure 1. Map of Lake Skadar with sampling locations.

Lake Skadar is the largest lake on the Balkan Pninsula. It is located in karst area on the Montenegro-Albanian border and covers the surface from approximately 370 to 600 km2, depending on seasonal fluctations. This area is classified as an internationally important RAMSAR site (Lake Skadar, Site, 3YU003, Ramsar Convention 2002) and promoted as a National Park IUCN Category II. In spite of its importance, inflowing waters from the Moraca River and other regional rivers contaminated by the industry, municipal and agricultural activities in the area affect the lake. River Moraca (Mediterranean basin), near the town Podgorica, is relatively intact but still receives the treatment of waste water discharge, produced by 300,000 citizens. River Moraca emerges at the topographic point of 975 m above the creeks which disembogue under the Javorje and Zebalci slopes, with largest of them being Javor and Rzav creeks. River Moraca is 113 km long, which makes in the longest river in Montenegro. The researched locations with the coordinates.

Vukovci 42°20′ 02″N; 19° 11′ 60″ E, ”Left branch of river Moraca“ 42°25′84″ N; 19°13′ 46″E ”Right branch of river Moraca“ 42°27′70″ N; 19°12′ 32″ E ”Kraljeva glavica“-Vranjina 42° 27′ 57″ N; 19° 12′ 15″E ”Tanki rt“- Under the bridge 42° 27′ 90″ N, 19° 13′ 49″ E.

Throughout decades, this locality has been under the influence of industrial waters originating from Kombinat Aluminijuma (CAP) and Machine Factory ”Radoje Dakić“. Therefore, all researches were conductedin order to determine the concentration of PCB, aluminium, heavy metals and oil in water, land and biota. However, this industry slowly stoped working during the 90s. Podgorica and its surroundings make up for more than a half of the population of Montenegro. Therefore, waste waters are seen as the main pollutants of river Moraca.

Animals and experimental design

Samples were fetched in triplets using fishnets in spring of 2016, during the time of high water level of the lake, we separated musscle tissues and repeated the process 3 times, grinded them separatekt in a hand blender, put them into special sample boxes and froze them. Two days later, they were transported to the Marine Institute of Montenegro where they were lyophilized.

Sample purification optimization

Fish homogenate extracts were spiked with a mixture of the target analytes and a comparison was made between three purification techniques: SPE Florisil cartridges (1 g, 6 ml cartridges), Gel permeation chromatography (GPC) in an Agilent 1260 Infinity high pressure liquid chromatography system in tandem with a diode array detector (HPLC-DAD), SPE Oasis HLB (200 mg, 6 ml cartridges) followed by GPC. For the clean-up method based on SPE Florisil, fish extracts were redissolved in 10 ml of acetonitrile prior SPE, which was performed in a J.T.Baker® system.

Liquid chromatography and mass spectrometry analysis

The cromatographic tandem mass spectrometry method applied for the analysis of fish extracts was adapted from Gros et al. (2009). Briefly, chromatographic separations were carried out with a Waters Acquity Ultra-PerformanceTM liquid chromatography system, using an Acquity HSS T3 column (50 mm×2.1mm i.d., 1.8_m particle size) for the compounds analyzed in positive electrospray ionization (PI) mode and Acquity BEH C18 column (50 mm×2.1mm i.d., 1.7_m particle size) for the ones analyzed under negative electrospray ionization (NI) mode. For the analysis in PI mode, separation conditions were as follows: solvent (A) methanol, solvent (B) 10mM formic acid/ammonium format (pH 3.2) at a flow rate of 0.5 mL/min. The analysis in NI mode was performed by using acetonitrile (A) and (B) 5mM ammonium acetate/ammonia (ph=8) at a flow rate of 0.6 mL/min. The sample volume injected was 5_L in both cases. The UPLC instrument was coupled to a 5500 OTRAP hybrid triple quadrupole-linear ion trap mass spectrometer (Applied Biosystems).; nitrogen collision gas (CAD) medium; source gases GS1 and GS2 were set at 60 and 50 psi, respectively. Besides the monitoring of the SRM transitions, the relative abundance of the two SRM transitions in the sample were compared with those in the standards, and the relative abundances in the samples must be within ±20% of the two SRM ratios in the analytical standards. Prepared samples were sent to Catalan Institute for Water Research (ICRA)-Gerona in order to determine the existence of certain EmS and EDCs in the fish tissues using the (Huerta et al., 2012) and (Huerta et al., 2013) method.

NUMERICAL RESULTS

Occurrence of PhACs and EDCs in freshwater fish is presented in table 1**.**

Obtained results are under the border of detection, or in the frames of the method detection and quantification limits (MLD, MQL). Out of 38 tested distributes, only one (triclosan) was founds in the muscle tissue of *Alburnus scoranca* in concentration 14,1±1,2 ng/g (Table 1).

Triclosan phenol, are commonly used commercial microbicides found in toothpastes and soaps. Triclosan (is widely used as an antibacterial agent in various industrial products, such as textile goods, soap, shampoo, liquid toothpaste and cosmetics, and often detected in wastewater effluent. However, there is a paucity of data on the toxicity of triclosan and its effects on aquatic organisms. For example, (Tatarazako et al., 2004) in his observation found that concentration of fish (*Danio rerio* and *Oryzias latipes)* was from 0.07 to 0.29 mg/l. Other scientists have studied the toxicity of triclosan too, especially because of its wide spread in chemical industry. For example, Ximei et al. (2013), researched assessment of toxic effects of triclosan on swordtail fish (*Xipophorus helleri*) using a multi-biomarker approach. Another example is the research of triclosan in Fresh Water Fish Gibelion Catla from the Kaveri River, India, and its Consumption Risk Assessment (Govindarej et al., 2014).

Of note, while fish can be exposed to higher levels of triclosan from their surroundings, algae and invertebrates are often considered more sensitive Chalew & Halden (2009). A number of different aquatic toxicity thresholds for triclosan are available in the literature. Colgate-Palmolive scientists used an unconventional method to develop a PNEC of 1,550ng/L (Capdevielle et al., 2008). In contrast, a more traditional and conservative method based on acute algal toxicity has led to the use of PNEC of 4.7 ng/L (e.g., von der Ohe et al., 2000). Should the latter threshold be considered more appropriate for San Francisco Bay, the few recent ambient Bay surface water measurements available (up to 68±26 ng/L) may suggest cause for concern. However, existing data are too few to trigger reclassification of triclosan within the RMP's CEC risk and management action framework (Sutton et al., 2016). Until more data are generated, triclosan may remain classified as a low concern (Tier II) for San Francisco Bay.

Table 1. Occurrence of EDCs and PhACs in freshwater fish in Lake Skadar lake.

Sample name EDCs ng/g	*Rutilus prespensis*	*Squalius platyceps*	*Scardinius knezevici*	*Chondrostoma ohridanum*	*Ciprinus carpio*	*Alburnus scoranza*	MDL	MQL
Caffeine	<MDL	<MDL	<MDL	<MDL	<MDL	<MDL	0,3255	1,0849
Progesterone	<MDL	<MDL	<MDL	<MDL	<MDL	<MDL	0,0158	0,0526
Levonorgestrel	<MDL	<MDL	<MDL	<MDL	<MDL	<MDL	0,0002	0,0006
TCEP	<MDL	<MDL	<MDL	<MDL	<MDL	<MDL	0,25	0,84
TBEP	<MQL	<MQL	<MQL	<MQL	<MQL	<MQL	0,07	0,27
TCCP	<MQL	<MQL	<MQL	<MQL	<MQL	<MQL	25,4	84,8
Estrone	<MDL	<MDL	<MDL	<MDL	<MDL	<MDL	0,003	0,0099
17β-Estradiol	<MDL	<MDL	<MDL	<MDL	<MDL	<MDL	0,01	0,05
Estriol	<MDL	<MDL	<MDL	<MDL	<MDL	<MDL	0,0002	0,0007
17-α-Ethinylestradiol	<MDL	<MDL	<MDL	<MDL	<MDL	<MDL	0,0004	0,0014
Estrone-3-sulfate	<MDL	<MDL	<MDL	<MDL	<MDL	<MDL	0,0007	0,0022
Bisphenol A	<MQL	<MQL	<MQL	<MQL	<MQL	<MQL	0,02	0,07
Triclosan	<MQL	<MQL	<MQL	<MQL	<MQL	14,1±1,3	0,0018	0,0061
Methylparaben	<MDL	<MDL	<MDL	<MDL	<MDL	<MDL	0,01	0,03

Sample name PhACs ng/g	*Rutilus prespensis*	*Squaliusplatyceps*	*Scardinius knezevici*	*Chondrostomaohridanum*	*Ciprinus carpio*	*Alburnus scoranza*	MDL	MQL
Atenolol	<MDL	<MDL	<MDL	<MDL	<MDL	<MDL	0,01	0,02
Carazolol	<MDL	<MDL	<MDL	<MDL	<MDL	<MDL	0,01	0,02
Metropolol	<MQL	<MDL	<MQL	<MDL	<MQL	<MQL	0,1	0,35
Nadolol	<MQL	<MQL	<MQL	<MQL	<MQL	<MQL	0,31	1,04
Propanolol	<MDL	<MDL	<MQL	<MQL	<MQL	<MQL	0,09	0,29
Sotalol	<MDL	<MDL	<MDL	<MDL	<MDL	<MDL	0,08	0,26
Carbamazepine	<MDL	<MDL	<MDL	<MDL	<MDL	<MDL	0,05	0,17
Citalopram	<MDL	<MDL	<MDL	<MDL	<MDL	<MDL	0,12	0,4
Diazepam	<MDL	<MDL	<MQL	<MDL	<MDL	<MDL	0,03	0,1
10,11-EpoxyCBZ	<MDL	<MDL	<MQL	<MDL	<MQL	<MDL	0,02	0,05
2-HydroxyCBZ	<MDL	<MDL	<MDL	<MDL	<MDL	<MDL	0,01	0,03
Lorazepam	<MDL	<MDL	<MDL	<MDL	<MDL	<MDL	0,06	0,2
Sertraline	<MDL	<MDL	<MDL	<MDL	<MDL	<MDL	0,25	0,83
Venlafaxine	<MDL	<MDL	<MDL	<MDL	<MDL	<MDL	0,01	0,03
Clopidrogel	<MDL	<MDL	<MDL	<MDL	<MDL	<MDL	0,01	0,04
Codeine	<MDL	<MDL	<MDL	<MDL	<MDL	<MDL	0,02	0,06
Levamisole	<MDL	<MDL	<MDL	<MDL	<MDL	<MDL	0,02	0,05
Salbutamol	<MDL	<MDL	<MDL	<MDL	<MDL	<MDL	0,01	0,04
Diclofenac	<MDL	<MDL	<MDL	<MDL	<MDL	<MDL	1,73	5,77
Hydrochlorothiazide	<MDL	<MDL	<MDL	<MDL	<MDL	<MDL	0,01	0,02

CONCLUSION

After the detailed research of PhACs and EDCs in the fish tissues (Rutilus prespensis, Squalius platyceps, Scardinius knezevici, Chondrostoma ohridanum, Cyprinu scarpio and Alburnus scoranza) it is determined that the concentration of researched distributors are found in MDL and MQL. Examined fish are a part of Skadar lake fauna, and are typical representatives. Economically, they are the most important fish. Exception to this research is detected concentration of triclosan (14,1±1,3 ng/g) in the tissue of fish Alburnus scoranza. It is considered that the specific habitat and diet of this fish caused these results in its muscle tissue. Further detailed research is needed to establish the source of the PhACs and EDCs.

REFERENCES

Bianco, P. G. & Kottelat, M. 2005. Scardiniusknezevici, a new species of rudd from Lake Skadar, Montenegro (Teleostei: Cyprinidae). Ichtyol. Explor. Freshwat.

Bonaparte, C. L. 1841. *Aspius alburnus (aspius alborella)* – In Iconografiadella fauna italica Pesci, Salvucci.

Beeton, A. M. & Karaman, G. 1981.The biota and limnology of Lake Skadar. Titograd GRO Prosveta, Beograd.

Brooks, B. W. 2005. Determination of select antidepressants in fish from an effluent-dominated stream. Environ Toxicol Chem.

Deighton, C. G. & Ternes, T. A. 1999. Pharmaceuticals and personal care products in the environment: Agents of subtle change? Environmental Health Perspectives.

Capdevielle, M, Egmond, R. V., Whelan, M., Versteeg, D., Hofmann-Kamensky, M., Inauen,J., Cunningham, V. & Voltering, D. 2008. Consideration of exposure and species sensitivity of triclosan in the freshwater environment. Integr Environ Assess Manag.

Chalew, T. E. A. & Halden, R. U. 2009. Environmental exposure of aquatic and terrestrial biota to triclosan and triclocarban. Journal of the American Water Resources Association (451).

Drecun, D. & Miranovic, M. 1962. Ulov ribe na Skadarskom jezeru 1947-1960 godine. Hydrobiologia Montenegrina.

Gros, M., Petrovic, M. & Barcelo, D. 2009. Tracing Pharmaceutical Residues of Different Therapeutic Classes in Environmental Waters by Using Liquid Chromatography/Quadrupole Linear Ion Trap Mass Spectrometry and Automated Library Searching. Analytical Chemistry.

Govindaraj, S., Karthik, R., Krishna, K., Selvaraj, S. S. & Babu, R. R. 2014. Triclosan in Fresh Water Fish Gibelion Catla from the Kaveri River, India, and Its Consumption Risk Assessment. Environmental Forensics Volume.

Karaman, S. 1924. Pisces Macedoniae. Split.

Kastratovic, V., Krivokapic, S., Bigovic, M., Djurovic, D. & Blagojevic, N. 2014. Bioaccumulation and translocation of heavy metals by Ceratophyllum demersum from Skadar Lake, Montenegro. J Serb Chem Soc.

Linnaeus, C. 1758. Systemanaturae per regna trianaturae, secundum classes, ordines, genera, species, cum characteribus, differentiis, synonymis, locis. Tomus I.

Fent, K., Weston, A. A. & Caminada, D. 2006. Ecotoxicology of human pharmaceuticals. Aquatic Toxicology.

Huerta, B., Jakimska, A., Gros, M., Rodriguez-Mozaz, S. & Barcelo, D. 2013. Analysis of multi-class pharmaceuticals in fish tissues by ultra-high-performance liquid chromatography tandem mass spectrometry. Journal of Chromatography A.

Huerta, B., Rodriguez-Mozaz, S. & Barcelo, D. 2012. Pharmaceuticals in biota in the aquatic environment: analytical methods and environmental implications. Anal BioanalChem.

Ohe, T., Hirobe, M. & Mashino, T. 2000. Novel metabolic pathway of estrone and 17b-estradiol catalyzed by cytochrome P-450. Drug Metab Dispos.

Perovic, A., Perovic, S., Erdinger, L. & Hollert, H. 2012. Assessment of genotoxic potential of the Lake Skadar sediments extracts using the comet assay with fish cell line RTL-W1 and Ames test. Arch BiolSci.

Petrovic, D., Jancic, D., Furdek, M., Mikac, N. & Krivokapic, S. 2016. Aquatic plant Trapanatans L. as bioindicator of trace metal contamination in a freshwater Lake (Skadar Lake, Montenegro).Acta Bot Croat.

Rastall, A. C., Neziri, A., Vukovic, Z., Jung, C., Mijovic, S., Hollert, H., Nikcevic, S. & Erdinger, L. 2004. The identification of readily bioavailable pollutions in Lake Shkodra/Skadar using Semipermeable membrane devices (SPMDs), bioassays and chemical analysis. Environ SciPollut Res Skadarsko jezero (Site 3YU003) In: A directory of wetlands of International importance 2002. The Ramsar Convention Bureau. Gland, Switzerland.

Rakocevic-Nedovic, J. & Hollert, H. 2005. Phytoplankton community and chlorophyll a as trophic state indices of Lake Skadar (Montenegro, Balkan). Environ SciPollut Res.

Stesevic, D., Feiler, U., Sundic, D., Mijovic, S., Erdinger, L., Seiler, T. B., Heininger, P. & Hollert, H. 2007. Application of a new sediment contact test with Myriophyllum aquaticum and of the aquatic Lemna test to assess the sediment quality of Lake Skadar.J Soils Sediments.

Sutton, R., Mason, S. A., Stanek, S. K., Willis-Norton, E., Wren, I. F. & Box, C. 2016. Microplastic contamination in the San Francisco Bay, California, USA.Mar Pollut Bull.

Tatarazako, N., Ishibashi, H., Teshima, K., Kishi, K. & Arizono, K. 2004. Effects of triclosan on various aquatic organisms. Environ Sci.

Ternes, T. A. 1998. Occurrence of drugs in German sewage treatment plants and rivers. Water Research.

Ximei, L., Xiangping, N., Guangguo, Y., Taicheng, A. & Kaibing, L. 2013. Assessment of toxic effects of triclosan on the swordtail fish (*Xiphophorus helleri*) by a multi-biomarker approach.Chemosphere.

Zupancic, P., Maric, D., Naseka, A. M. & Bogutskaya, N. G. 2010. Squalius platyceps, a new species of fish (*Actinopterygii*: *Cyprinidae*) from the Skadar Lake basin. Zoosystematica Rossica.

Zwiener, C. & Frimmel, F. 2004. LC-MS analysis in the aquatic environment and in water treatment - a critical review - Part I: Instrumentation and general aspects of analysis and detection. Analytical and Bioanalytical Chemistry.

Vemic, M., Rousseau, D., Laing, G. D. & Lens, P. 2014. Distribution and fate of metals in the Montenegrin part of Lake Skadar. Int J Sediment Res.

Bulletin of Natural Sciences Research
Vol.11, No.1, 2021, pp. 6-8.

DOI: https://doi.org/10.5937/bnsr11-28412
Original Scientific Paper

NEW DATA ON SOME MOTH SPECIES (LEPIDOPTERA) FROM MT. JADOVNIK AND MILEŠEVKA RIVER CANYON (WEST SERBIA)

PREDRAG JAKŠIĆ[1]⋆, ANDREW KING[2]

[1]Faculty of Natural Sciences and Mathematics, University of Priština, Kosovska Mitrovica, Serbia
[2]Grovewood Close 18, Chorleywood, Hertfordshire, WD3 5PU, United Kingdom

ABSTRACT

Data on six species of Lepidoptera significant for the fauna of Serbia, as the data on one quite rare species in Serbian fauna are presented.

Keywords: Lepidoptera, West Serbia.

INTRODUCTION

The Lepidopteran fauna of in Serbia is insufficiently known. This is especially true of the fauna of the microlepidoptera. In terms of the number of identified species, Serbia lags significantly behind neighboring countries. As far as we are aware, there is no organized and systematic research being undertaken by academic or similar institutions. Fragmentary data come mostly from foreign authors. Some domestic authors act together in NGOs, or independently. Their results are relatively modest, but still significant. Recently organized studying Lepidoptera in the region has been created as "Balkans Moths Project" by several scientists. Some of the results contain numerous new data on Lepidoptera of Serbia published in Plant et al. (2017) and Beshkov et al. (2020). As the part of this project, monograph on butterflies of Mt. Jadovnik will be published soon (Jakšić (2020), in print). The aim of this paper is to add new data on several species rare in western Serbia.

MATERIAL AND METHODS

Moths were sampled at light during night using a white sheet illuminated by 125 W Hg-Li mercury bulb. The species are listed according to their relevant families, according to Zhi-Qiang Zhang (2011).

Fieldwork in protected areas was undertaken in agreement with permits provided by the Ministry of Environment, Mining and Spatial Planning, Republic of Serbia, No. 353-01-1559 dated on 8.6.2011; 353-01-1070, dated on 12.6.2012; 353-01-637/2013-08 dated on 10.6.2013 and 353-01-916/2014-08 dated on 29.5.2014.; 353-01-356/2015-17 dated on 27.04.2015.; 353-01-389/2016-17 dated on 08.4. 2016. and 353-01-763/2019. 04 dated on 23.05.2019.

Photos of *in situ* specimen were taken by the second author, using a "Nikon D-3200" camera. All the material (specimens and genitalia slides) is deposited in the collection of P. Jakšić in Belgrade (CPJB).

RESULTS

Six species belonging to five families are presented in this paper.

Fam. Hepialidae Stephens, 1829

Korscheltellus lupulina (Linnaeus, 1758)

New data: Sopotnica village, 986 m, 2 males, 1 June 2014, Genitalia checked, slides SR-2641 and SR-2652; Kašanj village, 1276 m, 1 female, 8 June 2016.

Literature data for Serbia: Abafi-Aigner (1910), Beshkov (2017), Kereši & Almaši (2017), Tot et al. (2018).

A moth of grassland. The subterranean larvae feed on the roots of grasses and herbaceous plants.

Figure 1. *Nemophora degeerella* complex Sopotnica village, 986 m, 26 June 2016.

Fam. Adelidae Bruand, 1851

Nemophora degeerella complex

⋆ Corresponding author: jaksicpredrag@gmail.com

New data: Sopotnica village, 986 m, 26 June 2016, (Fig. 1).

Literature data for Serbia: Rebel (1911), Rebel (1914), Rebel (1917), Rebel & Zerny (1931), Rotschild (1912-1917), Szent-Ivany (1945), Zečević (2002).

A moth of open woodland and scrub. The males form leks 'dancing' aerially beside bushes in the sunshine. The larvae initially feed on various flowers and then build portable cases and move around on the ground, feeding on dead vegetation.

Figure 2. *Cnaemidophorus rhododactyla* (Denis Schiffermüller, 1775) Mileševka Canyon, 585 m, 14 June 2016.

Fam. Pterophoridae Latreille, 1802

Cnaemidophorus rhododactyla (Denis & Schiffermüller, 1775)

New data: Mileševka Canyon, 585 m, 14 June 2016 (Fig. 2).

Literature data for Serbia: Arenberger & Jakšić (1991), Gielis (2003), Guelmino (1996), Rebel (1914), Rebel & Zerny (1931), Rotschild (1912-1917), Stojanović (2012), Stojanović et al. (2014), Tot et al. (2018), Zečević (1999), Zečević (2002),

Figure 3. *Acleris forsskaleana* (Linnaeus, 1758) Mileševka Canyon, 585 m, 26 June 2016.

A moth of woodland margins and scrub, as well as on open limestone areas where the host plant grows. Larval food-plant the flower-buds and shoots of *Rosa canina*. Matović (1986) and Obratov (1992) reported presence of this species.

Fam. Tortricidae Latreille, 1802

Acleris forsskaleana (Linnaeus, 1758)

New data: Mileševka Canyon, 585 m, 26 June 2016 (Fig. 3).

Literature data for Serbia: Đurić & Hric (2015), Stojanović (2012), Stojanović et al. (2014), Tot et al. (2018), Zečević (1999), Zečević (2002).

A moth of woodland, hedgerows and scrub. Nocturnal. Larvae spin together flowers and later leaves of the food-plants, which are *Acer campestra*, *A. pseudoplatanus*, *A. platanoides* and possibly other *Acer* spp. Matović (1986) and Obratov (1992) reported presence of these species.

Figure 4. *Olethreutes arcuella* (Clerck, 1759) Šćepanica, 1139 m, 15 June 2016.

Olethreutes arcuella (Clerck, 1759)

New data: Šćepanica, 1139 m, 15 June 2016, (Fig. 4).

Literature data for Serbia: Rebel (1914), Rebel (1917), Rotschild (1912-1917), Stojanović (2012), Stojanović et al. (2014), Tot et al. (2018), Zečević (1999), Zečević & Vajgand (2001), Zečević (2002), Živojinović (1950).

Figure 5. *Amata kruegeri marjana* (Stauder, 1913) Mileševka Canyon, 585 m, 26 June 2016.

A moth of open woodland and woodland margins. Flies mostly in sunshine and also at night. Larvae feed, on the ground, on withered and decaying leaves.

Fam. Erebidae Leach, [1815]

Amata kruegeri marjana (Stauder, 1913) (Nomenclature according to De Freina (2008))

New data: Mileševka Canyon, 585 m, 26 June 2016 (Fig. 5).

Literature data for Serbia: Obraztsov (1966), Vojvodić (2011).

New species for Mt. Jadovnik. Day-flying over grassland. The larvae feed on *Plantago*, *Rumex*, *Galium* and *Taraxacum* spp. and probably other low-growing plants.

REFERENCES

Abafi-Aigner, L. 1910, Adaléka Magyar Tengermellék. Horvátország és Dalmáczia lepkefaunájához. Rovartani lapok, 17(3-4), pp. 55-57, (5-8), pp. 71-105, Budapest.

Arenberger, E. & Jakšić, P. 1991, Pterophoridae (Insecta, Lepidoptera). In: Nonveiller, G. (ed.): Fauna Durmitora 4, pp. 225-242. Titograd.

Beshkov, S. 2017, Contribution to knowledge of the Lepidoptera fauna of the Balkan Peninsula. Entomologist's Record and Journal of Variation, 129(1), pp. 9-33, 9 plates, 54 figs.

Beshkov, S., Plant, C., Nahirnić, A., King, A., & Jakšić, P. 2020, A contribution to knowledge of Balkan Lepidoptera: moths collected in May-June 2018 in Austria, Slovenia, Serbia, North Macedonia and Albania. Entomologist's Record and Journal of Variation, 132, pp. 24-45.

De Freina, J. 2008, Über die Biologie, Morphologie, Phänologie und Taxonomie von *Amata (Syntomis) kruegeri* (Ragusa, 1904) (Lepidoptera: Arctiidae, Syntominae, Syntomini). Nachr. entomol. Ver. Apollo, N.F., 28(3/4), pp. 97-107.

Gielis, C. 2003, Pterophoroidea Alucitoidea (Lepidoptera). In: World Catalogue of Insects, Apollo Books, 4, pp. 1-198.

Guelmino, J. 1996, Zenta környékének állatvilága. II. Gerinctelen állatok (Životinjski svet Sente). Zenta. Dudás Gyula Múzeumés Levéltárbarátok Köre 1-79+11 tabs.

Jakšić, P. 2020, Dnevni leptiri Jadovnika, Mileševke i susednih područja (Lepidoptera: Papilionoidea). Prirodnjački muzej u Beogradu, Posebna izdanja, 47, pp. 110.

Kereši, T. & Almaši, R. 2017, Nocturnal Lepidoptera in the vicinity of Novi Sad (Northern Serbia). Acta entomologica serbica, 14(2), pp. 147-162.

Matović, M. 1986, Vegetacija kanjona Mileševke. Monograph. Glas Polimlja, pp. 1-63.

Obratov, D. 1992, Flora i vegetacija planine Zlatar. Dissertation. Faculty of Biology. Belgrade.

Obraztsov, N. 1966, Die Palaearktische *Amata*-Arten (Lepidoptera, Ctenuchidae). Verö_entlichungen der zoologischen Staatssammlung Munchen, 10, pp. 1-383, 30 tabs, 79 figs.

Plant, C., Jakšić, P., Beshkov, S., & Nahirnić, A. 2017, A contribution to knowledge of the Balkan Lepidoptera. Some Pyraloidea (Lepidoptera: Crambidae Pyralidae) encountered recently in southern Serbia, Montenegro, the Republic of Macedonia and Albania. The University Thought - Publication in Natural Sciences, 7(2), pp. 1-27. https://doi.org/10.5937/univtho7-15336

Rebel, H. 1911, Die Lepidopterenfauna von Herkulesbad und Orsova. Eine zoogeographische Studie. Annalen des K.K. Naturhistorischen Hofmuseums, 25(3/4), pp. 253-430, figs. 1-16, tab. 1(figs. 1-17).

Rebel, H. 1914, Adatok Magyarország lepkefaunájához, (Beitrage zur Lepidopterenfauna Ungarns). Rovartani Lapok, XXI(1-3), pp. 27-53.

Rebel, H. 1917, Lepidopteren aus Neumontenegro. Sitzungsberichte der Akademie der Wissenschaften mat.-nat. Klasse, 126, pp. 765-813.

Rebel, H. & Zerny, H. 1931, Die Lepidopterenfauna Albaniens. Denkschriften der Akademie der wissenschaften inWien. Math. Nat. Klasse, 103, pp. 38-159+Taf. I., Wien.

Rotschild, C. 1912-1917, Adatok Magyarorszag lepkefaunajahoz (Beitrag zur Lepidopterenfauna Ungarns). Rovartani Lapok, XVI, pp. 130-148; XVIII, pp. 36-43; XIX, pp. 21-29, pp. 167-180; XX, pp. 66-91, pp. 170-175; XXI, pp. 27-47, pp. 72-77.

Stojanović, D. 2012, Taksonomsko-faunistička studija leptira (Insecta: Lepidoptera) Fruške gore. Disertacija. Biološki fakultet, pp. 1- 621. Beograd.

Stojanović, D., Ćurčić, S., & Tomić, M. 2014, Fauna Lepidoptera Nacionalnog Parka „Tara" Deo prvi – Microlepidoptera. Novi Sad, Bajina Bašta i Sremska Kamenica.

Szent-Ivany, J. 1945, Faunistische und ökologische Angaben über die Adelinen (Lepidopt.) des Karpatenbeckens mit Beschreibung zwei neuer Arten. Fragmenta Faunistica Hungarica, VIII(1-4), pp. 7-10.

Tot, I., Matić, B., Husarik, J., & Jovanov, A. 2018, Leptiri Spomenika priroder "Slapovi Sopotnice" i okoline zaštićenog područja (Insecta: Lepidoptera). Zbornik radova Spomenika prirode "Slapovi Sopotnice", pp. 17-33.

Vojvodić, L. 2011, Collection of Butterflies by Stanko Radovanović at the National Museum in Kikinda (Serbia). Bulletin of the Natural History Museum, 4, pp. 131-156, 6 figs.

Zečević, M. 1999, Fauna leptira (Lepidoptera, Microlepidoptera) Timočke Krajine. Razvitak, XXXIX(201-202), pp. 54-58.

Zečević, M. 2002, Fauna leptira Timočke Krajine (Istočna Srbija). Bakar Bor i Narodni muzej Zaječar, pp. 1-307.

Zečević, M. & Vajgand, D. 2001, Podaci iz kartoteke prof. dr Mihaila Gradojevića o fauni leptira (Lepidoptera) Srbije i Makedonije. Sveske Matice srpske, 37, pp. 34-78.

Zhi-Qiang Zhang, E. 2011, Animal biodiversity: An outline of higher-level classification and survey of taxonomic richness. Zootaxa, 3148, pp. 1-237.

Đurić, M. & Hric, B. 2015, Unapređeni uvid u noćne leptire Ovčarsko-Kablarske klisure. Beležnik Ovčarsko-kablarske klisure, 6(1), pp. 59-67, 2 figs.

Živojinović, S. 1950, Fauna insekata šumske domene Majdanpek. SAN, Institut za ekologiju i biogeografiju, 2, pp. 1-262.

Bulletin of Natural Sciences Research
Vol. 11, No. 1, 2021, pp. 9-16.

DOI: https://doi.org/10.5937/bnsr11-31265
Original Scientific Paper

SYNTHESIS, COMPLETE ASSIGNMENT OF ^{1}H- AND ^{13}C-NMR SPECTRA AND ANTIOXIDANT ACTIVITY OF NEW AZINE DERIVATIVE BEARING COUMARIN MOIETY

MILENKO RISTIĆ[1*], BILJANA DEKIĆ[1], NIKO RADULOVIĆ[2], MARIJA AKSIĆ[1]

[1]Faculty of Sciences and Mathematics, University of Priština in Kosovska Mitrovica, Serbia
[2]Department of Chemistry, Faculty of Sciences and Mathematics, University of Niš, Niš, Serbia

ABSTRACT

In this research, the synthesis of a new azine derivative with coumarin moiety was performed in three reaction steps, starting from 4-hydroxycoumarin. The first step in synthesis was the acetylation of 4-hydroxycoumarin to yield 3-acetyl-4-hydroxycoumarin and then the obtained 3-acetyl-4-hydroxycoumarin was reacted with hydrazine hydrate and give a corresponding hydrazone. Condensation of the hydrazone with 4-ethoxy-3-methoxybenzaldehyde afforded the target compound 1-[1-(4-hydroxy-2-oxo-2*H*-chromen-3-yl)-ethylidene]-2-(4-etoxy-3-methoxybenzylidene)-hydrazine in a good yield. The resulting azine derivative is fully spectrally characterized, including complete assignment of ^{1}H- and ^{13}C-NMR spectra, as well as 2D NMR (^{1}H-^{1}H COSY, NOESY, HSQC and HMBC) spectra. The antioxidant activity of corresponding hydrazone and target compound was evaluated by DPPH method where hydrazone derivative displayed a significant and target azine good antioxidant activity, with IC_{50} (μM) values 11.69 and 216.60, respectively.

Keywords: Synthesis, Azines, Coumarins, Spectral analysis, ^{1}H- and ^{13}C-NMR, Antioxidant activity.

INTRODUCTION

The chemistry of organic compounds undoubtedly represents an experimental field with the greatest possibilities for research that is expanding daily. Synthesis of these compounds attracts great attention to organic chemists, due to their reactivity and a wide spectrum of both biological and therapeutic activities. A similar trend is seen for azines, compounds formed by the reaction of two different or the same carbonyl compounds (mostly aldehydes or ketones) with hydrazine (Safari & Gandomi-Ravandi, 2014; Chourasiya et al., 2019). The chemical properties and biological activities of these compounds mostly are the consequence of the presence of double bonds and nitrogen atoms. It is well known that they possess antibacterial (Veena et al., 2011; Chourasiya et al., 2015), antifungal (Kurteva et al., 2011), anticonvulsant (Gul et al., 2004), anti-neuroinflammatory (Subedi et al., 2017), anticancer (Krezel et al., 1999; Qian et al., 2010; Liang et al., 2014) and antioxidant (Li et al., 2011) activities. Also, they behave as aldose reductase inhibitors (Meanwell et al., 1991) and MDR reversal agents (Paterna et al., 2018). Due to their ability to donate the lone electron pairs, azines have found great application as chemical sensors for many metal ions (Wei et al., 2017; Tiwari et al., 2018). In addition to the above, azines represent very good synthons in synthetic chemistry, especially for the preparation of heterocyclic compounds.

Coumarin and its derivatives represent a heterocyclic system that contains condensed benzene and α-pyrone ring. These condensed systems have the ability for different substitution reactions and as a result, a variety of biologically and pharmacologically active derivatives are formed. To determine these activities, an enormous number of synthesized coumarin derivatives are subjected to various assaying. They showed a remarkably wide spectrum of antimicrobial (Al-Haiza et al., 2003; Medimagh-Saidana et al., 2015; López-Rojas et al., 2018), antifungal (Guerra et al., 2015; Forezi et al, 2018), anti-HIV (Kirkiacharian et al., 2002; Su et al., 2006; Srivastav et al., 2018), anticoagulant (Manolov & Danchev, 1999), antitumor (Nofal et al., 2000; Fayed et al., 2019) and anti-inflammatory (Kontogiorgis & Hadjipavlou-Litina, 2005). Also, many coumarin derivatives are used as optical brightening agents and food supplements (Wang et al., 2013; Zhang et al., 2016). Especially, 3-substituted-4-hydroxycoumarins are the main representatives of biologically very active coumarin derivatives. A good example of this type compound is the well-known antibiotics novobiocin and clorobiocin. The mentioned 3-substituted coumarin core has a great pharmacological significance which is reflected in antibacterial (Laurin et al., 1999), anticoagulant (Manolov et al., 2006) and antioxidant (Kotali et al., 2016) properties.

Because azines showed a similar pharmacological effect, it is expected that the synthesis of azine derivatives with 3-acetyl-4-hydroxycoumarins moiety will give a promising result. This expectation confirmed a group of compounds of this type, which showed significant CDK (cyclic-dependent kinase) inhibition and a promising anticancer effect (Abdel Latif et al., 2016). However, compounds of this type are not numerous and their literature data are very scarce, primarily in the field of NMR spectral data and biological activities with an emphasis on antioxidant activity. As part of our interest in the discovery of

* Corresponding author: milenko.ristic@pr.ac.rs

novel compounds with possible pharmacological potential and following our previous work (Dekić et al., 2010, Radulović et al., 2015; Ristić et al., 2019), here we reported the synthesis, complete assignment of ^{1}H- and ^{13}C-NMR spectra, as well as 2D NMR spectra and antioxidant activity of new azine derivative obtained by condensation of hydrazone of 3-acetyl-4-hydroxycoumarin and an aromatic aldehyde, 4-ethoxy-3-methoxybenzaldehyde.

EXPERIMENTAL

General

Chemicals and materials. All solvents and chemicals were purchased from Merck (Germany), Fluka (Germany), Acros Organics (Belgium), J. T. Baker (USA), Fisher Scientific (USA) and Sigma-Aldrich (USA). Before use all solvents (acetone, methanol, absolute ethanol, ethyl acetate, hexane and chloroform) were distilled while other chemicals were used as thus obtained. The flow of the chemical reaction was monitored by thin layer chromatography (TLC) on aluminum plates with a previously applied layer of silica gel 60 F_{254}, layer thickness 0.2 mm, Merck (Germany). Visualization of spots on TLC plates was performed using a UV lamp (254 nm) or spraying (1:1, v/v) with an aqueous solution of sulfuric acid and then the TLC plates were heated until stains appeared. Column chromatography was used for purification and performed on silica gel 60 (particle size 40-63 μm), Fluka (Germany). Melting points were determined on MPM-HV2 melting point instrument (Germany).

UV-Vis measurements. UV spectra and absorbance were done on LLG UniSPEC2 spectrophotometer (Germany).

IR measurements. IR spectra were done on Thermo Nicolet 6700 FT-IR spectrophotometer (USA).

NMR measurements. One-dimensional (1D) and two-dimensional (2D) ^{1}H- and ^{13}C-NMR spectra were recorded on a Bruker Avance III 400 MHz NMR spectrometer (Switzerland). ^{1}H- spectra were recorded at 400 MHz and ^{13}C-NMR spectra at 100.6 MHz at 25 ºC. Deuterated dimethyl sulfoxide (DMSO-d_6) was used as the solvent, while tetramethylsilane (TMS) was used as the internal standard. The values of chemical shifts are given in δ (ppm) units relative to TMS (δ_H = 0.00 ppm) for ^{1}H- spectra or to the signal of residual solvent DMSO-d_6 (δ_H = 2.50 ppm and δ_C = 40.45 ppm) for ^{13}C- and heteronuclear 2D NMR spectra. For recording 2D NMR spectra (^{1}H,^{1}H-COSY, NOESY/ROESY, HSQC and HMBC) as well as for multipulse DEPT95 and DEPT135 spectra, the standard pulse sequences in the instrument software (Topspin) were used. Scalar couplings (J) are expressed in hertz (Hz).

HRMS measurements. HRMS(EI) analysis of the synthesized compounds was performed on a JOEL Mstation JMS 700 mass spectrometer (Germany). The ionization energy was 70 eV, ion trap 300 μA and the temperature of the ion source was 230 ºC.

Elemental microanalysis. Microanalysis of carbon, hydrogen, oxygen and nitrogen was performed on a Carlo Erba 1106 microanalyzer (Italy).

Synthesis

Synthesis of 3-acetyl-4-hydroxy-2H-chromen-2-one (2)

To a solution of 4-hydroxy-2*H*-chromen-2-one (1) (1.5 g, 9.3 mmol) in acetic acid (8 ml) $POCl_3$ (2.8 ml, 30 mmol) was slowly added. For the next 35 minutes, the mixture was heated at reflux in the oil bath. After completion of the reaction, the mixture was cooled in an ice bath, and the resulting precipitate was filtered. Recrystallization from ethanol gave 3-acetyl-4-hydroxy-2*H*-chromen-2-one (2) as white needle crystals (yield 90%, m.p. 135-136 °C).

Synthesis of 3-(1-hydrazonoethyl)-4-hydroxy-2H-chromen-2-one (3)

3-Acetyl-4-hydroxy-2*H*-chromen-2-one (2) (2.05 g, 10 mmol) was suspended in methanol (10 mL). After stirring for 10 minutes at room temperature, hydrazine hydrate (0.5 g, 10 mmol) was added and the obtained mixture was refluxed in a water bath for 5 hours. The reaction was monitored by TLC using ethyl acetate/hexane (2:1, v/v) as eluent. After completion of the reaction the mixture was cooled to room temperature, the resulting precipitate was filtered and washed with methanol. After air drying, the precipitate was recrystallized from ethanol to give 3-(1-hydrazonoethyl)-4-hydroxy-2H-chromen-2-one (3) as a pure light-greenish yellow powder (yield 89%, m.p. 222-224 ºC). IR (KBr, cm^{-1}): 3458, 3281, 3190, 1688, 1605, 1552, 1172, 1102. ^{1}H-NMR (400 MHz, DMSO-d_6): 15.17 (*brs*, HO–C(4)); 7.94 (*dd*, *J* = 8.0, 1.6, H–C(5)); 7.60, (*ddd*, *J* = 8.4, 8.0, 1.6, H–C(7)); 7.34 (*td*, *J* = 8.0, 0.8, H–C(6)); 7.25 (*dd*, *J* = 8.4, 0.8, H–C(8)); 6.16 (*brs*, NH_2)); 2.64 (*s*, Me). ^{13}C-NMR (100.6 MHz, DMSO-d_6): 178.3 (C(4)); 166.4 (C=N); 162.2 (C(2)); 153.4 (C(8a)); 133.8 (C(7)); 125.8 (C(5)); 123.9 (C(6)); 120.7 (C(4a)); 116.6 (C(8)); 94.1 (C(3)); 16.5 (Me). HRMS(EI): (M^+) 218.0673 ($C_{11}H_{10}N_2O_3$); requires 218.0691 (Δ = -1.8 mmu). Anal. calc. for $C_{11}H_{10}N_2O_3$: C, 60.55; H, 4.62; N, 12.83; O, 22.00; found: C, 60.76; H, 4.73; N, 12.78; O, 21.73.

Synthesis of 1-[1-(4-hydroxy-2-oxo-2H-chromen-3-yl)-ethylidene]-2-(4-ethoxy-3-methoxybenzylidene)-hydrazine (5)

3-(1-Hydrazonoethyl)-4-hydroxy-2*H*-chromen-2-one (3) (1.1 g, 5 mmol) was dissolved with stirring at room temperature in absolute ethanol (10 ml). Subsequently 4-ethoxy-3-methoxybenzaldehyde (4) (0.9 g, 5 mmol) was added and obtained mixture was refluxed in a water bath for 3 hours. The reaction was monitored by TLC using ethyl acetate/hexane (3:2, v/v). When the reaction was complete, reaction mixture was cooled to room temperature. The resulting precipitate was filtered and washed with chloroform/methanol (1:1, v/v). After purification by SiO_2 column chromatography (ethyl acetate/hexane (1:1, v/v) the target compound (5) was obtained

as brightness yellow powder (yield 83%, m.p. 186-188 °C). IR (KBr, cm^{-1}): 3389, 3092, 2975, 1697, 1601, 1555, 1176, 1111. ^{1}H-NMR (400 MHz, DMSO-d_6) 16.39 (*brs*, HO–C(4)); 8.68 (*s*, N=CH); 7.95 (*dd*, *J* = 7.2, 1.6, H–C(5)); 7.61, (*ddd*, *J* = 8.4, 7.2, 1.6, H–C(7)); 7.48 (*d*, *J* = 1.6, H–C(2')); 7.41 (*d*, *J* = 8.2, H–C(6')); 7.29 (*ddd*, *J* = 8.4, 7.2, 0.8, H–C(6)); 7.25 (*dd*, *J* = 8.4, 0.8, H–C(8)); 7.10 (*d*, *J* = 8.2, H–C(5')); 4.11 (*q*, *J* = 6.8, $CH_3\underline{CH_2}O$–C(4')); 3.85 (*s*, OMe–C(3')); 2.96 (*s*, Me); 1.37 (*t*, *J* = 6.8, $\underline{CH_3}CH_2O$–C(4')). ^{13}C-NMR (100.6 MHz, DMSO-d_6): 178.3 (C(4)); 171.8 (C=N); 161.3 (C(2)); 157.1 (N=CH); 153.4 (C(8a)); 152.1 (C(4')); 149.6 (C(3')); 133.8 (C(7)); 126.1 (C(1')); 125.8 (C(5)); 124.7 (C(6')); 123.9 (C(6)); 120.7 (C(4a)); 116.6 (C(8)); 112.8 (C(5')); 109.7 (C(2')); 94.1 (C(3)); 64.4 ($CH_3\underline{CH_2}O$–C(4')); 55.9 (OMe–C(3')); 17.9 (Me); 15.0 ($\underline{CH_3}CH_2O$–C(4')). HRMS(EI): (M^+) 380.1384 ($C_{21}H_{20}N_2O_5$); requires 380.1372 (Δ = +1.2 mmu). Anal. calc. for $C_{21}H_{20}N_2O_5$: C, 66.31; H, 5.30; N, 7.36; O, 21.03; found: C, 66.12; H, 5.48; N, 7.47; O, 20.93.

Antioxidant activity

The DPPH (2,2-diphenyl-1-picrylhydrazyl) assay was used to determine the antioxidant activity of the synthesized compounds 3 and 5, with some modification (Kadhum et al., 2011). Briefly, test samples were dissolved in methanol (12.5-400 μM) and then 2 ml of sample and 1 ml of methanolic DPPH solution (0.1 mM) were placed in a test tube. The tubes were shaken and then incubated in a dark place for 40 minutes at room temperature. For ascorbic acid, which was used as a positive control, in this case, the same procedure was repeated. The percentage inhibition of DPPH radical was determined spectrophotometrically measuring the absorbance at 517 nm against a blank (methanol) by using equation (1):

$$inhibition\ (\%) = ((A\text{-}A_1)/A) \cdot 100 \quad (1)$$

whereat *A*-absorbance of control (2 ml of methanol and 1 ml of DPPH), A_1-absorbance of the test samples (2 ml of samples and 1 ml of DPPH). Based on the relationship between the percentage inhibition of DPPH radical and the concentration of the tested samples, the results are performed in triplicate and presented in IC_{50} values (μM).

RESULTS AND DISCUSSION

Chemistry

The target azine derivative 1-[1-(4-hydroxy-2-oxo-2*H*-chromen-3-yl)-ethylidene]-2-(4-etoxy-3-methoxybenzylidene)-hydrazine (5) was prepared according to sequence of reactions presented in the Scheme 1. In the first step of reaction, the acetylation of 4-hydroxycoumarin (1) was performed with glacial acetic acid in the presence of $POCl_3$ as a catalyst to yield 3-acetyl-4-hydroxycoumarin (2). The reaction of compound (2) with hydrazine hydrate (molar ratio 1:1) in methanol, resulted the corresponding hydrazone of 3-acetyl-4-hydroxycoumarin (3). Finally, the target azine (5) was synthesized in a good yield (83%) by condensation of obtained hydrazone (3) and 4-ethoxy-3-methoxybenzaldehyde in absolute ethanol (Scheme 1).

Spectral data (HRMS(EI), IR, ^{1}H- and ^{13}C-NMR) of synthesized azine (5) were in complete agreement with the proposed structures. The IR spectra of compound (5) showed strong absorption bands at 3389 cm^{-1} which corresponding to the OH group, characteristic vibrations at 3092 cm^{-1} attributed to the Ar-H, and band at 1697 cm^{-1} concerning C=O (lactone carbonyl) of coumarin moiety. Characteristic vibrations at 1601 cm^{-1} are attributed to C=N. Intensity bands corresponding to C=C stretching vibration of the aromatic rings appeared at 1555 cm^{-1}. The IR spectra at 1176 cm^{-1} showed a characteristic C-O stretching.

High-resolution mass spectroscopy (HRMS-EI) confirmed the structure of the synthesized azine (5) with molecular formula $C_{21}H_{20}N_2O_5$ ((M^+) at *m/z* 380.1384, Δ = +1.2 mmu). In ^{1}H-NMR spectra of compound (5) exist seven signals with chemical shifts characteristic for aromatic methine protons which appeared as three doublets, two doublets of doublets, and two doublets of doublets of doublets. It is noticeable that in ^{1}H-^{1}H COSY and NOESY spectra these protons are separated into two groups of signals (Figure 1). In ^{1}H-NMR spectra (Table 1) three signals that appeared as doublets at 7.48, 7.41, and 7.10 ppm constitute the first group of protons, while the second group consisted of two sets of doublets of doublets at 7.95 ppm and 7.25 ppm and two doublets of doublets of doublets at 7.61 and 7.29 ppm.

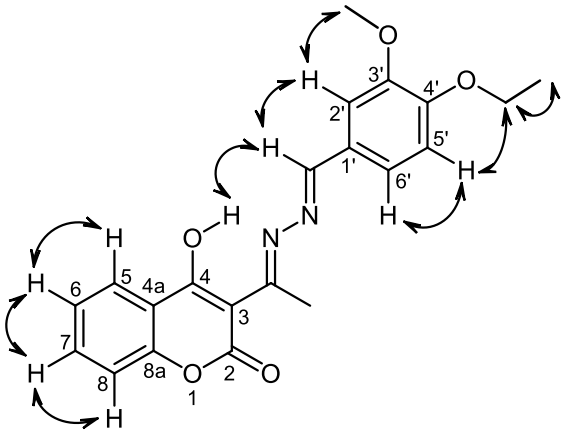

Figure 1. The NOE correlations of 1-[1-(4-hydroxy-2-oxo-2*H*-chromen-3-yl)-ethylidene]-2-(4-etoxy-3-methoxybenzylidene)-hydrazine (5) in the NOESY spectrum.

Based on the data from the HMBC and HSQC interactions it was possible to determine which aromatic protons are bonded to which ring (Figure 2). The second group which consists of four protons indicates that they belong to the coumarin ring. Chemical shifts at 7.95 and 7.25 ppm which appeared as doublets of doublets are assigned as protons on a position H-5 and H-8, whereby they coupling with one vicinal (H-6 and H-7) and one

long-range (H-7 and H-6) protons, respectively. Analyzing of given correlations, it was concluded that proton on position H-5 in HMBC spectrum, which interacts through three chemical bonds, assigns the quaternary carbons C-4 (178.3 ppm) and C-8a (153.4 ppm). This spectrum also showed that the carbon at 133.8 ppm is C-7 by the presence of a cross peak with H-5, which then allowed the assignment of H-7 as a peak at 7.61 ppm in HSQC. Analogously, the proton at position H-8 showed interactions with C-4a (120.7 ppm) and C-6 (123.9 ppm) and thus the shift of the proton H-6 was deduced to be 7.29 ppm from HSQC. Also, a characteristic interaction was observed through two chemical bonds between the proton H-8 and the quaternary carbon C-8a, which is assigned at 153.4 ppm (Figure 2). In the HMBC spectrum, the assignment of carbons C-4a and C-8a were also confirmed by protons interactions at position H-6 and H-7, respectively. The signal at 2.96 ppm in ^{1}H-NMR spectrum assigned as a singlet of methyl protons attached at the 3-C=N, in HMBC spectrum showed interactions with carbon C-3 (94.1 ppm), through three bonds, and with the signal at 171.8 ppm, through two bonds, which corresponded to the carbon of imine group (MeC=N). The largest chemical shift at 16.39 ppm in the ^{1}H-NMR spectrum which appeared as a broad singlet, was assigned to the proton of the OH group at position C-4 on coumarin moiety. The only remaining signal in ^{13}C-NMR spectra at 161.3 ppm was assigned to lactone carbonyl carbon (C-2), since no interaction was observed in HSQC and HMBC spectra.

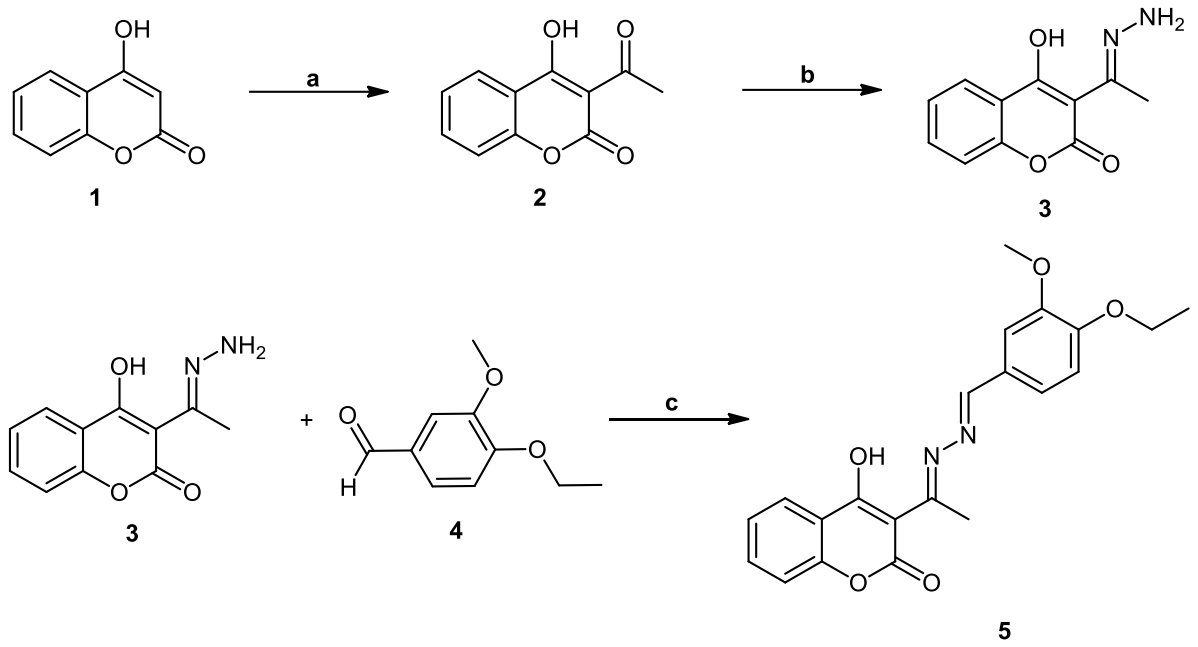

Scheme 1. Synthesis of target azine derivative 1-[1-(4-hydroxy-2-oxo-2*H*-chromen-3-yl)-ethylidene]-2-(4-etoxy-3-methoxybenzylidene)-hydrazine (5).
Reagents and condition: (a) CH_3COOH, $POCl_3$, reflux (35 min.), (b) $NH_2NH_2 \cdot H_2O$, MeOH, reflux (5 h), (c) abs. EtOH, reflux (3 h)

Aromatic protons on the substituent side which appeared at 7.48, 7.41 and 7.10 ppm in the ^{1}H-NMR spectrum as a doublet, were attributed to H-2', H-6' and H-5', respectively. The signals of carbons C-2', C-6', and C-5' (Table 1) of the substituent ring, were readily connected to the aforementioned ^{1}H-NMR signals according to correlations in the HSQC spectrum, and further corroborated by HMBC data. The proton of OH group on coumarin moiety in NOESY spectrum showed interaction with the signal at 8.68 ppm which appeared as singlet and corresponded to the proton of azomethine group (N=CH) on the substituent side. The mentioned proton in the HMBC spectrum has two more interactions which are accomplished through three chemical bonds, whereby assigned a carbons C-2' (109.7 ppm) and C-6' (124.7 ppm), (Figure 2). Also, the position of the carbon C-1' (126.1 ppm) is confirmed by the interactions of the proton H-5' in the HMBC spectrum. In NOESY spectrum proton H-5'

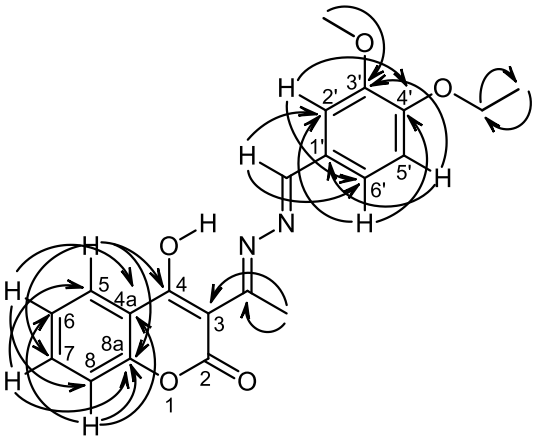

Figure 2. The HMBC correlations of 1-[1-(4-hydroxy-2-oxo-2*H*-chromen-3-yl)-ethylidene]-2-(4-etoxy-3-methoxybenzylidene)-hydrazine (5).

showed interaction with a peak that appeared as a quartet at 4.11 ppm in the ^{1}H-NMR spectrum and corresponded to the methylene protons of the ethoxy group. Also, methylene protons from the ethoxy group in the NOESY spectrum are in correlations with methyl protons (Figure 1) of the mentioned group which appeared as a triplet at the smallest chemical shifts of 1.37 ppm. Further, the aforementioned correlation between the methyl and methylene protons is confirmed by their interaction through two chemical bonds with the carbon atoms to which they are attached, in the HMBC spectrum. The last remaining signal (appeared as singlet) in the ^{1}H-NMR spectrum at 3.85 ppm belong to the protons of a methoxy group at position 3', which is confirmed by their interaction in the NOESY spectrum with a proton at position H-2'. The chemical shift of the remaining quaternary carbon C-4' (152.1 ppm) on the substituent side was determined from HMBC interactions, through three chemical bonds (H-2' and H-6').

The data provided by the NOESY spectrum were used for the determination of the spatial relationship between the coumarin core and the aryl substituent. The proton of the OH group on coumarin moiety showed a cross peak with the hydrogen of the azomethine group (N=CH, Figure 1), which makes it possible to determine the orientation of the aryl substituent (Figure 3).

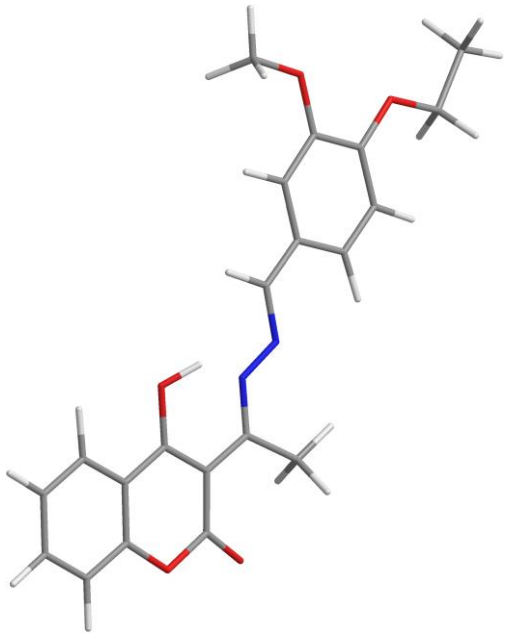

Figure 3. Spatial orientation of coumarin moiety and aryl-substituent in the molecule of 1-[1-(4-hydroxy-2-oxo-2*H*-chromen-3-yl)-ethylidene]-2-(4-etoxy-3-methoxybenzylidene)-hydrazine (5), obtained by energy minimization using the MM2 force field in the *ChemBio3D Ultra 12.0* software package.

Table 1. ^{1}H- and ^{13}C-NMR chemical shifts (δ, ppm), integrals, multiplets, coupling constants (J, Hz), crucial NOESY and HMBC correlations of 1-[1-(4-hydroxy-2-oxo-2*H*-chromen-3-yl)-ethylidene]-2-(4-etoxy-3-methoxybenzylidene)-hydrazine (5).

Position	δ ^{1}H (ppm)	Integral	Multiplet	J (Hz)	δ ^{13}C (ppm)	NOESY (^{1}H↔^{1}H)	HMBC (^{1}H→^{13}C)
2	–	–	–	–	161.3	–	–
3	–	–	–	–	94.1	–	–
4	–	–	–	–	178.3	–	–
4a	–	–	–	–	120.7	–	–
5	7.95	1H	*dd*	1.6, 7.2	125.8	H-6	C-7, C-4, C-8a
6	7.29	1H	*ddd*	0.8, 7.2, 8.4	123.9	H-5, H-7	C-4a, C-8
7	7.61	1H	*ddd*	1.6, 7.2, 8.4	133.8	H-6, H-8	C-5, C-8a
8	7.25	1H	*dd*	0.8, 8.4	116.6	H-7	C-4a, C-6, C-8a
8a	–	–	–	–	153.4	–	–
OH	16.39	1H	*brs*	–	–	N=C<u>H</u>	–
C=N	–	–	–	–	171.8	–	–
CH_3	2.96	3H	*s*	–	17.9	–	C-3, N=C
N=CH	8.68	1H	*s*	–	157.1	H-2', OH	C-2', C-6'
1'	–	–	–	–	126.1	–	–
2'	7.48	1H	*d*	1.6	109.7	N=C<u>H</u>, 3'-OC<u>H</u>$_3$	C-4', C-6'
3'	–	–	–	–	149.6	–	–
3'-OCH_3	3.85	3H	*s*	–	55.9	H-2'	C-3'
4'	–	–	–	–	152.1	–	–
4'-O<u>CH$_2$</u>CH_3	4.11	2H	*q*	6.8	64.4	H-5', 4'-OCH$_2$C<u>H$_3$</u>	4'-OCH$_2$<u>C</u>H$_3$
4'-OCH$_2$<u>CH$_3$</u>	1.37	3H	*t*	6.8	15.0	4'-O<u>CH$_2$</u>CH$_3$	4'-O<u>C</u>H$_2$CH$_3$
5'	7.10	1H	*d*	8.2	112.8	H-6', 4'-O<u>CH$_2$</u>CH$_3$	C-1', C-3'
6'	7.41	1H	*d*	8.2	124.7	H-5'	C-2', C-4'

On the other hand, the proton of the azomethine group also showed simultaneous interactions with proton H-2'. All mentioned interactions indicated that the diimine bridge was created, whereby coumarin moiety and ring of the substituent, toward each other at a specific angle (Figure 3).

Antioxidant activity

Antioxidants are compounds that slow down the oxidation processes in the human body. They act as "scavengers" of free radicals, or electron donors, and thus prevent chain reactions in which other molecules in cells are damaged. In addition to natural antioxidants, synthetic antioxidants have been developed and used in practice as additives, supplements, and drugs. Due to a lack of antioxidants, many health diseases occur in humans, such as cardiovascular, carcinogenic, and inflammatory (Nojiri et al., 2004). The DPPH assay is based on monitoring the color change of a purple-colored solution of a stable DPPH radical, into a reduced yellow-colored form (DPPH-H). DPPH is a stable free radical with a delocalized free electron on nitrogen so that the molecule does not form dimers, which is often the case with most other free radicals. Delocalization allows the appearance of a purple color, with maximum absorption at 517 nm. Receiving a proton from a potential antioxidant he is reduced to hydrazine, whereby the intensity of absorption is decreased since hydrazine is not absorbed in that wavelength. A higher degree of discoloration means a higher reduction ability.

Substitution, the position of substitution, and the nature of the substituent significantly affect antioxidant activity. Thus, for example, compounds that have electron-donating groups on the phenolic ring contribute to increases in antioxidant activity, while electron-withdrawing groups usually decrease antioxidant activity (Lee et al., 2015).

As can be seen (Table 2), compound (3) showed significant antioxidant activity with IC_{50} value of 11.69 μM, while compound (5) showed slightly more moderate antioxidant activity (216.60 μM). In our case, ascorbic acid was used as a criterion to compare the ability to neutralize DPPH radicals with the tested compounds, i.e. as a positive control, since it is known that represented an exceptional antioxidant.

Table 2. DPPH free radical scavenging activity (IC_{50}, μM) of compound (3), (5), and ascorbic acid

Compound	IC_{50} (μM)
3	11.69
5	216.60
Ascorbic acid	7.82

As both tested compounds on the coumarin part of the molecule have an OH group that participates in the formation of a strong hydrogen bond with the nitrogen atom, indicates that the OH group probably does not have any effect on the antioxidant action. The significant antioxidant activity of hydrazone of 3-acetyl-4-hydroxycoumarin (3) is a probable consequence of the electron-donating ability of the amino group and the high resonance stabilization of the formed radical. Similar to previous, although the tested compound (5) does not have an OH group on the aryl core that would certainly affect the increases in antioxidant activity, there are two electron-donating groups, methoxy and ethoxy group, which probably have influenced on the mentioned compound to exhibit a good antioxidant activity.

CONCLUSION

A new mixed azine derivative bearing coumarin moiety was synthesized and fully spectrally assigned using 1D- and 2D-NMR spectral data. The resulting azine was obtained in a good yield by condensation of hydrazone of 3-acetyl-4-hydroxycoumarin and 4-ethoxy-3-methoxybenzaldehyde in a simple, rapid, and very effective way. Synthesized compounds (3) and (5) were monitored for their antioxidant activity. The antioxidant activity of the compound (3) against the stable free radical DPPH showed that this compound possessed a significant antioxidant power, while compound (5) demonstrated somewhat smaller, but still good antioxidant potential. The results obtained in this study will primarily contribute to organic synthesis and better knowledge of the structure of this group of compounds, formed by the reaction of hydrazone of coumarin and aldehydes. The obtained target azine represents a very interesting starting material for further biological and pharmacological research.

ACKNOWLEDGMENTS

This work was financially supported by the Ministry of Education, Science and Technological Development of Serbia [Project No. 172061 and 45022] and Faculty of Sciences and Mathematics, University of Priština in Kosovska Mitrovica [Project IJ-0205].

REFERENCES

Abdel Latif, N. A., Batran, R. Z., Khedr, M. A. & Abdalla, M. M. 2016. 3-Substituted-4-hydroxycoumarin as a new scaffold with potent CDK inhibition and promising anticancer effect: Synthesis, molecular modeling and QSAR studies. Bioorganic Chemistry, 67, pp. 116-129. doi: 10.1016/j.bioorg.2016.06.005

Al-Haiza, M. A., Mostafa, M. S. & El-Kady, M. Y. 2003. Synthesis and biological evaluation of some new coumarin derivatives. Molecules, 8(2), pp. 275-286. doi: 10.3390/80200275

Chourasiya, S. S., Kathuria, D., Singh, S., Sonawane, V. C., Chakraborti, A. K. & Bharatam P. V. 2015. Design, synthesis and biological evaluation of novel unsymmetrical azines as quorum sensing inhibitors. RSC Advances, 5(97), pp. 80027-80038. doi: 10.1039/C5RA12925G

Chourasiya, S. S., Kathuria, D., Wani, A. A. & Bharatam, P. V. 2019. Azines: synthesis, structure, electronic structure and their applications. Organic & Biomolecular Chemistry, 17(37), pp. 8486-8521. doi: 10.1039/C9OB01272A

Dekić, V., Radulović, N., Vukićević, R., Dekić, B., Skropeta, D. & Palić, R. 2010. Complete assignment of the ^{1}H and ^{13}C NMR spectra of antimicrobial 4-arylamino-3-nitrocoumarin derivatives. Magnetic Resonance in Chemistry, 48(11), pp. 896-902. doi: 10.1002/mrc.2681

Fayed, E. A., Sabour, R., Harras, M. F. & Mehany, A. B. 2019. Design, synthesis, biological evaluation and molecular modeling of new coumarin derivatives as potent anticancer agents. Medicinal Chemistry Research, 28, pp. 1284-1297. doi: 10.1007/s00044-019-02373-x

Forezi, L. da S. M., Borba-Santos, L. P., Cardoso, M., Ferreira, V. F., Rozental, S. & Silva, de C da, F. 2018. Synthesis and Antifungal Activity of Coumarins Derivatives Against *Sporothrix* spp. Current Topics in Medicinal Chemistry, 18(2), pp. 164–171. doi: 10.2174/1568026618666180221115500

Guerra, F. S., Araújo, R. S., Sousa, J. P., Pereira, F. D., Mendonça-Junior, F. J., Barbosa-Filho, J. & Lima, E. D. 2015. Evaluation of Antifungal Activity and Mode of Action of New Coumarin Derivative, 7-Hydroxy-6-nitro-2H-1-benzopyran-2-one, against *Aspergillus* spp. Evidence-based Complementary and Alternative Medicine, 2015, ID 925096. doi: 10.1155/2015/925096

Gul, H. I., Calis, U. & Vepsalainen J. 2004. Synthesis of some mono-Mannich bases and corresponding azine derivatives and evaluation of their anticonvulsant activity. Arzneimittelforschung, 54(7), pp. 359-364. doi: 10.1055/s-0031-1296984

Kadhum, A. A., Al-Amiery, A. A., Musa, A. Y. & Mohamad, A. B. 2011. The antioxidant activity of new coumarin derivatives. International Journal of Molecular Sciences, 12(9), pp. 5747-5761. doi: 10.3390/ijms12095747

Kirkiacharian, S., Thuy, D. T., Sicsic, S., Bakhchinian, R., Kurkjian, R. & Tonnaire, T. 2002. Structure-activity relationships of some 3-substituted-4-hydroxycoumarins as HIV-1 protease inhibitors. Il Farmaco, 57(9), pp. 703-708. doi: 10.1016/s0014-827x(02)01264-8

Kontogiorgis, C. A. & Hadjipavlou-Litina, D. J. 2005. Synthesis and antiinflammatory activity of coumarin derivatives. Journal of Medicinal Chemistry, 48(20), pp. 6400-6408. doi: 10.1021/jm0580149

Kotali, A., Nasiopoulou, D. A., Tsoleridis, C. A., Harris, P. A., Kontogiorgis, C. A. & Hadjipavlou-Litina, D. J. 2016. Antioxidant Activity of 3-[N-(Acylhydrazono)ethyl]-4-hydroxy-coumarins. Molecules, 21(2), pp. 138. doi: 10.3390/molecules21020138

Krezel, I., Mikiciuk-olasik, E., Zurek, E. & Glowka, M. L. 1999. New Mitoguazone Analogues with Anticancer Activity. Pharmacy and Pharmacology Communications, 5(8), pp. 485-49 0. doi: 10.1211/146080899128735216

Kurteva, V. B., Simeonov, S. P. & Stoilova-Disheva, M. 2011. Symmetrical Acyclic Aryl Aldazines with Antibacterial and Antifungal Activity. Pharmacology & Pharmacy, 2(1), pp. 1-9. doi: 10.4236/pp.2011.21001

Laurin, P., Ferroud, D., Klich, M., Dupuis-Hamelin, C., Mauvais, P., Lassaigne, P., Bonnefoy, A. & Musicki, B. 1999. Synthesis and in vitro evaluation of novel highly potent coumarin inhibitors of gyrase B. Bioorganic & Medicinal Chemistry Letters, 9(14), pp. 2079-2084. doi: 10.1016/s0960-894x(99)00329-7

Lee, C. Y., Nanah, C. N., Held, R. A., Clark, A. R., Huynh, U. G., Maraskine, M. C., Uzarski, R. L., McCracken, J. & Sharma, A. 2015. Effect of electron donating groups on polyphenol-based antioxidant dendrimers. Biochimie, 111, pp. 125-134. doi: 10.1016/j.biochi.2015.02.001

Liang, C., Xia, J., Lei, D., Li, X., Yao, Q., & Gao, J. 2014. Synthesis, in vitro and in vivo antitumor activity of symmetrical bis-Schiff base derivatives of isatin. European Journal of Medicinal Chemistry, 74, pp. 742-750. doi: 10.1016/j.ejmech.2013.04.040

Li, D. Q., Tan, M. X., & Jie, L. 2011. Synthesis, Antioxidant and Antibacterial Activities of Salicylaldehyde Azine. Advanced Materials Research, 396-398, pp. 2366-2369. doi: 10.4028/www.scientific.net/AMR.396-398.2366

López-Rojas, P., Janeczko, M., Kubiński, K., Amesty, Á., Masłyk, M. & Estévez-Braun, A. 2018. Synthesis and Antimicrobial Activity of 4-Substituted 1,2,3-Triazole-Coumarin Derivatives. Molecules, 23(1), pp. 199. doi: 10.3390/molecules23010199

Manolov, I. & Danchev, N. D. 1999. Synthesis, toxicological, and pharmacological assessment of some oximes and aldehyde condensation products of 4-hydroxycoumarin. Archiv der Pharmazie, 332(7), pp. 243-248. doi: 10.1002/(sici)1521-4184(19997)332:7<243::aid-ardp243>3.0.co;2-2

Manolov, I., Maichle-Moessmer, C. & Danchev, N. 2006. Synthesis, structure, toxicological and pharmacological investigations of 4-hydroxycoumarin derivatives. European Journal of Medicinal Chemistry, 41, pp. 882-890. doi: 10.1016/j.ejmech.2006.03.007.

Meanwell, N. A., Roth, H. R., Smith, E. C. R., Wedding, D. L. & Wright, J. J. K. 1991. Diethyl 2,4-dioxoimidazolidine-5-phosphonates: Horner-Wadsworth-Emmons reagents for the mild and efficient preparation of C-5 unsaturated hydantoin derivatives. The Journal of Organic Chemistry, 56(24), pp. 6897-6904. doi: 10.1021/jo00024a036

Medimagh-Saidana, S., Romdhane, A., Daami-Remadi, M., Jabnoun-Khiareddine, H., Touboul, D., Jannet, H. B. & Hamza, M. A. 2015. Synthesis and antimicrobial activity of novel coumarin derivatives from 4-methylumbelliferone. Medicinal Chemistry Research, 24, pp. 3247-3257. doi: 10.1007/s00044-015-1368-y

Nofal, Z. M., El-Zahar, M. I. & Abd El-Karim, S. S. 2000. Novel Coumarin Derivatives with Expected Biological Activity. Molecules, 5(2), pp. 99-113. doi: 10.3390/50200099

Nojiri, S., Daida, H. & Inaba, Y. 2004. Antioxidants and cardiovascular disease: Still a topic of interest. Environmental Health and Preventive Medicine, 9(5), pp. 200-213. doi: 10.1007/BF02898101

Paterna, A., Khonkarn, R., Mulhovo, S., Moreno, A., Girio, P. M., Baubichon-Cortay, H., Falson, P. & Ferreira, M. J. U. 2018. Monoterpene indole alkaloid azine derivatives as MDR reversal agents. Bioorganic & Medicinal Chemistry, 26(2), pp. 421-434. doi: 10.1016/j.bmc.2017.11.052

Qian, Y., Zhang, H-Jia., Lv, P-C. & Zhu, H-L. 2010. Synthesis, molecular modeling and biological evaluation of guanidine derivatives as novel antitubulin agents. Bioorganic & Medicinal Chemistry, 18(23), pp. 8218-8225. doi: 10.1016/j.bmc.2010.10.008

Radulović, N., Stojanović-Radić, Z., Stojanović, N., Stojanović, P., Dekić, V. & Dekić, B. 2015. A small library of 4-(alkylamino)-3-nitrocoumarin derivatives with potent antimicrobial activity against gastrointestinal pathogens, Journal of the Serbian Chemical Society, 15(3), pp. 315-327. doi: 10.2298/JSC140619085R

Ristić, M., Radulović, N., Dekić, B., Dekić, V., Ristić, N. & Stojanović-Radić, Z. 2019. Synthesis and Spectral Characterization of Asymmetric Azines Containing a Coumarin Moiety: The Discovery of New Antimicrobial and Antioxidant Agents. Chemistry & Biodiversity, 16(1), e1800486. doi: 10.1002/cbdv.201800486

Safari. J. & Gandomi-Ravandi, S. 2014. Structure, synthesis and application of azines: a historical perspective. RSC Advances, 4(86), pp. 46224-46249. doi: 10.1039/C4RA04870A

Srivastav, V. K., Tiwari, M. K., Zhang, X. & Yao, X. J. 2018. Synthesis and Antiretroviral Activity of 6-Acetyl-coumarin Derivatives against HIV-1 Infection. Indian Journal of Pharmaceutical Sciences, 80, pp. 108-117. doi: 10.4172/pharmaceutical-sciences.1000335

Subedi, L., Kwon, O. W., Pak, C., Lee, G., Lee, K., Kim, H. & Kim. S. Y. 2017. N,N-disubstituted azines attenuate LPS-mediated neuroinflammation in microglia and neuronal apoptosis via inhibiting MAPK signaling pathways. BMC Neuroscience, 18:82. doi: 10.1186/s12868-017-0399-3

Su, C. X., Mouscadet, J. F., Chiang, C. C., Tsai, H. J. & Hsu, L. Y. 2006. HIV-1 integrase inhibition of biscoumarin analogues. Chemical & Pharmaceutical Bulletin, 54(5), pp. 682-686. doi: 10.1248/cpb.54.682

Tiwari, K., Kumar, S., Kumar, V., Kaur, J., Arora, S. & Mahajan, R. K. 2018. An azine based sensor for selective detection of Cu^{2+} ions and its copper complex for sensing of phosphate ions in physiological conditions and in living cells. Spectrochimica acta. Part A, Molecular and Biomolecular Spectroscopy, 191, pp. 16-26. doi: 10.1016/j.saa.2017.09.072

Veena, K., Ramaiah, M., Shashikaladevi, K., Avinash, T. S. & Vaidya V. P. 2011. Synthesis and antimicrobial activity of asymmetrical azines derived from naphtho[2,1-b]furan. Journal of Chemical and Pharmaceutical Research, 3(5), pp. 130-135.

Wang, Y. H., Avula, B., Nanayakkara, N. P., Zhao, J. & Khan, I. A. 2013. Cassia cinnamon as a source of coumarin in cinnamon-flavored food and food supplements in the United States. Journal of Agricultural and Food Chemistry, 61(18), pp. 4470-4476. doi: 10.1021/jf4005862

Wei, T., Liang, G., Chen, X., Qi, J., Lin, Q., Zhang, Y. & Yao, H. 2017. A functional applied material on recognition of metal ion zinc based on the double azine compound. Tetrahedron, 73(20), pp. 2938-2942. doi: 10.1016/j.tet.2017.04.001

Zhang, G., Zheng, H., Liu, G., Wang, P., & Xiang, R. 2016. Synthesis and application of a multifunctional fluorescent polymer based on coumarin. BioResources, 11(1), pp. 373-384. doi: 10.15376/biores.11.1.373-384

Bulletin of Natural Sciences Research
Vol. 11, No. 1, 2021, pp. 17-23.
DOI: https://doi.org/10.5937/bnsr11-26981
Original Scientific Paper

THE PREPARATION AND CHARACTERIZATION OF SOME NOVEL FEROCENIL DERIVATIVES

DANIJELA ILIĆ KOMATINA[1], ALEKSANDRA MINIĆ JANČIĆ[1], JOVANA BUGARINOVIĆ[2], DRAGANA STEVANOVIĆ[2]

[1]Faculty of Technical Sciences, University of Priština in Kosovska Mitrovica, Serbia
[2]Faculty of Science, University of Kragujevac, Kragujevac, Serbia

ABSTRACT

This paper provides a report on an easily performable synthesis *via* one-pot reaction, between the newly synthesized 3-arylamino-1-ferrocenylpropan-1-ols and PhNCO. We have used the acetic acid as the catalyst and ultrasound irradiation as the reaction promoter. We have evaluated the reaction score on three examples. In order to gain a more comprehensive insight into the role of α-ferrocenyl carbocation, we have described a plausible mechanism of the transformations in question. Moreover, we have purified the prepared by using column chromatography. Besides, we provide a detailed characterization of the new compounds (products and starting material), which was performed by IR, NMR and elemental analyses.

Keywords: Tetrahydropirimidine ring, Ferrocene, Intramolecular cyclization, α-Ferrocenyl carbocation, Spectral characterization.

INTRODUCTION

Over the past few years, we have witnessed a radical change for modern organic chemistry, namely, raising awareness of the issues of environmental sustainability and efficiency. Consequently, one-pot reactions which involve various types of cascade and tandem reactions are being increasingly seen as a favourable approach due to their higher efficiency, operational simplicity, increased cost effectiveness and reduced generation of chemical waste. This is particularly striking in comparison with other synthetic methodologies (Hayashi 2016; Nicolaou et al., 2006; Motokura et al., 2005; Yang et al., 2016; Domling et al., 2012). In a similar vein, a new mainstream method has emerged, especially in the development of sustainable, frequently catalyst- or/and solvent-free versions of challenging reactions (Sarma et al., 2012a). Moreover, from the perspective of industrial manufacturing and "green" chemistry, such strategies would result in high yields of relatively pure products in shorter reaction times. Therefore, these strategies can be seen as not only eco-friendly, but also as financially viable options (Sharma et al., 2012b).

In contrast, heterocycles constitute one of the largest classes of organic compounds (Eicher et al., 2013). Heterocycles represent important structural motifs which are to be found extensively across a range of biologically active natural products, drug intermediates, pharmaceuticals and dye chemistry, as well as common versatile building blocks used for the synthesis of a variety of compounds (Taylor et al., 2016). For instance, at present, the most dominant among prescription medicaments constitute small heterocyclic molecules (containing diverse functional groups), or more complex structures containing a heterocyclic core fragment (Taylor et al., 2016). Within the class of heterocycles, in recent years we have seen an increased interest of both chemists and biologists for urea derivatives, which have since been synthesized extensively. This specific class of compounds is characterized by a wide range of biological activities (Kashawa et al., 2009; Khan et al., 2008; Kaneko et al., 2007; Li et al., 2009; Tale et al., 2011; Fernandez & Caballero, 2006), which consequently resulted in a heightened interest for their synthesis. For this reason, the synthesis and characterization of novel cyclic ureas bearing ferrocenyl group obtained in this manner could be increasingly significant in the future.

Our team have recently reported synthesis of bioactive 2-ferrocenoyl ethyl aryl amines (Damljanović et al., 2011; Pejović et al., 2012a). These results are a proof of our sustained interest in the synthesis of novel Fc-containing (Fc = ferrocene) heterocyclic compounds, which are of potential biological significance (Pejović et al., 2012b; Pejović et al., 2017; Pejović et al., 2018a; Pejović et al., 2018b), and in the design and optimizations of reactions conditions. 2-Ferrocenoyl ethyl aryl amines - Mannich bases have demonstrated great initial results in the synthesis of Fc derivatives (Minić et al., 2017; Minić et al., 2018; Minić et al., 2019), notably in the synthesis of six-membered ureas (Minić et al., 2015; Minić et al., 2020a).

In view of this, we report the synthesis completed *via* one-pot reaction, between novel 3-arylamino-1-ferrocenylpropan-1-ols (which was obtained from corresponding Mannich bases), phenyl isocyanate, and acetic acid. All the above mentioned compounds used in this synthesis, including the products and the starting material, have been subjected to purification by column chromatography and their structure has been confirmed with the use of spectroscopic data (^{1}H-NMR, ^{13}C-NMR, 2D-NMR and IR). Moreover, elemental analyses have been used in this

*Coresponding author: danijela.ilic@pr.ac.rs

process. Furthermore, this synthetic approach generates novel Fc-containing heterocyclic systems which may prove to be biologically relevant.

EXPERIMENTAL

Materials and measurements

All chemicals were commercially available and used as received, except that the solvents were purified by distillation. Chromatographic separations were carried out using Silica Gel 60 (Merck, 230–400 mesh ASTM), whereas Silica Gel 60 on Al plates, layer thickness 0.2 mm (Merck) was used for TLC. Melting points were determined on a Mel-Temp capillary melting points apparatus, model 1001 and are uncorrected. Microanalysis of carbon and hydrogen were carried out with a Carlo Erba 1106 microanalyser; their results agreed favorably with the calculated values. IR measurements were carried out with a Perkin–Elmer FTIR 31725-X spectrophotometer. NMR spectra were recorded on a Bruker Avance III 400 MHz (^{1}H at 400 MHz, ^{13}C at 101 MHz) and Varian Gemini (^{1}H at 200 MHz, ^{13}C at 50 MHz) NMR spectrometers. Chemical shifts are reported in ppm (δ) values relative to TMS (δ_H 0 ppm) in ^{1}H, ^{13}C and heteronuclear 2D NMR spectra.

Synthesis and spectral characterization

*General procedure for the synthesis of 3-(arylamino)-1-ferrocenylproran-1-ones (**3a-c**)*

Ketones **3a-c** were synthesized by the known procedure (Pejović et al., 2012a; Minić et al., 2015; Minić et al., 2017; Minić et al., 2018; Minić et al., 2019). Spectral data of compounds **3a-c** follow.

1-Ferrocenyl-3-((2-iodophenyl)amino)propan-1-one (***3a***). Dark red solid; mp 162 °C. Yield 62%. ^{1}H NMR (400 MHz, $CDCl_3$) δ = 7.71 – 7.67 (m, 1H, CH_{Ar}), 7.30 – 7.25 (m, 2H, 2 × CH_{Ar}), 6.69 (d, *J* = 7.9 Hz, 1H, CH_{Ar}), 4.80 (pseudo t, *J* = 1.9 Hz, 2H, 2 × CH_{Cp}), 4.68 (t, *J* = 5.8 Hz, 1H, $CH_2CH_2N\underline{H}$), 4.54 (pseudo t, *J* = 1.9 Hz, 2H, 2 × CH_{Cp}), 4.17 (s, 5H, 5 × CH_{Cp}), 3.65 (q, *J* = 6.2 Hz, 2H, $CH_2C\underline{H_2}NH$), 3.11 – 3.05 (m, 2H, $C\underline{H_2}CH_2NH$). ^{13}C NMR (101 MHz, $CDCl_3$) δ = 202.7 (C=O), 146.9 (C_{Ar}), 139.3 (C_{Ar}), 129.4 (C_{Ar}), 118.8 (C_{Ar}), 110.5 (C_{Ar}), 85.8 (C_{Ar}), 78.8 (C_{Cp}), 72.5 (2 × C_{Cp}), 69.9 (5 × C_{Cp}), 69.3 (2 × C_{Cp}), 38.8 ($CH_2\underline{C}H_2NH$), 38.2 ($\underline{C}H_2CH_2NH$). IR (ATR, cm^{-1}): ν = 3210 (N-H) cm^{-1}; ν = 1651 (C=O) cm^{-1}. Anal. Calc. for $C_{19}H_{18}FeINO$: C, 49.71; H, 3.95; Fe, 12.16; I, 27.64; N, 3.05; O, 3.48. Found: C, 49.76, H, 3.91, N, 3.12%.

1-Ferrocenyl-3-((3-iodophenyl)amino)propan-1-one (***3b***). Dark red solid; mp 156 °C. Yield 74%. ^{1}H NMR (400 MHz, $CDCl_3$) δ = 7.06 – 7.00 (m, 2H, 2 × CH_{Ar}), 6.94 – 6.85 (m, 1H, CH_{Ar}), 6.65 – 6.60 (m, 1H, CH_{Ar}), 4.81 (pseudo t, *J* = 1.9 Hz, 2H, 2 × CH_{Cp}), 4.54 (pseudo t, *J* = 1.9 Hz, 2H, 2 × CH_{Cp}), 4.30 (s, 1H, $CH_2CH_2N\underline{H}$), 4.15 (s, 5H, 5 × CH_{Cp}), 3.55 (s, 2H, $CH_2C\underline{H_2}NH$), 3.03 (t, *J* = 6.0 Hz, 2H, $C\underline{H_2}CH_2NH$). ^{13}C NMR (101 MHz, $CDCl_3$) δ = 203.3 (C=O), 149.0 (C_{Ar}), 130.8 (C_{Ar}), 126.4 (C_{Ar}), 121.3 (C_{Ar}), 112.6 (C_{Ar}), 95.4 (C_{Ar}), 78.7 (C_{Cp}), 72.5 (2 × C_{Cp}), 69.9 (5 × C_{Cp}), 69.3 (2 × C_{Cp}), 38.5 ($CH_2\underline{C}H_2NH$), 37.9 ($\underline{C}H_2CH_2NH$). IR (ATR, cm^{-1}): ν = 3230 (N-H) cm^{-1}; ν = 1663 (C=O) cm^{-1}. Anal. Calc. for $C_{19}H_{18}FeINO$: C, 49.71; H, 3.95; Fe, 12.16; I, 27.64; N, 3.05; O, 3.48. Found: C, 49.76, H, 3.99, N, 3.10%.

1-Ferrocenyl-3-((4-iodophenyl)amino)propan-1-one (***3c***). Dark red solid; mp 160 °C. Yield 56%. ^{1}H NMR (400 MHz, $CDCl_3$) δ = 7.54 – 7.37 (m, 2H, 2 × CH_{Ar}), 6.58 – 6.36 (m, 2H, 2 × CH_{Ar}), 4.77 (pseudo t, *J* = 2.0 Hz, 2H, 2 × CH_{Cp}), 4.54 (pseudo t, *J* = 2.0 Hz, 2H, 2 × CH_{Cp}), 4.29 (s, 1H, $CH_2CH_2N\underline{H}$), 4.16 (s, 5H, 5 × CH_{Cp}), 3.56 (s, 2H, $CH_2C\underline{H_2}NH$), 3.01 (t, *J* = 5.9 Hz, 2H, $C\underline{H_2}CH_2NH$). ^{13}C NMR (101 MHz, $CDCl_3$) δ = 203.3 (C=O), 147.3 (C_{Ar}), 137.9 (C_{Ar}), 115.2 (C_{Ar}), 78.7 (C_{Ar}), 78.0 (C_{Cp}), 72.6 (2 × C_{Cp}), 69.9 (5 × C_{Cp}), 69.3 (2 × C_{Cp}), 38.6 ($CH_2\underline{C}H_2NH$), 38.0 ($\underline{C}H_2CH_2NH$). IR (ATR, cm^{-1}): ν = 3190 (N-H) cm^{-1}; ν = 1657 (C=O) cm^{-1}. Anal. Calc. for $C_{19}H_{18}FeINO$: C, 49.71; H, 3.95; Fe, 12.16; I, 27.64; N, 3.05; O, 3.48. Found: C, 49.71, H, 3.93, N, 3.12%.

*General procedure for the synthesis of 3-(arylamino)-1-ferrocenylproran-1-ols (**4a-c**)*

Alcohols **4a-c** were synthesized by the known procedure (Minić et al., 2015; Minić et al., 2017; Minić et al., 2018; Minić et al., 2019). Spectral data of compounds **4a-c** follow.

1-Ferrocenyl-3-((2-iodophenyl)amino)propan-1-ol (***4a***). Yellow oil. Yield 97%. ^{1}H NMR (200 MHz, $CDCl_3$) δ = 7.66 – 7.62 (m, 1H, CH_{Ar}), 7.24 – 7.11 (m, 1H, CH_{Ar}), 6.57 (t, *J* = 8.8 Hz, 1H, CH_{Ar}), 6.47 – 6.36 (m, 1H, CH_{Ar}), 4.52 (pseudo t, *J* = 1.9 Hz, 2H, 2 × CH_{Cp}), 4.28 – 4.21 (m, 1H, $C\underline{H}OHCH_2CH_2NH$), 4.17 (s, 7H, 7 × CH_{Cp} *overlapped signals), 3.30 – 3.27 (m, 2H, $CHOHCH_2C\underline{H_2}NH$), 2.24 – 2.12 (m, 1H, $CHO\underline{H}CH_2CH_2NH$), 2.05 – 2.01 (m, 2H, $CHOHC\underline{H_2}CH_2NH$). ^{13}C NMR (50 MHz, $CDCl_3$) δ = 147.3 (C_{Ar}), 138.9 (C_{Ar}), 129.3 (C_{Ar}), 118.4 (C_{Ar}), 110.5 (C_{Ar}), 93.3 (C_{Ar}), 85.4 (C_{Cp}), 68.3 ($\underline{C}HOH$), 68.0 (5 × C_{Cp}), 67.9 (C_{Cp}), 66.7 (C_{Cp}), 65.5 (C_{Cp}), 65.4 (C_{Cp}), 41.4 ($CHOHCH_2\underline{C}H_2NH$), 36.7 ($CHOH\underline{C}H_2CH_2NH$). IR (ATR, cm^{-1}): ν = 3280 (N-H) cm^{-1}; ν = 3074 (O-H) cm^{-1}. Anal. Calc. for $C_{19}H_{20}FeINO$: C, 49.49; H, 4.37; Fe, 12.11; I, 27.52; N, 3.04; O, 3.47. Found: C, 49.52, H, 4.31, N, 3.10%.

1-Ferrocenyl-3-((3-iodophenyl)amino)propan-1-ol (***4b***). Yellow oil. Yield 98%. ^{1}H NMR (200 MHz, $CDCl_3$) δ = 7.03 – 6.77 (m, 3H, 3 × CH_{Ar}), 6.56 – 6.45 (m, 1H, CH_{Ar}), 4.55 – 4.39 (m, 1H, $C\underline{H}OHCH_2CH_2NH$), 4.26 – 4.07 (m, 9H, 9 × CH_{Cp} *overlapped signals), 3.26 – 3.09 (m, 2H, $CHOHCH_2C\underline{H_2}NH$), 2.38 – 2.16 (m, 1H, $CHO\underline{H}CH_2CH_2NH$), 2.07 – 1.75 (m, 2H, $CHOHC\underline{H_2}CH_2NH$). ^{13}C NMR (50 MHz, $CDCl_3$) δ = 149.4 (C_{Ar}), 130.5 (C_{Ar}), 125.7 (C_{Ar}), 121.1 (C_{Ar}), 112.0 (C_{Ar}), 95.2 (C_{Ar}), 93.1 (C_{Cp}), 68.4 ($\underline{C}HOH$), 68.2 (5 × C_{Cp}), 67.9 (C_{Cp}), 67.9 (C_{Cp}), 66.6 (C_{Cp}), 65.4 (C_{Cp}), 40.9 ($CHOHCH_2\underline{C}H_2NH$), 36.6

(CHOHCH$_2$CH$_2$NH). IR (ATR, cm^{-1}): ν = 3290 (N-H) cm^{-1}; ν = 3080 (O-H) cm^{-1}. Anal. Calc. for $C_{19}H_{20}FeINO$: C, 49.49; H, 4.37; Fe, 12.11; I, 27.52; N, 3.04; O, 3.47. Found: C, 49.44, H, 4.41, N, 3.01%.

1-Ferrocenyl-3-((4-iodophenyl)amino)propan-1-ol (***4c***). Yellow solid; mp 80 °C Yield 97%. ^{1}H NMR (200 MHz, $CDCl_3$) δ = 7.39 (d, *J* = 8.6 Hz, 2H, 2 × CH$_{Ar}$), 6.37 (d, *J* = 8.6 Hz, 2H, 2 × CH$_{Ar}$), 4.55 – 4.41 (m, 1H, CHOHCH$_2$CH$_2$NH), 4.29 – 4.03 (m, 9H, 9 × CH$_{Cp}$ *overlapped signals), 3.33 – 3.07 (m, 3H, 2H, CHOHCH$_2$CH$_2$NH and 1H, CHOHCH$_2$CH$_2$NH * overlapped signals), 2.08 – 1.80 (m, 2H, CHOHCH$_2$CH$_2$NH). ^{13}C NMR (50 MHz, $CDCl_3$) δ = 147.9 (C$_{Ar}$), 135.5 (C$_{Ar}$), 115.0 (C$_{Ar}$), 93.5 (C$_{Ar}$), 85.2 (C$_{Cp}$), 68.6 (CHOH), 68.3 (5 × C$_{Cp}$), 68.1 (C$_{Cp}$), 66.8 (C$_{Cp}$), 66.7 (C$_{Cp}$), 65.3 (C$_{Cp}$), 41.2 (CHOHCH$_2$CH$_2$NH), 36.9 (CHOHCH$_2$CH$_2$NH). IR (ATR, cm^{-1}): ν = 3300 (N-H) cm^{-1}; ν = 3080 (O-H) cm^{-1}. Anal. Calc. for $C_{19}H_{20}FeINO$: C, 49.49; H, 4.37; Fe, 12.11; I, 27.52; N, 3.04; O, 3.47. Found: C, 49.53, H, 4.33, N, 3.08%.

*Synthesis of 1-aryl-4-ferrocenyl-3-phenyltetrahydropyrimidin-2(1H)-ones (**5a-c**)*

Ureas **5a-c** were synthesized by the known procedure (Minić et al., 2015; Minić et al., 2020a). Spectral data of compounds **5a-c** follow.

4-(Ferrocenyl)-1-(2-iodophenyl)-3-phenyltetrahydro-pyrimidin-2(1H)-one (***5a***). **For example ***5a*** we obtained a mixture of two atropoisomers (in the text below labeled as **5a+5a'**), therefore, most of the signals in the NMR (^{1}H NMR and ^{13}C NMR) spectra were double, which was in agreement with our previous studies (Minić et al., 2015; Minić et al., 2020).

Yellow oil. Yield 47%. Isomers ratio **5a** : **5a'** = 59.5 : 40.5 and it has been calculated based on ^{1}H NMR spectra. ^{1}H NMR (400 MHz, $CDCl_3$) δ = 7.91 – 7.84 (m, 2H, 2 × CH$_{Ar}$), 7.55 (dt, *J* = 8.7, 1.7 Hz, 3H, 3 × CH$_{Ar}$), 7.49 (dt, *J* = 6.4, 1.3 Hz, 3H, 3 × CH$_{Ar}$), 7.45 – 7.17 (m, 8H, 8 × CH$_{Ar}$), 7.09 – 6.95 (m, 2H, 2 × CH$_{Ar}$), 5.28 (pseudo t, *J* = 3.7 Hz, 1H, NCHCH$_2$CH$_2$N), 5.22 (pseudo t, *J* = 3.7 Hz, 1H, NCHCH$_2$CH$_2$N), 4.51 (dt, *J* = 2.4, 1.2 Hz, 1H, CH$_{Cp}$), 4.36 (dt, *J* = 2.4, 1.3 Hz, 1H, CH$_{Cp}$), 4.22 – 4.12 (m, 3H, 3 × CH$_{Cp}$), 4.11 – 4.09 (m, 3H, 3 × CH$_{Cp}$), 3.78 (s, 5H, 5 × CH$_{Cp}$), 3.77 (s, 5H, 5 × CH$_{Cp}$), 3.63 – 3.58 (m, 2H, NCHCH$_2$CH$_2$N), 3.45 – 3.31 (m, 2H, NCHCH$_2$CH$_2$N), 2.82 – 2.59 (m, 2H, NCHCH$_2$CH$_2$N), 2.34 – 2.16 (m, 2H, NCHCH$_2$CH$_2$N). ^{13}C NMR (101 MHz, $CDCl_3$) δ = 154.0 (NCON), 153.3 (NCON), 146.4 (C$_{Ar}$), 145.8 (C$_{Ar}$), 143.9 (C$_{Ar}$), 143.5 (C$_{Ar}$), 143.3 (C$_{Ar}$), 143.2 (C$_{Ar}$), 129.8 (C$_{Ar}$), 129.5 (C$_{Ar}$), 129.4 (C$_{Ar}$), 129.3 (C$_{Ar}$), 128.8 (C$_{Ar}$), 128.6 (C$_{Ar}$), 128.4 (C$_{Ar}$), 128.1 (C$_{Ar}$), 126.3 (C$_{Ar}$), 126.2 (C$_{Ar}$), 126.0 (C$_{Ar}$), 125.6 (C$_{Ar}$), 100.3 (C$_{Ar}$), 99.4 (C$_{Ar}$), 88.9 (C$_{Cp}$), 88.8 (C$_{Cp}$), 69.9 (5 × C$_{Cp}$), 68.9 (5 × C$_{Cp}$), 68.8 (C$_{Cp}$), 68.5 (C$_{Cp}$), 66.9 (C$_{Cp}$), 66.8 (C$_{Cp}$), 66.6 (C$_{Cp}$), 64.5 (C$_{Cp}$), 64.4 (C$_{Cp}$), 64.4 (C$_{Cp}$), 58.8 (NCHCH$_2$CH$_2$N), 58.6 (NCHCH$_2$CH$_2$N), 45.9 (NCHCH$_2$CH$_2$N), 45.8 (NCHCH$_2$CH$_2$N), 31.1 (NCHCH$_2$CH$_2$N), 31.0 (NCHCH$_2$CH$_2$N). IR (ATR, cm^{-1}): ν = 1650 (NCON) cm^{-1}. Anal. Calc. for $C_{26}H_{23}FeIN_2O$: C, 55.54; H, 4.12; Fe, 9.93; I, 22.57; N, 4.98; O, 2.85. Found: C, 55.60; H, 4.07; N, 4.94%.

4-(Ferrocenyl)-1-(3-iodophenyl)-3-phenyltetrahydro-pyrimidin-2(1H)-one (***5b***). Yellow solid; mp 103 °C. Yield 66%. ^{1}H NMR (400 MHz, $CDCl_3$) δ = 7.73 (t, *J* = 1.9 Hz, 1H, CH$_{Ar}$), 7.52 – 7.40 (m, 5H, 5 × CH$_{Ar}$), 7.31 (ddd, *J* = 8.1, 2.1, 1.0 Hz, 1H, CH$_{Ar}$), 7.28 – 7.23 (m, 1H, CH$_{Ar}$), 7.05 (t, *J* = 8.0 Hz, 1H, CH$_{Ar}$), 5.20 (pseudo t, *J* = 3.9 Hz, 1H, NCHCH$_2$CH$_2$N), 4.22 – 4.18 (m, 2H, 2 × CH$_{Cp}$), 4.16 – 4.13 (m, 1H, CH$_{Cp}$), 4.07 (dt, *J* = 2.5, 1.3 Hz, 1H, CH$_{Cp}$), 3.77 (s, 5H, 5 × CH$_{Cp}$), 3.65 (td, *J* = 11.6, 3.9 Hz, 1H, NCHCH$_2$CH$_2$N), 3.53 (m, 1H, NCHCH$_2$CH$_2$N), 2.68 – 2.57 (m, 1H, NCHCH$_2$CH$_2$N), 2.25 – 2.17 (m, 1H, NCHCH$_2$CH$_2$N). ^{13}C NMR (101 MHz, $CDCl_3$) δ = 153.6 (NCON), 145.0 (C$_{Ar}$), 143.2 (C$_{Ar}$), 134.6 (C$_{Ar}$), 134.3 (C$_{Ar}$), 129.9 (C$_{Ar}$), 128.5 (C$_{Ar}$), 128.1 (C$_{Ar}$), 126.4 (C$_{Ar}$), 124.9 (C$_{Ar}$), 93.4 (C$_{Ar}$), 88.6 (C$_{Cp}$), 68.8 (5 × C$_{Cp}$), 68.4 (C$_{Cp}$), 68.2 (C$_{Cp}$), 67.0 (C$_{Cp}$), 64.4 (C$_{Cp}$), 58.6 (NCHCH$_2$CH$_2$N), 45.6 (NCHCH$_2$CH$_2$N), 31.0 (NCHCH$_2$CH$_2$N). IR (ATR, cm^{-1}): ν = 1640 (NCON) cm^{-1}. Anal. Calc. for $C_{26}H_{23}FeIN_2O$: C, 55.54; H, 4.12; Fe, 9.93; I, 22.57; N, 4.98; O, 2.85. Found: C, 55.59; H, 4.08; N, 4.93%.

4-(Ferrocenyl)-1-(4-iodophenyl)-3-phenyltetrahydro-pyrimidin-2(1H)-one (***5c***). Yellow solid; mp 92 °C. Yield 74%. ^{1}H NMR (400 MHz, $CDCl_3$) δ = 7.63 – 7.58 (m, 2H, 2 × CH$_{Ar}$), 7.46 – 7.36 (m, 4H, 4 × CH$_{Ar}$), 7.24 – 7.19 (m, 1H, CH$_{Ar}$), 7.10 – 7.05 (m, 2H, 2 × CH$_{Ar}$), 5.17 (pseudo t, *J* = 3.9 Hz, 1H, NCHCH$_2$CH$_2$N), 4.19 – 4.14 (m, 2H, 2 × CH$_{Cp}$), 4.10 (td, *J* = 2.4, 1.3 Hz, 1H, CH$_{Cp}$), 4.04 (dt, *J* = 2.5, 1.3 Hz, 1H, CH$_{Cp}$), 3.74 (s, 5H, 5 × CH$_{Cp}$), 3.61 (td, *J* = 11.6, 3.9 Hz, 1H, NCHCH$_2$CH$_2$N), 3.53 – 3.47 (m, 1H, NCHCH$_2$CH$_2$N), 2.65 – 2.54 (m, 1H, NCHCH$_2$CH$_2$N), 2.21 – 2.14 (m, 1H, NCHCH$_2$CH$_2$N). ^{13}C NMR (101 MHz, $CDCl_3$) δ = 153.7 (NCON), 143.7 (C$_{Ar}$), 143.2 (C$_{Ar}$), 137.5 (C$_{Ar}$), 128.5 (C$_{Ar}$), 128.0 (C$_{Ar}$), 127.6 (C$_{Ar}$), 126.3 (C$_{Ar}$), 89.6 (C$_{Ar}$), 88.6 (C$_{Cp}$), 68.8 (5 × C$_{Cp}$), 68.4 (C$_{Cp}$), 68.2 (C$_{Cp}$), 66.9 (C$_{Cp}$), 64.4 (C$_{Cp}$), 58.6 (NCHCH$_2$CH$_2$N), 45.5 (NCHCH$_2$CH$_2$N), 31.0 (NCHCH$_2$CH$_2$N). IR (ATR, cm^{-1}): ν = 1645 (NCON) cm^{-1}. Anal. Calc. for $C_{26}H_{23}FeIN_2O$: C, 55.54; H, 4.12; Fe, 9.93; I, 22.57; N, 4.98; O, 2.85. Found: C, 55.58; H, 4.07; N, 4.91%.

RESULTS AND DISCUSSION

Synthesis

Within the first phase of this synthesis, we made sure to come up with an appropriate method for the synthesis of 3-(arylamino)-1-ferrocenylproran-1-ones. Our team have already designed and optimized reaction conditions for the synthesis of 3-arylamino-1-ferrocenylpropan-1-ones. On this occasion, which took place a few years ago, we managed to obtain high yields of the said compounds, and these proved to be both biological agents, as well as exquisite starting materials which can be used

for further chemical modifications (Damljanović et al., 2011; Pejović et al., 2012a; Pejović et al., 2012b; Minić et al., 2015; Minić et al., 2017; Minić et al., 2018; Minić et al., 2019; Minić et al., 2020a). In this manner, we adapted the protocol to make it suitable for the synthesis of target compounds through the usage of iodoaniline as the arylamino moiety (see Scheme 1). After setting the reaction, we were delighted to see that under these conditions we were indeed able to successfully synthesize 2-ferrocenoyl ethyl aryl amines (**3a-c**) in the yields which were satisfactory (see Scheme 1 and Scheme 2).

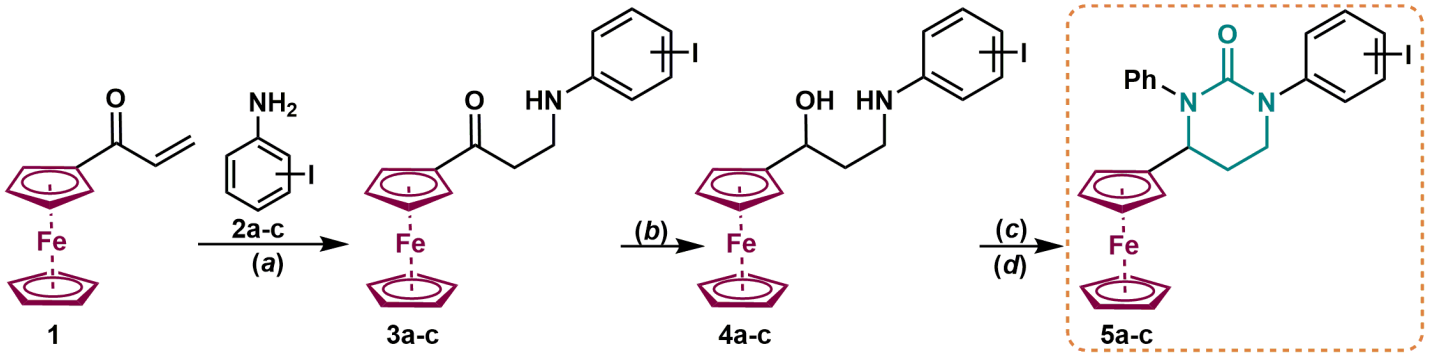

Scheme 1. Synthesis of novel Fc-containing derivatives (**3**, **4** and **5**). Reagents and conditions: (*a*) **1** (1 mmol), iodoaniline (2 mmol), montmorillonite K-10 (100 mg), ultrasound irradiation 1 h, r.t.; (*b*) **3a-c** (1 mmol), MeOH (20 ml), $NaBH_4$ (5 mmol, up to 190 mg), r.t.; (*c*) **4a-c** (1 mmol), PhNCO (0.12 ml, 1.1 equivalents), ultrasound irradiation 1 h, r.t., then (*d*) AcOH (1 ml), ultrasound irradiation 1 h, r.t.

The following step was to convert the obtained ketones **3a-c** into the 3-(arylamino)-1-ferrocenylproran-1-ols (**4a-c**). We utilized $NaBH_4$ (5 equivalents) in MeOH for this reaction and we were also able to synthesize target compounds in a successful manner. This means that we managed to obtain exquisite yields (98%), combined with a reduced reaction time and with the absence of sub products (see Scheme 1. and Scheme 2.). Our research team has previously reported on the method we utilized here (Minić et al., 2015; Minić et al., 2017; Minić et al., 2018; Minić et al., 2019; Minić et al., 2020b). It is essential to note that in organic chemistry γ-amino alcohols are generally regarded as versatile synthons. For that reason, the **4a-c** products we were able to obtain represent not only encouraging biological activity, but also remarkable starting material to be used for further synthesis of Fc-containing compounds. In this case, the focus is on an interest from a biological point of view (antibacterial, antimalarial, anti-inflammatory, antitumor etc.) (Minić et al., 2015; Minić et al., 2017; Minić et al., 2018; Minić et al., 2019; Minić et al., 2020a; Minić et al., 2020b; Pejović et al., 2015)

The last steps consisted of premising six-membered cyclic ureas **5a-c** bearing ferrocenyl group (see Scheme 1). A method which we opted for in this synthetic transformation is both efficient and involves mild reaction conditions. The method was earlier reported on by our research team (Minić et al., 2015; Minić et al., 2020a). We started the investigation by ultrasonicating the mixture of 1,3-aminoalcohol (**4a-c**) and phenyl isocyanate (0.12 ml, 1.1 mmol). In the next step, we added 1 ml of glacial acetic acid, and irradiation continued for additional 1.5 h. Through the process of purification, we were able to isolate the desired heterocyclic scaffold **5**, by using column chromatography in high purity (>95%, confirmed by NMR) and good yield (see Scheme 2). It is important to note that in the case of the example **5a** we were able to obtain the mixture of two atropoisomers (**5a+5a'**; see Scheme 2). This is the result which corresponds to previous study by our team (Minić et al., 2020a) However, regretfully, we haven't succeeded in separating these isomers.

Despite the fact that the reaction of 1,3-amino alcohols **4a-c** with phenyl isocyanate and the following intramolecular cyclization in the presence of acetic acid to cyclic ureas **5a-c** was carried out in "a one-pot" manner, we have previously established the existence of intermediates - the corresponding hydroxy ureas (**6a-c**) by carefully analyzing ^{1}H and ^{13}C NMR spectra (see Scheme 3) (Minić et al., 2015; Minić et al., 2020a).

In order to get a more comprehensive insight into the role of α-ferrocenyl carbocation, we discussed the reaction mechanism. As demonstrated in Scheme 3, the beginning of the reaction is marked by the protonation of β-hydroxy ureas **6a-c** by acetic acid and dehydration of the resulting oxonium ions **II**, eventually giving α-ferrocenyl carbocations **III** (Wagner, G., & Herrmann, R., 1995). Finally, a nucleophilic attack of the carbamide nitrogen on the positive centre of α-ferrocenyl carbocations **III** forms cations **IV**, which yielded the target 1-aryl-4-ferrocenyl-3-phenyltetrahydropyrimidin-2(1*H*)-ones after deprotonations (**5a-c**).

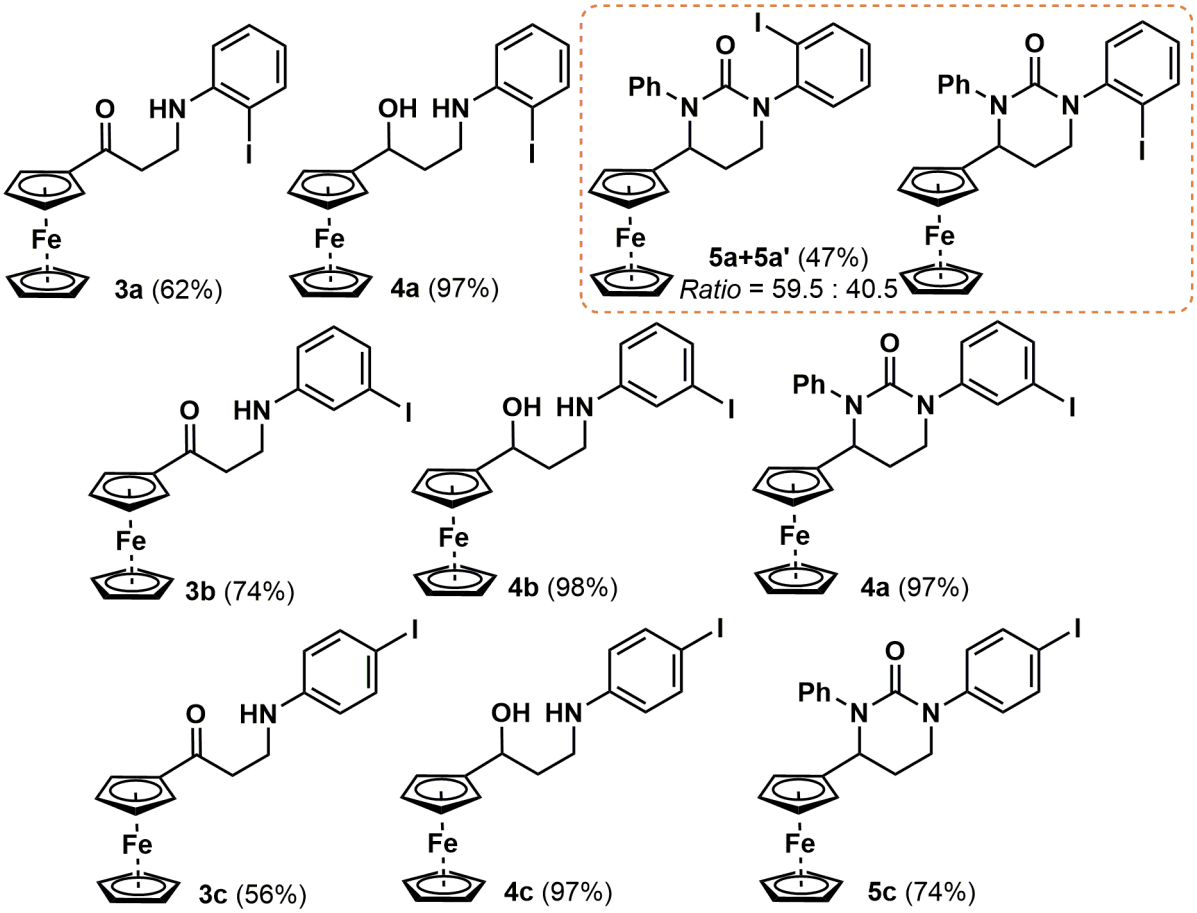

Scheme 2. An overview of newly prepared Fc-derivatives **3, 4** and **5.**

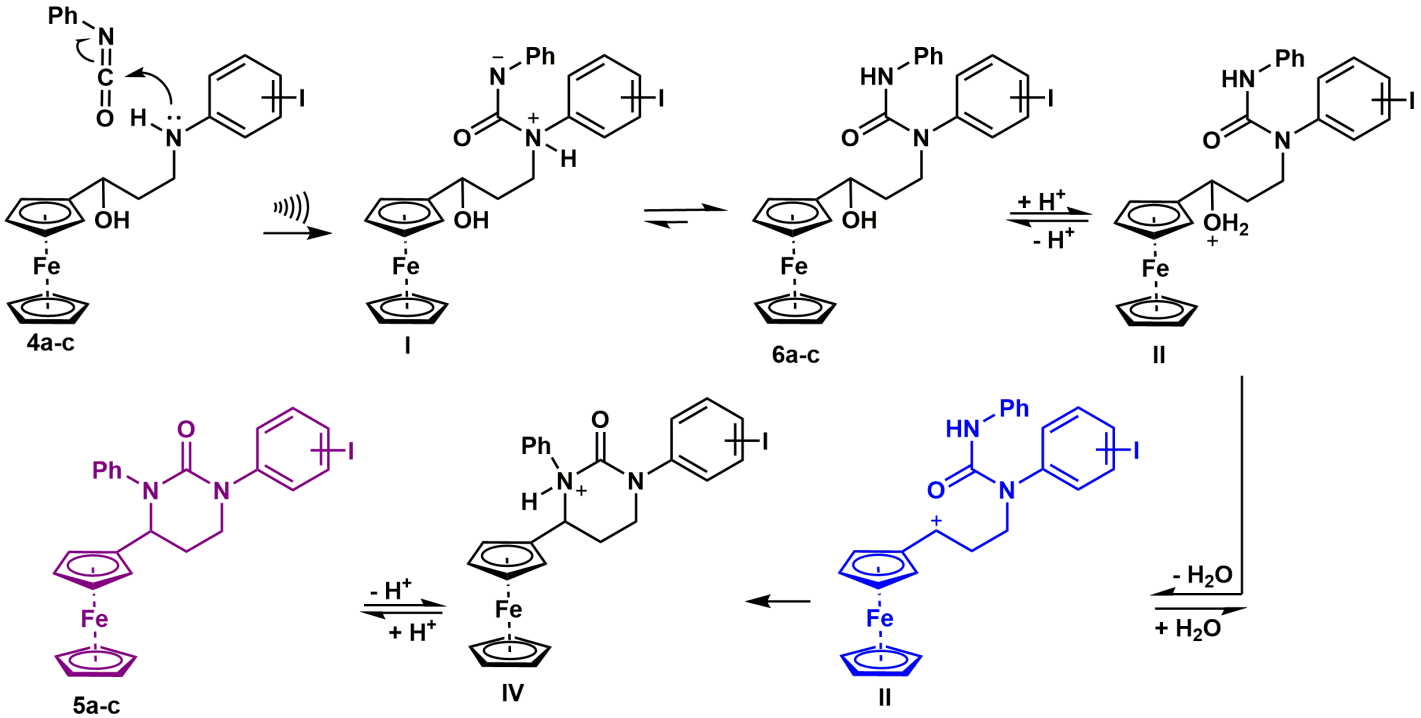

Scheme 3. A plausible reaction mechanism of the transformation of 1,3-amino alcohols **4a-c** into **5a-c.**

Spectral characterization

In order to confirm structure of the newly prepared molecules **3**, **4** and **5**, we have performed a detailed characterization by standard spectroscopic techniques (IR, ^{1}H and ^{13}C NMR), as well as elemental analyses. We have found all spectral data to be entirely compatible to the projected structures (for more data see Experimental part).

Within the IR spectra of **3a-c**, we have observed sharp, medium intensity absorption of NH stretching vibration below 3200 cm^{-1}, thereby demonstrating that all NH groups participate in H-bonding interactions. The CO stretching vibration band of the 1'-ferrocene-carbonyl group seem to be at approximately 1655 cm^{-1}. The ^{1}H and ^{13}C NMR spectra of compound **3a-c** demonstrate all the signals (for aliphatic, amino, ferrocenyl and aromatic protons) normally foreseen for the projected composition.

Infrared spectra of the Fc-containing 1,3-amino alcohols **4a-c** exhibit characteristic bands related to N-H stretching vibrations approximately 3290 cm^{-1} and O-H stretching vibrations approximately 3080 cm^{-1}. Furthermore, the lack of signal for C=O undeniably validates the occurrence of the reduction. The ^{1}H NMR spectra of **4a-c** comprises the signals which are typical of the aliphatic, hydroxy, ferrocene, amino, and aromatic protons found in the expected regions. In the ^{13}C NMR spectra of the **4a-c**, we can recognize the signals of the aliphatic, ferrocene and aromatic carbons in suitable regions. Additionally, the lack of signal which is associated with carbonyl group in ^{13}C NMR spectra of compound **4a-c** and the presence of signal at ~ 68.5 ppm, originated from CHOH, unquestionably validates the projected product structure.

The IR spectra of the obtained compound **5a-c** comprises projected bands carbonyl diamide group. In the ^{1}H NMR spectra of product mixture **5a + 5a'** the signals typical of the aromatic, ferrocene, and aliphatic protons can be found in pairs in the projected regions. The corresponding signal for compounds **5b** and **5c** has been observed, as well. In the ^{13}C NMR spectra of 1-aryl-4-ferrocenyl-3-phenyltetrahydropyrimidin-2(1*H*)-ones (**5a-c**) signals of the aliphatic, ferrocenyl, aromatic and carbonyl diamide carbons can be recognized in suitable regions (for example **5a + 5a'** the majority of the signals can be recognized in pairs).

CONCLUSION

In conclusion, this paper presents the synthesis of three novel six-membered cyclic ureas bearing a ferrocenyl core starting from appropriate 1,3-amino alcohol. The protocol used is found to be practical, as well as convenient. Structures of all newly prepared compounds were undeniably validated using the standard spectroscopic techniques and elemental analyses. Finally, we find the synthesized compounds to be of potential interest for the bioactivity studies.

ACKNOWLEDGMENTS

This work was supported by the Ministry of Education, Science and Technological development of the Republic of Serbia (Agreement No. 451-03-68/2020-14/200122).

REFERENCES

Damljanović, I., Stevanović, D., Pejović, A., Vukićević, M., Novaković, S. B., Bogdanović, G. A., Mihajilov-Krstev, M. T., Radulović, N. & Vukićević, R. D. 2011. Antibacterial 3-(arylamino)-1-ferrocenylpropan-1-ones: Synthesis, spectral, electrochemical and structural characterization. Journal of Organometallic Chemistry, 696, pp. 3703-3713. doi.org/10.1016/j.jorganchem.2011.08.016

Domling, A., Wang, W., & Wang, K., 2012. Chemistry and Biology Of Multicomponent Reactions. Chemistry Reviews, 112, pp. 3083-3135. https://doi.org/10.1021/cr100233r

Eicher, T., Hauptmann, S. & Speicher, A. 2003. The Chemistry of Heterocycles: Structure, Reactions, Syntheses, and Applications, 2nd ed., Wiiey-VCH Veriag,. doi.10.1002/352760183X

Fernandez, M. & Caballero, J. 2006. Modeling of activity of cyclic urea HIV-1 protease inhibitors using regularized-artificial neural networks, Bioorganic & Medicinal Chemistry, 16, pp. 280-294. https://doi.org/10.1016/j.bmc.2005.08.022

Hayashi, Y. 2016. Pot economy and one-pot synthesis. Chemical Science, 7, pp. 866-880. DOI: 10.1039/C5SC02913A

Kaneko, T., McMillen, W. & Lynch, M. K. 2007. Synthesis and antibacterial activity of C11, C12-cyclic urea analogues of ketolides, Bioorganic & Medicinal Chemistry Letters, 17, pp. 5013-5018. https://doi.org/10.1016/j.bmcl.2007.07.041

Kashawa, S. K., Kashawa, V., Mishra, P., Jain, N. K. & Stables, J. P. 2009. Synthesis, anticonvulsant and CNS depressant activity of some new bioactive 1-(4-substituted-phenyl)-3-(4-oxo-2-phenyl/ethyl-4H-quinazolin-3-yl)-urea, European Journal of Medicinal Chemistry, 44, pp. 4335-4343. https://doi.org/10.1016/j.ejmech.2009.05.008

Khan, S. A., Singh, N. & Saleem, K. 2008. Synthesis, characterization and in vitro antibacterial activity of thiourea and urea derivatives of steroids, European Journal of Medicinal Chemistry, 43, pp. 2272-2277. https://doi.org/10.1016/j.ejmech.2007.12.012

Li, H. Q., Zhu, T. T., Yan, T., Luo, Y. & Zhu, H. L. 2009. Design, synthesis and structure–activity relationships of antiproliferative 1,3-disubstituted urea derivatives, European Journal of Medicinal Chemistry, 44, pp. 453-459. https://doi.org/10.1016/j.ejmech.2008.04.011

Minić, A., Stevanović, D., Vukićević, M., Bogdanović, G. A., D'hooghe, M., Radulović, N. & Vukićević, R. D. 2017. Synthesis of novel 4-ferrocenyl-1,2,3,4-tetrahydroquinolines and 4-ferrocenylquinolines via α-ferrocenyl carbenium ions as key intermediates. Tetrahedron, 73, pp 6268-6274. doi. 10.1016/j.tet.2017.09.014

Minić, A., Bugarinović, J., Ilić-Komatina, D., Bogdanović, G. A., Damljanović, I. & Stevanović, D. 2018. Synthesis of novel ferrocene-containing 1,3-thiazinan-2-imines: One-pot reaction promoted by ultrasound irradiation. Tetrahedron Letters, 59, pp. 3499-3502. doi. 10.1016/j.tetlet.2018.08.029

Minić, A., Bugarinović, J., Pešić, M. & Ilić-Komatina, D. 2019. Novel 4-ferrocenyl-8-(phenylthio)-1,2,3,4-tetrahydroquinoline: design, synthesis and spectral characterization, University Thought - Publication in Natural Sciences, 9(1), pp. 38-44. DOI:10.5937/univtho9-20839

Minić, A., Stevanović, D., Damljanović, I., Pejović, A., Vukićević, M., Bogdanović, G. A., Radulović, N. & Vukićević, R. D. 2015. Synthesis of ferrocene-containing six-membered cyclic ureas via α-ferrocenyl carbocations. RSC Advances, 5, pp. 24915-24919. doi. 10.1039/C5RA01383F

Minić, A., Novaković, S. B., Bogdanović, G. A., Bugarinović, J., Pešić, M., Todosijević, A., Ilić-Komatina, D., Damljanović, I. & Stevanović, D. 2020a. Synthesis and structural characterizations of novel atropoisomeric ferrocene-containing six-membered cyclic ureas, Polyhedron, 177 pp. 114316. https://doi.org/10.1016/j.poly.2019.114316

Minić, A., Van de Walle, T., Van Hecke, K., Combrinck, J., Smith, P. J., Chibale, K. & D'hooghe, M. 2020b. Design and synthesis of novel ferrocene-quinoline conjugates and evaluation of their electrochemical and antiplasmodium properties, European Journal of Medicinal Chemistry, 187, pp. 111963. https://doi.org/10.1016/j.ejmech.2019.111963

Motokura, K., Fujita, N., Mori, K., Mizugaki, T., Ebitani, K. & Kaneda, K. 2005. An Acidic Layered Clay Is Combined with A Basic Layered Clay for One-Pot Sequential Reactions. Journal of the American Chemical Society, 127, pp. 9674-9675. https://doi.org/10.1021/ja052386p

Nicolaou, K. C., Edmons, D. J. & Bulger, P. G. 2006. Cascade Reactions in Total Synthesis. Angewandte Chemie International Edition, 45, pp. 7134-7186. https://doi.org/10.1002/anie.200601872

Pejović, A., Stevanović, D., Damljanović, I., Vukićević, M., Novaković, S. B., Bogdanović, G. A., Mihajilov-Krstev, M. T., Radulović, N. & Vukićević, R. D. 2012a. Ultrasound-assisted synthesis of 3-(arylamino)-1-ferrocenylpropan-1-ones. Helvetica Chimica Acta, 95, pp. 1425-1441. doi.org/10.1002/hlca.201200009

Pejović, A., Damljanović, I., Stevanović, D., Vukićević, M., Novaković, S. B., Bogdanović, G. A., Radulović, N. & Vukićević, R. D. 2012b. Antimicrobial ferrocene containing quinolinones: Synthesis, spectral, electrochemical and structural characterization of 2-ferrocenyl-2,3-dihydroquinolin-4(1H)-one and its 6-chloro and 6-bromo derivatives, Polyhedron, 31, pp. 789-795. https://doi.org/10.1016/j.poly.2011.11.006

Pejović, A., Damljanović, I., Stevanović, D., Minić, A., Jovanović, J., Mihailović, V., Katanić, J. & Bogdanović, G. A. 2017. Synthesis, characterization and antimicrobial activity of novel ferrocene containing quinolines: 2-ferrocenyl-4-methoxyquinolines, 1-benzyl-2-ferrocenyl-2,3-dihydroquinolin-4(1H)-ones and 1-benzyl-2-ferrocenylquinolin-4(1H)-ones, Journal of Organometallic Chemistry, 846, pp. 6-17. http://dx.doi.org/10.1016/j.jorganchem.2017.05.051

Pejović, A., Minić, A., Bugarinović, J., Pešić, M., Damljanović, I., Stevanović, D., Mihailović, V., Katanić, J. & Bogdanović, G. A. 2018a. Synthesis, characterization and antimicrobial activity of novel 3-ferrocenyl-2-pyrazolyl-1,3-thiazolidin-4-ones, Polyhedron, 155, pp. 382-389. https://doi.org/10.1016/j.poly.2018.08.071

Pejović, A., Minić, A., Jovanović, J., Pešić, M., Ilić Komatina, D., Damljanović, I., Stevanović, D., Mihailović, V., Katanić, J. & Bogdanović, G. A. 2018b. Synthesis, characterization, antioxidant and antimicrobial activity of novel 5-arylidene-2-ferrocenyl-1,3-thiazolidin-4-ones, Journal of Organometallic Chemistry, 869, pp. 1-10. https://doi.org/10.1016/j.jorganchem.2018.05.014

Pejović, A., Danneels, B., Desmet, T., Cham, B. T., Nguyen, T., Radulović, N.S., Vukićević, R. D. & D'hooghe, M. 2015. Synthesis and Antimicrobial/Cytotoxic Assessment of Ferrocenyl Oxazinanes, Oxazinan-2-ones, and Tetrahydropyrimidin-2-ones, Synlett, 26, pp. 1195-1200. doi. 10.1055/s-0034-1380348

Sarma, R., Sarmah, M. M., & Prajapati, D., 2012a. Microwave-Promoted Catalyst- and Solvent-Free Aza-Diels–Alder Reaction of Aldimines with 6-[2-(Dimethylamino)vinyl]-1,3-dimethyluracil. Journal of Organic Chemistry, 77, pp. 2018-2023. https://doi.org/10.1021/jo202346w

Sharma, A., Appukkuttan, P., & Van der Eycken, E. V., 2012b. Microwave-assisted synthesis of medium-sized heterocycles. Chemical Communications, 48, pp. 1623-1637. DOI: 10.1039/C1CC15238F

Taylor, A. P., Robinson, R. P., Fobian, Y. M., Blakemore, D. C., Jones, L. H. & Fadeyi, O. 2016. Modern advances in heterocyclic chemistry in drug discovery. Organic & Biomolecular Chemistry, 14, pp. 6611-6637. doi.10.1039/C6OB00936K

Tale, R. T., Rodge, A. H., Hatnapure, G. D., & Keche, A. P. 2011. The novel 3,4-dihydropyrimidin-2(1H)-one urea derivatives of N-aryl urea: Synthesis, anti-inflammatory, antibacterial and antifungal activity evaluation, Bioorganic & Medicinal Chemistry Letters, 21, pp. 4648-4651. https://doi.org/10.1016/j.bmcl.2011.03.062

Wagner, G., & Herrmann, R., 1995. Chiral Ferrocene Derivatives, An Introduction, in Ferrocenes: Homogenous Catalysts, Organic Synthesis, Material Science, ed. A. Togni and T. Hayashi, VCH, Weinheim, pp. 175-178.

Yang, B., Tao, C., Shao, T., Gong, J., & Che, C., 2016. One-pot synthesis of tetracyclic fused imidazo[1,2-a]pyridines *via* a three-component reaction. Beilstein Journal of Organic Chemistry, 12, pp 1487-1492. doi:10.3762/bjoc.12.145

Bulletin of Natural Sciences Research
Vol. 11, No. 1, 2021, pp. 24-28.

DOI: https://doi.org/10.5937/bnsr11-30567
Original Scientific Paper

SYNTHESIS AND CHARACTERIZATION OF COPPER(II) COMPLEX WITH 2,6-DIACETYLPYRIDINE-BIS(PHENYLHYDRAZONE)

SVETLANA BELOŠEVIĆ[1], MIRJANA M. RADANOVIĆ[2*], MARKO V. RODIĆ[2], VUKADIN M. LEOVAC[2]

[1]Faculty of Technical Sciences, University of Priština in Kosovska Mitrovica, Serbia
[2]Faculty of Sciences, University of Novi Sad, Novi Sad, Serbia

ABSTRACT

The syntheses, physicochemical and structural properties of the novel Cu(II) complex with 2,6-diacetylpyridine bis(phenylhydrazone) (L), of the formula $[CuL_2]Br_2$ are presented. In the reaction of warm MeOH solutions of the ligand, 2,6-diacetylpyridine bis(phenylhydrazone) and $CuBr_2$ in molar ratio 2:1 resulted in formation of black single crystals of the bis(ligand) complex. This is the first Cu(II) complex with this ligand that is characterized by SC-XRD. Two ligand molecules are coordinated in the usual tridentate mode, *via* nitrogen atoms of the pyridine ring, and two azomethine nitrogen atoms, forming distorted octahedral environments of the metal ion.

Keywords: Metal complex, Hydrazone, 2,6-diacetylpyridine derivative, Structure determination.

INTRODUCTION

For a few decades now, hydrazones are interesting field of research due to their good chelating properties (Kitaev & Buzykin, 1974; Kogan et al., 1990; Watanabe et al., 2018), but the pharmacological activity, as well. The research has shown that some compounds from this group have promising antibacterial, antifungal and antitumor activities (Ainscough et al., 1998; Avaji et al., 2009; Azaz et al., 2007; Mahalingam et al., 2008; Wang et al., 2007), and some of their derivatives are suggested as reagents for the treatment of genetic and neurodegenerative disorders, such as thalassemic syndrome and Alzheimer's (Armstrong et al., 2003; Bernhardt et al., 2007; Buss et al., 2005; Donnelly et al., 2008). Besides, some of these compounds are used as highly sensitive analytical reagents, luminescent probes and molecular sensors (ávila Terra et al., 2002; Bakir et al., 2008; Basu et al., 2007; Pinto et al., 2004; Sreeja et al., 2003).

2,6-Diacetylpyridine bis(hydrazones) are especially interesting because of their versatile coordination chemistry, i.e., they can act as ligands of different denticity (from tridentate to heptadentate). Even though a large number of metal complexes with this ligand group is synthesized, the number of those that are structurally characterized is rather small (Groom et al., 2016). Since the presence of metal center could often enhance the properties of the organic ligand, even improve its biological activity, it is significant thoroughly to examine the coordination properties of this ligand class, and the structures of the obtained complexes.

Lately, one of these ligands, 2,6-diacetylpyridine bis(phenylhydrazone) (L) became the topic of our research, thus the crystal structure of the first metal complex, $[CoL_2]I_2$, was determined (Belošević et al., 2018). In this paper the synthesis, some physicochemical properties, as well as molecular, and crystal structure of copper complex with the same ligand, of the formula $[CuL_2]Br_2$ is reported.

EXPERIMENTAL

Materials and methods

All chemicals used were commercial products of analytical reagent grade, except for the ligand, 2,6-diacetylpyridine-bis(phenylhydrazone), which was synthesized as described previously (Belošević et al., 2018). Elemental analyses (C, H, N) of air-dried complexes were carried out by standard micromethods in the Center for Instrumental Analyses, ICTM in Belgrade. Molar conductivities of freshly prepared complexes solutions ($c = 1\times10^{-3}$ mol dm^{-3}) were measured on a Jenway 4010 conductivity meter. IR spectra were recorded using KBr pellets on a NEXUS 670 FTIR spectrophotometer (Thermo Nicolet) in the range of 4000–400 cm^{-1}. Melting points were measured on a Nagema melting point microscope Rapido.

Synthesis of complex

The mixture of 0.024 g $CuBr_2$ (0.1 mmol) and 0.068 g (0.2 mmol) of L was heated in 5 cm^3 of MeOH until complete dissolution. The obtained dark solution was left at the room temperature and evaporated to a small volume. After 50 h black prismatic single crystals were filtered and washed with MeOH. Yield: 0.033 g (31 %). Anal. Calcd. for $[C_{42}H_{42}CuN_{10}]Br_2$ (Mr = 910.21): C, 55.42; H, 4.66; N, 15.39. Found: C, 55.98; H, 4.52; N, 15.82. IR bands [$\tilde{\nu}$ /cm^{-1}]: 3440vs, 3157w, 3100w, 2938w, 1634w, 1599s, 1520m,

*Corresponding author: mirjana.lalovic@dh.uns.ac.rs

1494m, 1444w, 1380w, 1264m, 1170w, 1092w, 807w, 750m, 696m, 503w. M.p. = 234 °C. Molar conductivity, Λ_M (S cm^2 mol^{-1}): 120 (DMF).

Crystal structure determination

Diffraction data were collected on an Oxford Diffraction Gemini S diffractometer equipped with a Sapphire3 CCD area detector. Graphite monochromatized Mo *Kα* radiation was employed. Data reduction was performed with the *CrysAlisPro* software (Rigaku Oxford Diffraction, 2015). The crystal structure was solved by *SHELXT* (Sheldrick, 2015b), and refined with the *SHELXL-2018* (Sheldrick, 2015a). The *ShelXle* (Hübschle et al., 2011) was used as graphical user interface for crystal structure refinement procedures. Additional calculations were performed the *SHAPE* (Llunell et al., 2013) and *CrystalExplorer* (Turner et al., 2017).

CCDC 2059113 contains the supplementary crystallographic data for this paper. The data can be obtained free of charge from The Cambridge Crystallographic Data Centre via https://www.ccdc.cam.ac.uk/structures/.

Table 1. Crystallographic data and refinement statistics.

Crystal data	
Chemical formula	$[C_{42}H_{42}CuN_{10}]Br_2$
M_r (g cm^{-3})	910.21
Crystal system	Monoclinic
Space group	*C*2/*c*
Temperature (K)	294
a (Å)	20.7769(5)
b (Å)	15.8668(4)
c (Å)	11.8754(3)
β (°)	91.864(2)
V (Å^3)	3912.81(17)
Z	4
Crystal size (mm)	0.50 × 0.31 × 0.19
Data collection	
Diffractometer	Gemini S (Oxford Diffraction)
Radiation type	Mo *Kα*
No. of measured reflections	9140
No. of independent reflections	4491
No. of observed [$I > 2\sigma(I)$] reflections	3453
R_{int}	0.021
$(\sin\theta/\lambda)_{max}$ (Å^{-1})	0.683
μ (mm^{-1})	2.646
Absorption correction	Analytical
T_{min}, T_{max}	0.481, 0.693
Refinement	
No. of reflections	4491
No. of parameters	259
No. of restraints	0
H-atom treatment	Mixed
$R[F^2 > 2\sigma(F^2)]$	0.035
$wR(F^2)$	0.088
S	1.03
$\Delta\rho_{max}$, $\Delta\rho_{min}$ (e Å^{-3})	0.35, −0.66

RESULTS AND DISCUSSION

Synthesis and physicochemical characterization of the complex

The reaction of warm methanolic solution of $CuBr_2$ and the ligand in molar ratio 1:2 yielded in formation of prismatic single crystals of the complex $[CuL_2]Br_2$.

The obtained complex is stable in air and high temperatures. It is well soluble in DMF, and partially soluble in alcohols and H_2O. Molar conductivity of its DMF solution has a value characteristic for 2:1 electrolyte type, thus is in concordance with the coordination formula (Geary, 1971).

In the IR spectrum of the complex the band found at 1520 cm^{-1} could be ascribed to ν(C=N) vibrations of the imine group. In the spectrum of the ligand, this band is found at higher wavenumbers (1563 cm^{-1}), and due to coordination has suffered a negative shift (Curry et al., 1967; Kazak et al., 2009). The band at 3157 cm^{-1} corresponds to ν(NH) vibrations, while the other bands in the range above 2900 cm^{-1} originate from valent ν(CH) vibrations of CH_3-groups and aromatic rings (pyridine and benzene). Bands at 1599 and 1494 cm^{-1} are the result of ν(C=C), ν(C=N) vibrations of the mentioned aromatic rings.

Crystal structure of the complex

The complex $[CuL_2]Br_2$ is isostructural with $[CoL_2]I_2$ (Belošević et al., 2018). Both complexes crystallize in *C*2/*c* space group, with very similar unit cell parameters. Complex cation $[CuL_2]^{2+}$ is situated on a two-fold rotation axis, so that the asymmetric unit of the unit cell is comprised of a ligand molecule, half of a copper atom, and a bromide ion (Figure 1). To facilitate structural comparisons of $[CuL_2]Br_2$ and $[CoL_2]I_2$, pertinent structural parameters of both complexes are listed in Table 2. Coordination environment around Cu(II) is heavily distorted, and calculation of continuous shape measure (*CShM*) assigned the coordination polyhedron as heavily distorted octahedron, with *CShM*(*OC*-6)=5.911 (Alvarez et al., 2005). The coordination environment is formed by two meridionally arranged tridentate N_3 chelate ligands. Dihedral angle enclosed by planes through N1, N2A and N2B donor atoms of the symmetry-related ligands amounts 74.2°. Distortion of the octahedron may be seen through valance angles centered on Cu(II) atom, all of which deviate from ideal values. The largest deviations are observed by The *trans*-valence angle N2A–Cu1–N2A and *cis*-valence angles N1–Cu1–N2A, N1–Cu1–N2B with values of 150.69(7)°, 74.14(7)°, and 76.56(8)°, respectively.

The coordination mode of the ligand, through nitrogen atoms of the pyridine ring, and two azomethine nitrogen atoms, is identical to that found in $[CoL_2]I_2$ (Belošević et al., 2018), and $[ZnL'_2](CF_3O_3S)_2$, where L' is structurally related ligand 2,6-diformylpyridine bis(phenylhydrazone) (Dumitru et al., 2009).

Table 2. Selected bond lengths (Å), and valence angles (°).

	$[CuL_2]Br_2$	$[CoL_2]I_2$
Bonds	Length (Å)	
M–N1	1.9451(18)	2.0061(18)
M–N2B	2.2170(18)	2.1993(19)
M–N2A	2.3736(18)	2.3057(19)
N1–C3	1.346(3)	1.338(3)
N1–C7	1.357(3)	1.346(3)
C2–C3	1.469(3)	1.467(3)
C7–C8	1.468(3)	1.465(4)
N2A–C2	1.292(3)	1.298(3)
N2B–C8	1.291(3)	1.302(3)
N2A–N3A	1.373(3)	1.374(3)
N2B–N3B	1.369(3)	1.366(3)
N3A–C10A	1.388(3)	1.390(3)
N3B–C10B	1.395(3)	1.400(4)
Bonds	Angle (°)	
N1–Cu1–N1^{i}	173.87(11)	173.26(10)
N2A–Cu1–N2B	150.69(7)	152.17(7)
N1–Cu1–N2A	74.14(7)	74.69(7)
N1–Cu1–N2B	76.56(8)	77.51(7)

Metal–ligand bond lengths are in the range of 1.9451(18)– 2.3736(18) Å, with Co–N1 being the shortest one. Also, the two phenylhydrazine moieties are asymmetrically coordinated, as indicated by different metal–ligand bond lengths (Table 2). These structural features are analogous to those found in $[CoL_2]I_2$. Intra-ligand bond lengths and comparable to those found in $[CoL_2]I_2$. Intra-ligand bonds with localized double character are N2–C2 and N2–C8, while others are in the expected range for sp^2 hybridized atoms, with considerable electron delocalization.

Crystal packing in $[CuL_2]Br_2$ (Figure 1c) is congruent to that of $[CoL_2]I_2$. Its investigation by method of Hirshfeld surface (HS) analysis documents striking similarity between $[CuL_2]Br_2$ and $[CoL_2]I_2$. Namely, cations HS decomposition into atom-specific contacts (Fig. 2), reveals following distribution: 68.2% of H···H contacts (68.4% for $[CoL_2]I_2$), 13.7% of C···H or H···C contacts (13.2% for $[CoL_2]I_2$), and 13.5 of H···I contacts (13.6% for $[CoL_2]I_2$). As expected, and analogous with results for $[CoL_2]I_2$, the anion's HS is 99.6% mapped with Br···H contacts.

The bromide ion is involved in two hydrogen bonds, with very similar geometry (Table 3).

Table 3. Selected hydrogen-bond parameters.

D–H···*A*	*D*–H (Å)	H···*A* (Å)	*D*···*A* (Å)	*D*–H···*A* (°)
N3A–H3A···Br1^{i}	0.81(3)	2.64(3)	3.440(2)	168(3)
N3B–H3B···Br1	0.82(3)	2.64(3)	3.456(2)	169(3)

Symmetry code(s): (i) $-x+1, y, -z+1/2$.

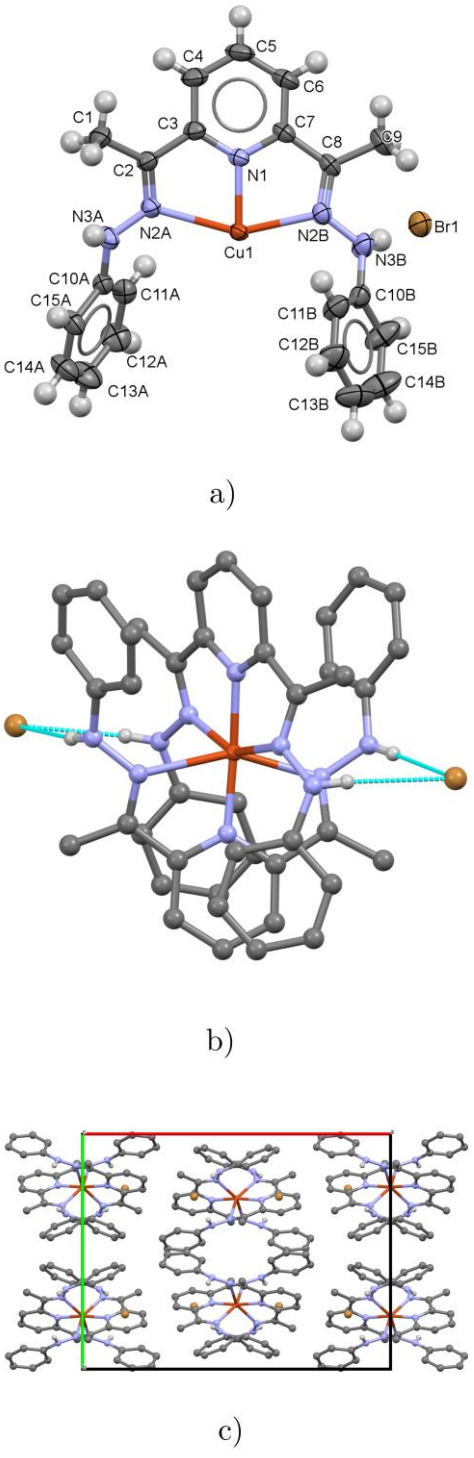

Figure 1. Asymmetric unit (a) and formula unit (b) of $[CoL_2]I_2$; c) Crystal packing viewed along crystallographic *c* axis (hydrogen atoms are omitted for clarity).

CONCLUSION

In this paper sythesis, structure, and some physicochemical properties of the novel complex with 2,6-diacetylpyridine bis(phenylhydrazone), of the formula $[CuL_2]Br_2$, are described. This is only the second structurally

characterized metal complex with this ligand, and since this class of compounds is promising from the many point of views it is of a high importance to make some further research in this field.

ACKNOWLEDGMENTS

The authors acknowledge financial support of the Ministry of Education, Science and Technological Development of the Republic of Serbia (Grant No . 451-03-9/2021-14/ 200125).

REFERENCES

Ainscough, E. W., Brodie, A. M., Dobbs, A. J., Ranford, J. D. & Waters, J. M. 1998. Antitumour copper(II) salicylaldehyde benzoylhydrazone (H_2sb) complexes: Physicochemical properties and the single-crystal X-ray structures of [{Cu(H_2sb)(CCl_3CO_2)$_2$}$_2$] and [{Cu(Hsb)(ClO_4)(C_2H_5OH)}$_2$]. Inorganica Chimica Acta, 267(1), pp. 27-38. https://doi.org/10.1016/s0020-1693(97)05548-5

Alvarez, S., Alemany, P., Casanova, D., Cirera, J., Llunell, M. & Avnir, D. 2005. Shape maps and polyhedral interconversion paths in transition metal chemistry. Coordination Chemistry Reviews, 249(17-18 SPEC. ISS.), pp. 1693-1708. https://doi.org/10.1016/j.ccr.2005.03.031

Armstrong, C. M., Bernhardt, P. V., Chin, P. & Richardson, D. R. 2003. Structural variations and formation constants of first-row transition metal complexes of biologically active aroylhydrazones. European Journal of Inorganic Chemistry, 2003(6), pp. 1145-1156. https://doi.org/10.1002/ejic.200390146

Avaji, P. G., Vinod Kumar, C. H., Patil, S. A., Shivananda, K. N. & Nagaraju, C. 2009. Synthesis, spectral characterization, in-vitro microbiological evaluation and cytotoxic activities of novel macrocyclic bis hydrazone. European Journal of Medicinal Chemistry, 44(9), pp. 3552-3559. https://doi.org/10.1016/j.ejmech.2009.03.032

Ávila Terra, L. H. S., Guekezian, M., Gaubeur, I., Matos, J. R. & Suárez-Iha, M. E. V. 2002. Synthesis, characterization, properties and thermal study of nickel(II)/di-2-pyridyl ketone benzoylhydrazone complex. Polyhedron, 21(23), pp. 2375-2380. https://doi.org/10.1016/S0277-5387(02)01185-3

Azaz, A. D., Celen, S., Namli, H., Turhan, O., Kurtaran, R., Kazak, C. & Arslan, N. B. 2007. Synthesis, crystal structure and biological activity of the nickel(II) complex of 2,6-diacetylpyridinedihydrazone. Transition Metal Chemistry, 32(7), pp. 884-888. https://doi.org/10.1007/s11243-007-0242-2

Bakir, M., Green, O. & Mulder, W. H. 2008. Synthesis, characterization and molecular sensing behavior of [ZnCl2(η3-N,N,O-dpkbh)] (dpkbh = di-2-pyridyl ketone benzoyl hydrazone). Journal of Molecular Structure, 873(1–3), pp. 17-28. https://doi.org/10.1016/j.molstruc.2007.03.001

Basu, C., Chowdhury, S., Banerjee, R., Stoeckli Evans, H. & Mukherjee, S. 2007. A novel blue luminescent high-spin iron(III) complex with interlayer O-H···Cl bridging: Synthesis, structure and spectroscopic studies. Polyhedron, 26(14), pp. 3617-3624. https://doi.org/10.1016/j.poly.2007.03.053

Belošević, S., Rodić, M., Radanović, M., & Leovac, V. 2018. Synthesis and structure of cobalt(II) complex with 2,6-diacetylpyridine-bis(phenylhydrazone). The University Thought - Publication in Natural Sciences, 8(2), pp. 33-38. https://doi.org/10.5937/univtho8-19451

Bernhardt, P. V., Chin, P., Sharpe, P. C. & Richardson, D. R. 2007. Hydrazone chelators for the treatment of iron overload disorders: Iron coordination chemistry and biological activity. Dalton Transactions, 30, pp. 3232-3244. https://doi.org/10.1039/b704102k

Buss, J. L., Greene, B. T., Turner, J., Torti, F. M. & Torti, S. V. 2005. Iron chelators in cancer chemotherapy. Current Topics in Medicinal Chemistry, 4(15), pp. 1623-1635. https://doi.org/10.2174/1568026043387269

Curry, J. D., Robinson, M. A. & Busch, D. H. 1967. Metal complexes derived from substituted hydrazones of 2,6-diacetylpyridine. Inorganic Chemistry, 6(8), pp. 1570-1574. https://doi.org/10.1021/ic50054a032

Donnelly, P. S., Caragounis, A., Du, T., Laughton, K. M., Volitakis, I., Cherny, R. A., Sharples, R. A., Hill, A. F., Li, Q. X., Masters, C. L., Barnham, K. J. & White, A. R. 2008. Selective intracellular release of copper and zinc ions from bis(thiosemicarbazonato) complexes reduces levels of Alzheimer disease amyloid-β peptide. Journal of Biological Chemistry, 283(8), pp. 4568-4577. https://doi.org/10.1074/jbc.M705957200

Dumitru, F., Legrand, Y.-M., Barboiu, M., Petit, E. & Lee, A. van der. 2009. Metallosupramolecular architectures of pseudoterpyridine-type ligands and Zn^{II} metal ions. Crystal Growth & Design, 9(6), pp. 2917-2921. https://doi.org/10.1021/cg9002466

Geary, W. J. 1971. The use of conductivity measurements in organic solvents for the characterisation of coordination compounds. Coordination Chemistry Reviews, 7(1), pp. 81-122. https://doi.org/10.1016/S0010-8545(00)80009-0

Groom, C. R., Bruno, I. J., Lightfoot, M. P. & Ward, S. C. 2016. The Cambridge Structural Database. Acta Crystallographica Section B Structural Science, Crystal Engineering and Materials, 72(2), pp. 171-179. https://doi.org/10.1107/S2052520616003954

Hübschle, C. B., Sheldrick, G. M. & Dittrich, B. 2011. ShelXle: A Qt graphical user interface for SHELXL. Journal of Applied Crystallography, 44(6), pp. 1281-1284. https://doi.org/10.1107/S0021889811043202

Kazak, C., Arslan, N. B., Karabulut, S., Azaz, A. D., Namlı, H. & Kurtaran, R. 2009. Supramolecular lead(II) azide complex of 2,6-diacetylpyridine dihydrazone: synthesis, molecular structure, and biological activity. Journal of Coordination Chemistry, 62(18), pp. 2966-2973. https://doi.org/10.1080/00958970902980537

Kitaev, I. & Buzykin, B. 1974. Gidrazony. Moscow: Nauka.

Kogan, V. A., Zelentsov, V. V., Larin, G. M., Lukov, V. V. 1990. Kompleksy perekhodnykh metallov c gidrazomani. Moscow: Nauka.

Llunell, M., Casanova, D., Cirera, J., Alemany, P. & Alvarez, S. 2013.SHAPE (2.1), Universitat de Barcelona, Barcelona,

Mahalingam, V., Chitrapriya, N., Fronczek, F. R., & Natarajan, K. 2008. New Ru(II)-dmso complexes with heterocyclic hydrazone ligands towards cancer chemotherapy. Polyhedron, 27(7), pp. 1917-1924. https://doi.org/10.1016/j.poly.2008.02.036

Pinto, J. J., Moreno, C., & García-Vargas, M. 2004. A very sensitive flow system for the direct determination of copper in natural waters based on spectrophotometric detection. Talanta, 64(2), pp. 562-565. https://doi.org/10.1016/j.talanta.2004.03.009

Rigaku Oxford Diffraction. 2015. CrysAlisPro Software system (1.171.38.46).

Sheldrick, G. M. 2015a. Crystal structure refinement with SHELXL. Acta Crystallographica Section C Structural Chemistry, 71(1), pp. 3-8. https://doi.org/10.1107/S2053229614024218

Sheldrick, G. M. 2015b. SHELXT - Integrated space-group and crystal-structure determination. Acta Crystallographica Section A Foundations and Advances, 71(1), pp. 3-8. https://doi.org/10.1107/S2053273314026370

Sreeja, P. B., Sreekanth, A., Nayar, C. R., Prathapachandra, M. R., Usman, K. A., Razak, I. A., Chantrapromma, S. & Fun, H. K. 2003. Synthesis, spectral studies and structure of 2-hydroxyacetophenone nicotinic acid hydrazone. Journal of Molecular Structure, 645(2-3), pp. 221-226. https://doi.org/10.1016/S0022-2860(02)00563-X

Turner, M. J., McKinnon, J. J., Wolff, S. K., Grimwood, D. J., Spackman, P. R., Jayatilaka, D. & Spackman, M. A. 2017. CrystalExplorer17 (No. 17). University of Western Australia.

Wang, B. dui, Yang, Z. Y., Crewdson, P., & Wang, D. qi. 2007. Synthesis, crystal structure and DNA-binding studies of the Ln(III) complex with 6-hydroxychromone-3-carbaldehyde benzoyl hydrazone. Journal of Inorganic Biochemistry, 101(10), pp. 1492-1504. https://doi.org/10.1016/j.jinorgbio.2007.04.007

Watanabe, K., Mino, T., Yoshida, Y. & Sakamoto, M. 2018. Hydrazone-palladium catalyzed reactions using allyl compounds. Journal of Synthetic Organic Chemistry, Japan, 76(8), pp. 828-837. https://doi.org/10.5059/yukigoseikyokaishi.76.828

Bulletin of Natural Sciences Research
Vol. 11, No. 1, 2021, pp. 29-37.
DOI: https://doi.org/10.5937/bnsr11-30488
Original Scientific Paper

ISO CLUSTER CLASSIFIER BY ARCGIS FOR UNSUPERVISED CLASSIFICATION OF THE LANDSAT TM IMAGE OF REYKJAVÍK

POLINA LEMENKOVA[1*]

[1]Schmidt Institute of Physics of the Earth, Russian Academy of Sciences. Department of Natural Disasters, Anthropogenic Hazards and Seismicity of the Earth. Laboratory of Regional Geophysics and Natural Disasters. Moscow, Russian Federation

ABSTRACT

The paper presents the use of the Landsat TM image processed by the ArcGIS Spatial Analyst Tool for environmental mapping of southwestern Iceland, region of Reykjavik. Iceland is one of the most special Arctic regions with unique flora and landscapes. Its environment is presented by vulnerable ecosystems of highlands where vegetation is affected by climate, human or geologic factors: overgrazing, volcanism, annual temperature change. Therefore, mapping land cover types in Iceland contribute to the nature conservation, sustainable development and environmental monitoring purposes. This paper starts by review of the current trends in remote sensing, the importance of Landsat TM imagery for environmental mapping in general and Iceland in particular, and the requirements of GIS specifically for satellite image analysis. This is followed by the extended methodological workflow supported by illustrative print screens and technical description of data processing in ArcGIS. The data used in this research include Landsat TM image which was captured using GloVis and processed in ArcGIS. The methodology includes a workflow involving several technical steps of raster data processing in ArcGIS: 1) coordinate projecting, 2) panchromatic sharpening, 3) inspection of raster statistics, 4) spectral bands combination, 5) calculations, 6) unsupervised classification, 7) mapping. The classification was done by clustering technique using ISO Cluster algorithm and Maximum Likelihood Classification. This paper finally presents the results of the ISO Cluster application for Landsat TM image processing and concludes final remarks on the perspectives of environmental mapping based on Landsat TM image processing in ArcGIS.The results of the classification present landscapes divided into eight distinct land cover classes: 1) bare soils; 2) shrubs and smaller trees in the river valleys, urban areas including green spaces; 3) water areas; 4) forests including the Reykjanesfólkvangur National reserve; 5) ice-covered areas, glaciers and cloudy regions; 6) ravine valleys with a sparse type of the vegetation: rowan, alder, heathland, wetland; 7) rocks; 8) mixed areas. The final remarks include the discussion on the development of machine learning methods and opportunities of their technical applications in GIS-based analysis and Earth Observation data processing in ArcGIS, including image analysis and classification, mapping and visualization, machine learning and environmental applications for decision making in forestry and sustainable development.

Keywords: Machine learning, Landsat TM, ArcGIS, Cartography.

INTRODUCTION

The paper presents the use of the Landsat TM image processed by the ArcGIS Spatial Analyst Tool for raster data processing, band calculations and classification. The Landsat TM imagery presents so far one of the most widely used launched programs on satellite based Earth Observation.

The Landsat was launched in July 23, 1972 under the name of Earth Resources Technology Satellite (ERTS-1), and then renamed as Landsat 1 in 1975. Since then the Landsat TM satellite images continues to play an important role in remote sensing domain as an open source reliable data (Woodcock et al., 2008; Zhu et al., 2019). As a result of such successful development, by January 1, 2015 the USGS Landsat archive already contained an impressive data pool of 5.5 million images with a global coverage and open access availability (Wulder et al., 2016).

Due to its availability and quality, the analysis of the Landsat TM data presents a variety of existing applications (Cao et al., 2020; Lemenkova, 2011, 2015, 2020c, 2020d; Foga et al., 2017; Nagol et al., 2015; Healey et al., 2018; Chowdhury et al., 2021; Homer et al., 2015). With a history of nearly 50 years of continuous global data collection, the Landsat mission has a constant development. Current version include Landsat-8 which is on-orbit and a Landsat-9 which is being still under development (Wulder et al., 2019).

Applications of the Landsat TM imagery for remote sensing based mapping are constantly developing due to the actuality of the environmental monitoring in the land planning and policy issues (Flood, 2013). A thorough review summarizing current status of remote sensing of forests and

* Corresponding author: pauline.lemenkova@gmail.com

forest dynamics using Landsat TM imagery collection is given by Banskota et al. (2014).

A new approach of Landsat TM images processing is introduced by Kennedy et al. (2010) to extract spectral trajectories of land surface change from yearly Landsat time-series stacks to extract temporal trajectories of spectral data on a pixel-by-pixel basis.

The application of ArcGIS based analysis of the habitat and agricultural crops using Landsat 8 by Maximum Likelihood algorithm of the supervised classification is presented by Herbei & Sala (2016). Examples of other application of the Landsat TM are given by a variety of papers (Townshend et al., 2012; Lemenkova, 2011, 2014a, 2014b, 2016; Qiu et al., 2019; Goodwin et al., 2013; Vermote et al., 2016) that were considered in this study.

GIS analysis and remote sensing (RS) methods are effective tools for thematic mapping of forest changes enabling better understanding of environmental dynamics (Valjarević et al., 2018). On the other hand, modelling and artificial computer based simulations support GIS research being integral to mapping, graphical visualization and plotting (Schenke & Lemenkova, 2008; Lindh et al., 2000). Modelling can be applied for the ecological management, mapping, and visualization of crucial information necessary for sustainable environmental prognosis (Vuollekoski et al., 2015). Furthermore, RS applications are applied in predictive modelling, analysis of water quality, and studies on global adaptation to climate change (Tomaszkiewicz et al., 2015).

Using machine learning (ML) algorithms in Remote Sensing (RS) data processing, such as ISO cluster classifier is an effective, accurate and promising tool enabling to perform automatic land cover mapping. A wide variety ofdisciplinesin Earth sciences apply advanced ML methods for data processing (Zhong & Zhang, 2012; Lindh & Winter, 2003; Lemenkova, 2019b). These include such domains as landscape studies, geology, environment, remote sensing, marine and ocean research and civil engineering to mention a few (Valjarević et al., 2020; Lindh, 2001, 2004; Lemenkova, 2019c, 2019d). Application of ML for environmental research presents a promising interdisciplinary approach and contributes to the existing regional environmental studies of Iceland (Thórhallsdóttir, 1996; Brombacher et al., 2020).

GIS-based analysis is incorporated into environmental studies for a variety of mapping purposes. For instance, thematic maps depicting the exposure to agricultural pesticides for large areas are produced to alert environmentalists in areas affected by pesticides, and to estimate high-resolution GIS information for pesticides-related health problems (Wan, 2015). Maps based on specific remote sensing data pertaining to various cartographic operations, such as satellite image classification or assessment dynamics of land cover types in various years, are necessary to assist environmentalists in the actual decision making process regarding nature conservation.

Due to the variety of existing GIS software, a selection of suitable tool is necessary to apply its technical functionality to the performed operations in image processing and visualization for environmental analysis. For this reason, this paper used ArcGIS as suitable and powerful tool for image processing and processed Landsat TM image of Reykjavik by a combination of spectral and panchromatic bands for cartographic visualization and presented an ISO cluster classifier classification of the study area to analyse spatial distribution of the land cover types.

STUDY AREA

Environmental setting

The study area encompasses the southwestern part of Iceland with its capital Reykjavík (Figure 1). The characteristics of the vulnerable Arctic ecosystems in Arctic Iceland include the resilience of the highland environment to external impact factors including those of climate, human or geologic character (e.g. annual temperature change, overgrazing or local volcanism in the seismically active areas). Among the environmental factors, important conditions are created by geological setting, e.g. volcanism and local hydrogeology which controls the glacial landscape evolution and finally results in the modern topography by sculpturing geomorphic landforms (Robinson et al., 2008).

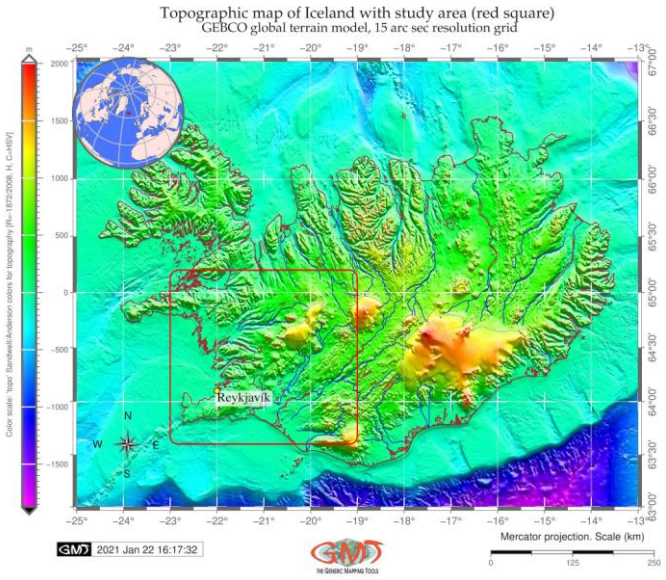

Figure 1. Topographic map of Iceland. Source: author.

The landscapes in Iceland have unique features due to the mixed flora that includes elements from Greenland, Scandinavia and Europe. Therefore, the vegetation of Iceland differs from other part of Arctic and Subarctic (Steindórsson, 1962; Kristinsson, 1986). Mapping such a unique region implies a contribution to nature conservation with regards to the protected areas and or threatened species in Arctic.

The relationship between the relief, geologic strata characteristics and climate factors is finally reflected in the vegetation coverage. Since the geology of Iceland has some specifics due to the volcanic activities (Jakobsson, 1979; Jakobsson et al., 2008), the vegetation has a unique character due to the underdeveloped soil layer. Volcanic conditions in

the region create special condition of the erosion-prone sandy and volcanic soils where only specific types of plants can exist (Arnalds et al., 2001, 2003).

In turn, the surficial geological processes are reflected in a modern glacial land system context through the glacier dynamics, ablation, ice cover fluctuation under the impact of the climate changes and shaping the glacier terrains (Krüger, 1994). For instance, glaciers and ice sheets largely contribute to the sediment deposition through the processes of erosion and deposition of massive quantities of debris. Besides, subglacial meltwater exerts a control on ice dynamics and sediment transport (Gerrard, 1985; Russell et al., 2006).

Anthropogenic activities

Apart from the geological and physical geographic factors, the nature of Iceland experiences certain impacts of the anthropogenic origin. More specifically, land use pressure in Iceland is mostly caused by the intense agricultural activities and cattle grazing. Thus, the degree of degradation in Iceland has been assessed in various studies with the aim of the ecosystem change studies (Gísladóttir, 2001; Greipsson, 2012).

Environmental significance of lands using GIS for environmental monitoring plays a crucial role in decision making and land policy (Klaučo et al., 2013a, 2013b). Among other factors, the selection of the advanced tools for data processing and visualization is important. Using GIS analysis of the satellite imagery of the Landsat TM proposes an effective tool for automated data processing especially useful for the regions with harsh climate conditions. This study presents the Landsat TM image processing by using ArcGIS.

METHODOLOGY

Data Capture and Software

The Landsat TM scene was taken from the USGS Global Visualization Viewer (GloVis), an online search and order tool for selected remote sensing data (Figure 2).

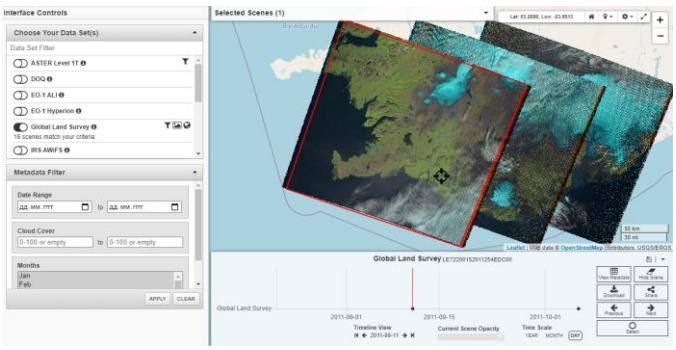

Figure 2. Data capture through the GloVis repository.

The geographic map of the study area (Figure 1) was plotted using the GMT scripting cartographic toolset (Wessel & Smith, 1995) using GEBCO high-resolution raster map (GEBCO Compilation Group, 2020) by existing methods of GMT (Lemenkova, 2019a, 2020a, 2020b, 2020c) consisting in scripting approach in cartographic visualization. The main cartographic workflow was performed in an ArcGIS, a widely used GIS in geosciences (Suetova et al., 2005a, 2005b; Klaučo et al., 2014, 2017).

Data Preprocessing

Before the image processing, a cartographic coordinate re-projection was performed (Figure 3). The World Geodetic SystemW GS-1984 Zone 27 was changed to the local GCS_Reykjavik_1900 EPSG:4657 with accuracy 10.0 m, which has following WGS 84 bounds: -24.66°W, 63.34N to -13.38°W, 66.59N and a center coordinate -19.02378948° 64.96335686° which is suitable for mapping of Iceland (Figure 3).

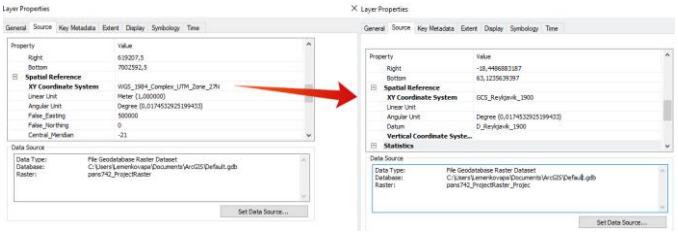

Figure 3. Change of coordinate system WGS84 UTM_27N to GCS_Reykjavik_1900 in ArcGIS.

This coordinate system is maintained by the Landmaelingar Islands (National Survey of Iceland).

Image pan-sharpening

The next step includes a procedure of the pan-sharpening which has been performed using ArcGIS menu with a following path:

ArcToolbox> Data Management Tools> Raster>Raster Processing> Create Pan-sharpened Raster Dataset (Figure 4).

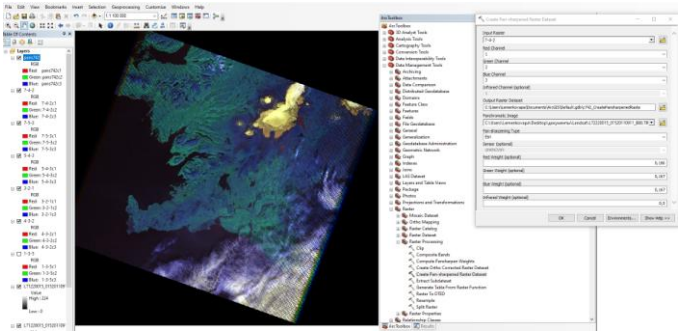

Figure 4. Pan-sharpening Landsat TM by a combination of spectral and panchromatic bands. Source: author.

The pan-sharpening (panchromatic sharpening) of the Landsat TM satellite image follows the principle of taking the best qualities of each band to achieve a better output result.

More specifically, it is a technique that combines the high-resolution panchromatic band with a high level of precision (panchromatic band has a resolution of 15 m per pixel, which is twice as detailed as the individual spectral bands) with the lower-resolution yet color information of spectral bands (30 m resolution in visible bands). Such a combination provides a more detailed and precise image, as shown in Figure 4. The pan-sharpening type was selected as ESRI and a band combination is 7-4-2.

Other parameters for the pan-sharpening include nearest resampling method, and creating pyramids for quicker raster processing. The cartographic coordinate system is PROJCS [WGS-1984 Zone 27N], geographic Transformation NAD_1927_To_NAD_1983_NADCON (North American Datum). These and other technical details were checked up in Compute Pan-sharpen Weights menu, as well as Calculate Statistics and Get Raster Properties menus of Data Management Tools of the ArcGIS.

Hence, the precision was set up as the highest (Figure 4). The raster statistics and properties after the pan-sharpening are checked by the menu of ArcGIS (Figure 5).

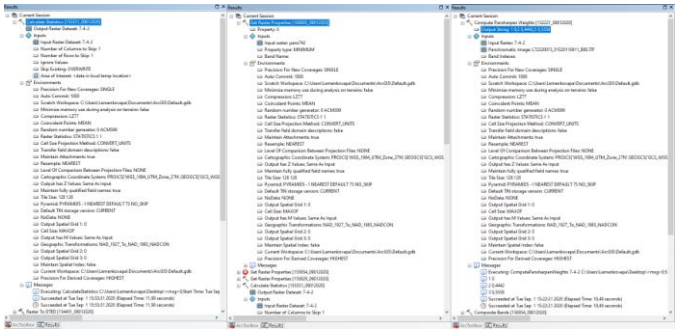

Figure 5. Raster statistics after pan-sharpening.

ISO Cluster Classifier

The next step included an unsupervised classification by ISO Cluster Classifier using ArcGIS (Figure 6 and 8).

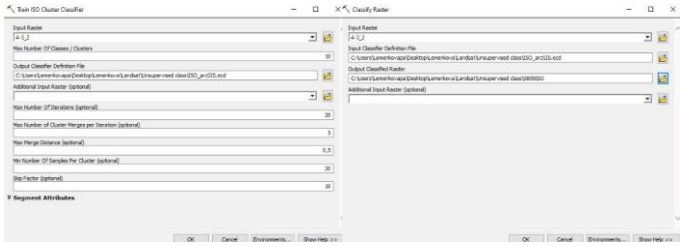

Figure 6. Menu of Spatial Analyst Tools, Segmentation and Classification, ArcGIS. Source: author.

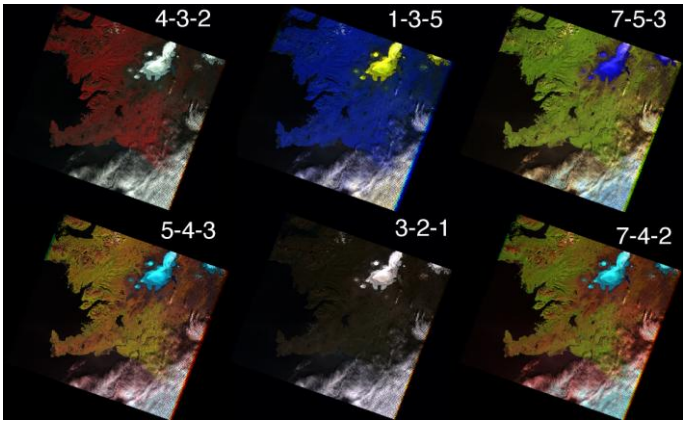

Figure 7. Color composites of the Landsat TM 7 bands in ArcGIS. Source: author.

Various methods of satellite image processing exist and described in the literature (Abburu & Golla, 2015; Schowengerdt, 2007; Lemenkova, 2013a). Due to the benefits of image classification, it is common for remote sensing analysis to adopt various existing approaches of classification (both supervised and unsupervised) of Landsat TM image. Among the variety of classification methods one should mention the following ones: unsupervised K-mean and ISODATA, random trees, supervised learning methods such as vector machine classifier, maximum likelihood to mention a few.

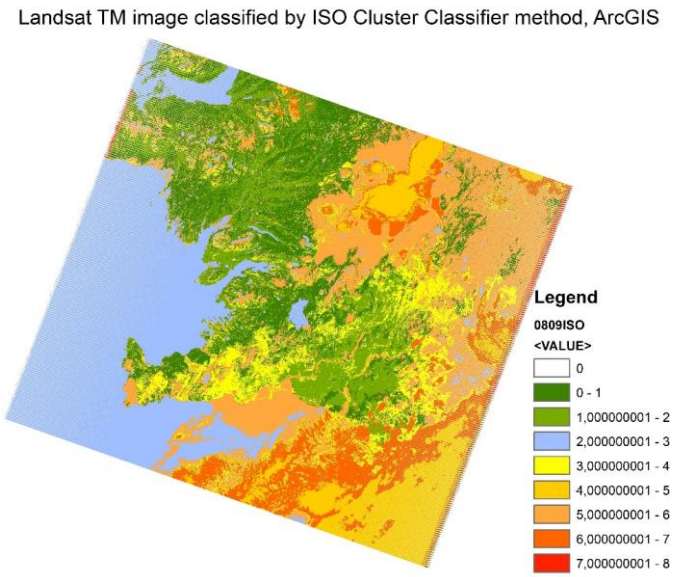

Figure 8. Results of the ISO Cluster Classifier classification, ArcGIS. Source: author.

The ISO Cluster Classifier was selected in this research due to its straightforward and machine-based approach with minimized human intervention. The menu of the selected parameter is presented in Figure 6. First, the Train ISO Cluster Classifier was performed in the selected color composite bands with the created output file ISO_arcGIS.ecd, which is an ESRI classifier definition file (Figure 6, left).

Using this file, the ArcGIS classifies a raster dataset inputs using the generated ecd file which contains all the information to perform an ESRI-supported classification (Figure 6, right). After that, the image was processed using the embedded algorithm of ESRI (Figure 8).

RESULTS AND DISCUSSION

Image analysis

The unsupervised classification made using ArcGIS used archived, high-resolution pan-sharpened Landsat TM 7 satellite image to classify and distinguish where vegetated habitats, urban areas, and bare soils exist and if vegetation areas can be separated into several sub-classes. The research focused on the region bordered by 18°-24°W, 63°-65.2°N and includes Reykjanesfólkvangur National reserve with various land cover types that include volcanic products (lava formations and crater lakes), bird cliffs and geothermic fields. The impact of volcanism was detected in the origfin of dust

sources in the soils of Icelands, which includes basaltic volcanic glass (Arnalds, 2004, 2010).

Another special object includes the Þingvallavatn (Thingvallavatn), a rift valley lake in 21,09°W, 64,11°N. With a surface of 84 km² it is the largest natural lake in Iceland of volcanic origin with the greatest depth at 114 m located near the Thingvellir National Park. The geologic setting includes cracks and faults with the Almannagjá ravine as the largest. North of Reykjavik there is a 30-km long Hvalfjörður fjord which was clearly detected on the image together with other water areas.

Interpretation of color compositions

The unsupervised classification

The original Landsat TM image was processed and color composites were created using various band combinations (Figure 7). A variety of band combinations provide additional information on the objects that can be highlighted by the correct colors.

When interpreting the results of the land cover classification it can be discovered that classifying spectral reflectance of pixels by the machine learning made fewer errors comprehending land cover types and distinguishing betwen landscape classes than it did with human-based GIS classification (e.g. supervised learning methods). Thus, as can be seen in Figure 7, the color composite 4-3-2 (upper row, left in Figure 7) provides a false color composite suitable for detecting vegetation coverage.

- An effective composition is achieved by the bands 1-3-5 (upper row, center in Figure 7). that gives the bright yellow color for the ice-covered regions, which can be suitable for glaciological studies, e.g. assessment of glacier retreats by comparison of ice coverage in various dates. Such a bright highlighting of glaciers can be distinguished on the image and processed further by methods of image classification.
- The ‘natural with atmospheric removal’ is achieved by combination of 7-5-3 (upper row, right in Figure 7).
- The false color composite (Figure 7) uses a band combination 4-3-2 where the vegetation performs in bright crimson red colors.
- The color infrared (vegetation) composition is achieved by 5-4-3 bands (lower row, left in Figure 7).
- The behavior similar to this band composition can be seen on a combination 7-4-2 (lower row, right in Figure 7). The difference between the both consists in brighter and greener (more natural-looking) vegetation in the 7-4-2 composition.
- The combination of natural colors is achieved by the bands of 3-2-1 (lower row, center in Figure 7).

Unsupervised classification

The unsupervised classification based on the color composites does not require creating training points and is a fully machine learning approach (Figure 8). The clustering algorithms here was used to build training sites for a without using field survey data. The advantage of the Iso Cluster approach consists in its combination of the functionalities of the Iso Cluster and Maximum Likelihood Classification. The output classified raster implies creating of the signature file.

As evident in Figure 8 (Results of the ISO Cluster Classifier classification), a high degree of distinguisheability in classes of land cover types used in a landscape context reflects spectral reflectance properties of various surfaces on Earth. The ISO Cluster unsupervised classifier is based on the nine selected classes of which eights classes represent ‘land cover types’ and one class shows technical ‘no values’ for the rest of the pixels (this corresponds to the technical noises on the images).

This study considered published literature on remote sensing and environmental mapping that described the standardised approaches to land cover types detection and interpreting the results. The resulting 8 classes (plus the ‘no data’ class colored by white areas) are well associated with the land cover types distributed over the area of Reykjavik and surroundings (Figure 8).

1. The first class (dark green colors) is classified as bare soils.
2. The second class (light green colors) shows shrubs and smaller trees mostly located in the river valleys, as well as urban areas including green spaces.
3. The third class (blue color) clearly detected water areas.
4. The forth class (yellow colors) shows forest areas: for instance, the Reykjanesfólkvangur National reserve is included in this class.
5. The fifth class (sandy beige color) means ice-covered areas and cloudy regions on the image. This class also includes some misclassified types of vegetation and water areas with high spectral reflectance that can be assigned to these classes.
6. The sixth class (beige color) shows the ravine valleys with a special, mostly sparse type of the vegetation distributed over the study area: rowan, alder, heathland, wetland and other and other similar types of grasses, e.g. Nootka lupin (Lupinusnootkatensis), distributed due to the limited soil development in Iceland and Nordic climate.
7. The seventh class (orange color) shows bare rocks.
8. The eights class (crimson red color) has a very rare occurrence and mostly shows mixed areas of the land cover types.

The demonstrated benefit of machine learning in ArcGIS based environmental studies is that resulting map is more accurate, objective and independent in terms of interpreting land cover types than when applying human based supervised classification methods for image processing. The study shown that complex and heterogeneous landscapes may be classified with the improved technical options of ArcGIS that include both cartographic and remote sensing functionality available in ArcToolbox of ArcGIS.

DISCUSSION

Perspectives

In Iceland, vegetation distribution can be qualitatively differentiated and have a wide variety of types. These inlcude rocky landscapes, ice-covered areas, volcanic sands and water bodies. Using spectral data of these land cove types can support environmental monitoring. In contrast, selected land cover types (vegetation types) could not be classified and they are merged with other land cover types due to the spectral reflectance properties similar to these types. This highlights the importance of sufficient information for a better classification. This can includespecial data on forest types and clarity of image with regards to cloudiness.

The study has implications for the monitoring, conservation and management of land cover types in southwestern coastal region of Iceland around Reykjavik and other vegetated habitats. The results presented a map of the land cover types based on the unsupervised classification (a machine learning approach) performed in ArcGIS Desktop 10.7 Spatial Analyst. The study provided a land cover types map with eight machine-separated classes, and a classification framework using a 'Train IDSO Cluster Classifier'. This approach requires no fieldwork neither creating training samples, that is, a fully machine-based classification of the Landsat TM satellite image.

Recommendations

The dominant vegetation types along the southwestern shores of Iceland can further be selected using the datasets on biogeographical patterns in the native flora of Iceland. In Iceland, there are 438 species in the vascular flora (Kristinsson, 2008; Wasowicz et al., 2014). Computer-based image classification ishighly valuable for environmental mapping of the distribution of the vegetation types.

The distribution of vegetation on the one hand depends on the variety of factors including climatic, topographic, social (urban areas), geomorphological (slope steepness), and geological (bedrock types) variables. On the other hand, vegetation serves as a significant indicator of healthy ecosystem, since it provides essential functions (e.g. habitat) in a complexity of its functioning. Therefore, testing various methods and applications of land cover mapping is crucial and recommended both for the regional development of the environmental protection in Arctic and for the technical testing of ArcGIS functionality in thematic mapping and remote sensing applications.

Core advantages of machine learning methods in remote sensing and GIS over traditional methods – such as the speed of classification with which land cover maps can be generated automatically by the machine, as well as the automated adjustment of distinguishable color palettes of land classes for display in ArcGIS mapping – have been maximized significantly owing to technological changes in GIS development in recent years.

CONCLUSION

This study assessed the effectiveness of using the Landsat TM image for the automatic classification of the land cover types in Iceland using ArcGIS. The automation in Earth observation studies is based on using machine learning (ML) algorithm of data recognition and processing. The advantages of the automatization in cartographic studies consists in the reduced human-prone errors, increased speed of data processing and correctness of the final output.

The combination of the satellite spectral data from Landsat TM imagery in ArcGIS demonstrated classification of the scenes for environmental monitoring and land policy analysis in high Arctic regions. In addition, the combination of spectral bands effectively demonstrated the possibility of the Landsat TM for highlighting selected objects of interest and detecting land cover types (e.g. ice coverage, land and water areas, agricultural crop fields).

Although visible bands of the Landsat TM have a moderate accuracy (30 m), the addition of the panchromatic band when combined with other Landsat bands enables to increase the accuracy and resolution of the image through the pan-sharpening, as demonstrated. The paper also showed the workflow of the ArcGIS for projecting coordinates with regard to the study location (GCS_Reykjavik_1900). The ArcGIS is a powerful GIS both for vector and raster data processing. It includes a wide variety of tools for mapping and cartographic analysis.

Selected pixels or small-scale areas can still be misclassified because of the proximity of spectral reflectance properties in objects making difficult to distinguish between various vegetation types. However, the presented approach can detect the most significant spectral signatures, such as land cover types both in urban and in forest-covered areas of the region of Reykjavik. An ISO Cluster approach to classify the image composed of the three spectral bands is a promising approach for land cover types mapping.

Because Iceland is one of the most special Arctic regions with unique flora and landscapes, it presents opportunities for land cover studies based on Landsat TM classifications. Hence, it is important toperform an ArcGIS-based Landsat TM image processing that visualizespresent land cover patterns around Reykjavik and enables monitoring land cover changesin similar research usingseveral Landsat TM scenes.

The present study employed reliable Landsat TM data and ArcGIS methodology to perform an ISO Cluster classification of land cover types in Reykjavik area. This study presented mapping land cover types using ArcGIS by the unsupervised classification approach. The methodology includes several print screens illustrating workflow which can be repeated in similar research in the future. This study contributes both to the regional Arctic studies of Iceland and to the technical testing of the cartographic functionality of ArcGIS with a special focus on remote sensing data.

ACKNOWLEDGMENTS

The author thanks the reviewers and editor for the review, critical remarks, suggestions and editing of this manuscript.

REFERENCES

Abburu, S. & Golla, S. B. 2015. Satellite Image Classification Methods and Techniques: A Review, International Journal of Computer Applications, 119(8), pp. 20-25. https://doi.org/10.5120/21088-3779

Arnalds, O., Gisladottir, F. & Sigurjonsson, H. 2001. Sandy deserts of Iceland: an overview, Journal of Arid Environments, 47, pp. 359-371. https://doi.org/10.1006/jare.2000.0680

Arnalds, O. & Barkarson, B. H. 2003. Soil erosion and land use policy in Iceland in relation to sheep grazing and government subsidies, Environmental Science & Policy, 6(1), pp. 105-113. https://doi.org/10.1016/S1462-9011(02)00115-6

Arnalds, O. 2004. Volcanic soils of Iceland. Catena 56, pp. 3-20. https://doi.org/10.1016/j.catena.2003.10.002

Arnalds, O. 2010. Dust sources and deposition of aeolian materials in Iceland. Icelandic Agricultural Sciences 23(1), pp. 3-21.

Banskota, A., Kayastha, N., Falkowski, M. J., Wulder, M. A., Froese, R. E. & White, J. C. 2014. Forest Monitoring Using Landsat Time Series Data: A Review. Canadian Journal of Remote Sensing, 40, pp. 362-384. https://doi.org/10.1080/07038992.2014.987376

Brombacher, J., Reiche, J., Dijksma, R. & Teuling, A. J. 2020. Near-daily discharge estimation in high latitudes from Sentinel-1 and 2: A case study for the Icelandic Þjórsá river, Remote Sensing of Environment, 241, pp. 111684. https://doi.org/10.1016/j.rse.2020.111684

Cao, Z., Ma, R., Duan, H., Pahlevan, N., Melack, J., Shen, M. & Xue, K. 2020. A machine learning approach to estimate chlorophyll-a from Landsat-8 measurements in inland lakes, Remote Sensing of Environment, 248, pp. 111974.

Chowdhury, S., Peddle, D. R., Wulder, M. A., Heckbert, S., Shipman, T. C. & Chao, D. K. 2021. Estimation of land-use/land-cover changes associated with energy footprints and other disturbance agents in the Upper Peace Region of Alberta Canada from 1985 to 2015 using Landsat data, International Journal of Applied Earth Observation and Geoinformation, 94, 102224. https://doi.org/10.1016/j.jag.2020.102224

Flood, N. 2013. Seasonal composite Landsat TM/ETM+ images using the medoid (a multi-dimensional median), Remote Sensing, 5, pp. 6481-6500. https://doi.org/10.3390/rs5126481

Foga, S., Scaramuzza, P. L., Guo, S., Zhu, Z., Dilley, R. D., Beckmann, T., Schmidt, G. L., Dwyer, J. L., Joseph Hughes, M. & Laue, B. 2017. Cloud detection algorithm comparison and validation for operational Landsat data products. Remote Sensing of Environment, 194, pp. 379-390. https://doi.org/10.1016/j.rse.2017.03.026

GEBCO Compilation Group 2020. GEBCO 2020 Grid. https://doi.org/10.5285/a29c5465-b138-234d-e053-6c86abc040b9

Gerrard, A. J. 1985. Soil erosion and landscape stability in southern Iceland: a tephrochronological approach. 18 pp. In: K.S. Richards, R.R. Arnett, S. Ellis (eds.). Geomorphology and Soils. 1st Ed. London, Routledge https://doi.org/10.4324/9780429320781

Gísladóttir, G. 2001. Ecological Disturbance and Soil Erosion on Grazing Land in Southwest Iceland, Land Degradation. Springer, pp. 109-126. https://doi.org/10.1007/978-94-017-2033-5_7

Goodwin, N. R., Collett, L. J., Denham, R. J., Flood, N. & Tindall, D. 2013. Cloud and cloud shadow screening across Queensland, Australia: an automated method for Landsat TM/ETM+ time series. Remote Sensing of Environment, 134, pp. 50-65. https://doi.org/10.1016/j.rse.2013.02.019

Greipsson, S. 2012. Catastrophic soil erosion in Iceland: impact of long-term climate change, compounded natural disturbances and human driven landuse changes, Catena, 98, pp. 41-54. https://doi.org/10.1016/j.catena.2012.05.015

Healey, S. P., Cohen, W. B., Yang, Z., Brewer, C. K., Brooks, E. B., Gorelick, N., Hernandez, A. J., Huang, C., Hughes, M. J., Kennedy, R. E., Loveland, T. R., Moisen, G. G., Schroeder, T. A., Stehman, S. V., Vogelmann, J. E., Woodcock, C. E., Yang, L. & Zhu, Z. 2018. Mapping forest change using stacked generalization: An ensemble approach. Remote Sensing of Environment, 204, 717-728. https://doi.org/10.1016/j.rse.2017.09.029

Herbei, M. & Sala, F. 2016. Classification of Land and Crops Based on Satellite Images Landsat 8: Case Study SD Timisoara, Bulletin UASVM series Agriculture, 73(1), pp. 29-34. https://doi.org/10.15835/buasvmcn-agr:12007

Homer, C. G., Xian, G., Aldridge, C. L., Meyer, D. K., Loveland, T. R. & O'Donnell, M. S. 2015. Forecasting sagebrush ecosystem components and greater sage-grouse habitat for 2050: Learning from past climate patterns and Landsat imagery to predict the future, Ecological Indicators, 55, 131-145. https://doi.org/10.1016/j.ecolind.2015.03.002

Jakobsson, S. P. 1979. Outline of the petrology of Iceland, Jökull, 29, pp. 57-73.

Jakobsson, S. P., Jonasson, K. & Sigurdsson, I. A. 2008. The tree igneous rock series of Iceland, Jökull, 58, pp. 117-138.

Kennedy, R. E., Yang, Z. & Cohen, W. B. 2010. Detecting trends in forest disturbance and recovery using yearly Landsat time series: 1. LandTrendr – Temporal segmentation algorithms, Remote Sensing of Environment, 114, pp. 2897-2910. https://doi.org/10.1016/j.rse.2010.07.008

Klaučo, M., Gregorová, B., Stankov, U., Marković, V. & Lemenkova, P. 2013a. Interpretation of Landscape Values, Typology and Quality Using Methods of Spatial Metrics for Ecological Planning, Environmental and Climate Technologies, October 14, 2013. Riga, Latvia. https://doi.org/10.13140/RG.2.2.23026.96963

Klaučo, M., Gregorová B., Stankov U., Marković V. & Lemenkova P. 2013b. Determination of ecological significance based on geostatistical assessment: a case study from the Slovak Natura 2000 protected area, Open Geosciences, 5(1), pp. 28-42. https://doi.org/10.2478/s13533-012-0120-0

Klaučo, M., Gregorová, B., Stankov, U., Marković, V. & Lemenkova, P. 2014. Landscape metrics as indicator for ecological significance: assessment of Sitno Natura 2000 sites, Slovakia, Ecology and Environmental Protection, Minsk, Belarus, pp. 85-90. https://doi.org/10.6084/m9.figshare.7434200

Klaučo, M., Gregorová, B., Koleda, P., Stankov, U., Marković, V. & Lemenkova, P. 2017. Land planning as a support for

sustainable development based on tourism: A case study of Slovak Rural Region, Environmental Engineering and Management Journal, 2(16), pp. 449-458. https://doi.org/10.30638/eemj.2017.045

Kristinsson, H. 1986. A guide to the flowering plants and ferns of Iceland. Reykjavik: Mál og menning. https://doi.org/10.1111/j.1756-1051.1991.tb01794.x

Kristinsson, H. 2008. Íslenskt Plöntutal: Blómplöntur og byrkningar. Fjölrit náttúrufræðistofnunar, 51, pp. 1-58.

Krüger, J. 1994. Glacial processes, sediments, landforms and stratigraphy in the terminus region of Mýrdalsjökull, Iceland. Folia Geographica Danica, 21, pp. 1-233.

Lemenkova, P. 2011. Seagrass Mapping and Monitoring Along the Coasts of Crete, Greece. M.Sc. Thesis. University of Twente, Faculty of Earth Observation and Geoinformation (ITC), Enschede, Netherlands. https://doi.org/10.13140/RG.2.2.16945.22881

Lemenkova, P. 2013a. Monitoring Changes in Agricultural Landscapes of Central Europe, Hungary: Application of ILWIS GIS for Image Processing, Geoinformatics: Theoretical and Applied Aspects, 13–16 May, Ukraine, Kiev. https://doi.org/10.3997/2214-4609.20142479

Lemenkova P 2014a. Opportunities for Classes of Geography in the High School: the Use of 'CORINE' Project Data, Satellite Images and IDRISI GIS for Geovisualization. In: Perspectives for the Development of Higher Education. Belarus, Grodno, pp. 284-286. https://doi.org/10.6084/m9.figshare.7211933

Lemenkova P. 2014b. Detection of Vegetation Coverage in Urban Agglomeration of Brussels by NDVI Indicator Using eCognition Software and Remote Sensing Measurements. In: GIS and Remote Sensing, November 17–19, 2014, Tsaghkadzor, pp. 112-119. https://doi.org/10.6084/m9.figshare.743421

Lemenkova, P. 2015. Analysis of Landsat NDVI Time Series for Detecting Degradation of Vegetation, Geoecology and Sustainable Use of Mineral Resources. From Science to Practice, Belgorod, Russia, pp. 11-13. https://doi.org/10.6084/m9.figshare.7211795

Lemenkova, P. 2016. Using GIS for Monitoring Lacustrine Ecosystem: a Case Study of Laguna de Gallocanta, Spain. In Conference Proceedings Problems of the Environmental Landscape Planning, pp. 237-240. https://doi.org/10.6084/m9.figshare.7210229

Lemenkova, P. 2019a. Automatic Data Processing for Visualising Yap and Palau Trenches by Generic Mapping Tools, Cartographic Letters, 27(2), pp. 72-89. https://doi.org/10.6084/m9.figshare.11544048

Lemenkova, P. 2019b. AWK and GNU Octave Programming Languages Integrated with Generic Mapping Tools for Geomorphological Analysis, GeoScience Engineering, 65(4), pp. 1-22. https://doi.org/10.35180/gse-2019-0020

Lemenkova, P. 2019c. Statistical Analysis of the Mariana Trench Geomorphology Using R Programming Language, Geodesy and Cartography, 45(2), pp. 57-84. https://doi.org/10.3846/gac.2019.3785

Lemenkova, P. 2019d. Processing oceanographic data by Python libraries NumPy, SciPy and Pandas, Aquatic Research, 2(2), pp. 73-91.

Lemenkova, P. 2020a. GMT Based Comparative Geomorphological Analysis of the Vityaz and Vanuatu Trenches, Fiji Basin. Geodetski List, 74(1), pp. 19-39. https://doi.org/10.6084/m9.figshare.12249773

Lemenkova, P. 2020b. Variations in the bathymetry and bottom morphology of the Izu-Bonin Trench modelled by GMT. Bulletin of Geography. Physical Geography Series, 18(1), pp. 41-60. https://doi.org/10.2478/bgeo-2020-0004

Lemenkova, P. 2020c. Hyperspectral Vegetation Indices Calculated by Qgis Using Landsat Tm Image: a Case Study of Northern Iceland. Advanced Research in Life Sciences, 4(1), pp. 70-78. https://doi.org/10.2478/arls-2020-0021

Lemenkova, P. 2020d. SAGA GIS for information extraction on presence and conditions of vegetation of northern coast of Iceland based on the Landsat TM. Acta Biologica Marisiensis 3(2), pp. 10-21. https://doi.org/10.2478/abmj-2020-0007

Lindh, P., Dahlin, T. & Svensson, M. 2000. Comparisons Between Different Test Methods for Soil Stabilisation, in: GeoEng 2000, pp. 1-7.

Lindh P. 2001. Optimising binder blends for shallow stabilisation of fine-grained soils. In Proceedings of the Institution of Civil Engineers Ground Improvement, 5, pp. 23-34.

Lindh, P. & Winter, M. G. 2003. Sample preparation effects on the compaction properties of Swedish fine-grained tills, Quarterly Journal of Engineering Geology and Hydrogeology, 36, pp. 321-330. https://doi.org/10.1144/1470-9236/03-018

Lindh P 2004. Compaction- and strength properties of stabilised and unstabilised fine-grained tills. PhD Thesis, Lund University, Lund. https://doi.org/10.13140/RG.2.1.1313.6481

Nagol, J. R., Sexton, J. O., Kim, D. H., Anand, A., Morton, D., Vermote, E. & Townshend, J. R. 2015. Bidirectional effects in Landsat reflectance estimates: Is there a problem to solve? ISPRS Journal of Photogrammetry and Remote Sensing, 103, pp. 129-135. https://doi.org/10.1016/j.isprsjprs.2014.09.006

Qiu, S., Lin, Y., Shang, R., Zhang, J., Ma, L., Zhu, Z., Qiu, S., Lin, Y., Shang, R., Zhang, J., Ma, L. & Zhu, Z. 2019. Making landsat time series consistent: evaluating and improving landsat analysis ready data, Remote Sensing, 11, pp. 51.

Robinson, Z. P., Fairchild, I. J. & Russell, A. J. 2008. Hydrogeological implications of glacial landscape evolution at Skeiðarársandur, SE Iceland, Geomorphology, 97, pp. 218-236. https://doi.org/10.1016/j.geomorph.2007.02.044

Russell, A. J., Roberts, M. J., Fay, H., Marren, P. M., Cassidy, N. J., Tweed, F. S. & Harris, T. 2006. Icelandic jökulhlaup impacts: implications for ice-sheet hydrology, sediment transfer and geomorphology, Geomorphology, 75, pp. 33-64. https://doi.org/10.1016/j.geomorph.2005.05.018

Schenke, H. W. & Lemenkova, P. 2008. Zur Frage der Meeresboden-Kartographie: Die Nutzung von AutoTrace Digitizer für die Vektorisierung der Bathymetrischen Daten in der Petschora-See, Hydrographische Nachrichten, 81, pp. 16-21. https://doi.org/10.6084/m9.figshare.7435538

Schowengerdt, R. 2007. Remote Sensing. Models and Methods for Image Processing, 3rd ed., Schowengerdt, R. Academic Press.

Steindórsson, S. 1962. On the age and immigration of the Icelandic flora, Societas Scientiarum Islandica, 35, pp. 5-155.

Suetova I. A., Ushakova L. A. & Lemenkova P. 2005a. Geoinformation mapping of the Barents and Pechora Seas. Geography and Natural Resources, 4, pp. 138-142. https://doi.org/10.6084/m9.figshare.7435535

Suetova I. A., Ushakova L. A. & Lemenkova P. 2005b. Geoecological Mapping of the Barents Sea Using GIS, International Cartographic Conference, La Coruna Spain. https://doi.org/10.6084/m9.figshare.7435529

Thórhallsdóttir, T. E. 1996. Seasonal and annual dynamics of frozen ground in the central highland of Iceland, Arctic, Antarctic, and Alpine Research, 28, pp. 237-243. https://doi.org/10.2307/1551765

Tomaszkiewicz, M., Abou Najm, M., Beysens, D., Alameddine, I. & El-Fadel, M. 2015. Dew as a sustainable non-conventional water resource: a critical review. Environmental Reviews, 23, pp. 425-442. https://doi.org/10.1139/er-2015-0035

Townshend, J. R., Masek, J. G., Huang, C., Vermote, E. F., Gao, F., Channan, S., Sexton, J. O., Feng, M., Narasimhan, R., Kim, D., Song, K., Song, D., Song, X. P., Noojipady, P., Tan, B., Hansen, M. C., Li, M. & Wolfe, R. E. 2012. Global characterization and monitoring of forest cover using Landsat data: opportunities and challenges, International Journal of Digital Earth, 5, pp. 373-397. https://doi.org/10.1080/17538947.2012.713190

Valjarević, A., Djekić, T., Stevanović, V., Ivanović, R. & Jandziković, B. 2018. GIS Numerical and remote sensing analyses of forest changes in the Toplica region for the period of 1953-2013. Applied Geographym 92, 131-139. https://doi.org/10.1016/j.apgeog.2018.01.016.

Valjarević A, Filipović D, Valjarević D, Milanović M, Milošević S., Živić, N. & Lukić, T. 2020. GIS and remote sensing techniques for the estimation of dew volume in the Republic of Serbia. Meteorological Applications 27(3), e1930. https://doi.org/10.1002/met.1930

Vermote, E., Justice, C., Claverie, M. & Franch, B. 2016. Preliminary analysis of the performance of the Landsat 8/OLI land surface reflectance product, Remote Sensing of Environment, 185, pp. 46-56. https://doi.org/10.1016/j.rse.2016.04.008

Vuollekoski, H., Vogt, M., Sinclair, V. A., Duplissy, J., Järvinen, H., Kyrö, E.-M., Makkonen, R., Petäjä, T., Prisle, N. L., Räisänen, P., Sipilä, M., Ylhäisi, J. & Kulmala, M. 2015. Estimates of global dew collection potential on artificial surfaces. Hydrology and Earth System Science, 19, pp. 601-613, https://doi.org/10.5194/hess-19-601-2015

Wan, N. 2015. Pesticides exposure modeling based on GIS and remote sensing land use data. Applied Geography, 56, pp. 99-106. https://doi.org/10.1016/j.apgeog.2014.11.012.

Wasowicz, P., Pasierbiński, A., Przedpelska-Wasowicz, E.M. & Kristinsson, H. 2014. Distribution Patterns in the Native Vascular Flora of Iceland. PLoS ONE, 9(7), pp. E102916. https://doi.org/10.1371/journal.pone.0102916

Wessel, P. & Smith, W. H. F. 1995. New version of the generic mapping tools released, Eos, Transactions American Geophysical Union, Washington, DC: American Geophysical Union, 76(33), 329. https://doi.org/10.1029/95EO00198

Woodcock, C. E., Allen, R., Anderson, M., Belward, A., Bindschadler, R., Cohen, W., Gao, F., Goward, S. N., Helder, D., Helmer, E., Nemani, R., Oreopoulos, L., Schott, J., Thenkabail, P. S., Vermote, E. F., Vogelmann, J., Wulder, M. A. & Wynne, R. 2008. Free access to Landsat imagery, Science, 320, pp. 1011.

Wulder, M. A., White, J. C., Loveland, T. R., Woodcock, C. E., Belward, A. S., Cohen, W. B., Fosnight, E. A., Shaw, J., Masek, J. G. & Roy, D. P. 2016. The global Landsat archive: Status, consolidation, and direction, Remote Sensing of Environment, 185, pp. 271-283. https://doi.org/10.1016/j.rse.2015.11.032

Wulder, M. A., Loveland, T. R., Roy, D. P., Crawford, C. J., Masek, J. G., Woodcock, C. E., Allen, R. G., Anderson, M. C., Belward, A. S., Cohen, W. B., Dwyer, J., Erb, A., Gao, F., Griffiths, P., Helder, D., Hermosilla, T., Hipple, J. D., Hostert, P., Hughes, M. J., Huntington, J., Johnson, D. M., Kennedy, R., Kilic, A., Li, Z., Lymburner, L., McCorkel, J., Pahlevan, N., Scambos, T. A., Schaaf, C., Schott, J. R., Sheng, Y., Storey, J., Vermote, E., Vogelmann, J., White, J. C., & Wynne, R. H. & Zhu, Z. 2019. Current status of Landsat program, science, and applications, Remote Sensing of Environment, 225, pp. 127-147. https://doi.org/10.1016/j.rse.2019.02.015

Zhong, Y. & Zhang, L. 2012. An Adaptive Artificial Immune Network for Supervised Classification of Multi-/Hyperspectral Remote Sensing Imagery. IEEE Transactions on Geoscience and Remote Sensing 50(3), pp. 894-909. https://doi.org/10.1109/TGRS.2011.2162589

Zhu, Z., Wulder, M. A., Roy, D. P., Woodcock, C. E., Hansen, M. C., Radeloff, V. C., Healey, S. P., Schaaf, C., Hostert, P., Strobl, P., Pekel, J. F., Lymburner, L., Pahlevan, N. & Scambos, T. A. 2019. Benefits of the free and open Landsat data policy, Remote Sensing of Environment, 224, pp. 382-385. https://doi.org/10.1016/j.rse.2019.02.016

Bulletin of Natural Sciences Research
Vol.11, No.1, 2021, pp. 38-43.

DOI: https://doi.org/10.5937/bnsr11-32015
Original Scientific Paper

CURVES ON RULED SURFACES UNDER INFINITESIMAL BENDING

MARIJA NAJDANOVIĆ[1,⋆], MIROSLAV MAKSIMOVIĆ[1], LJUBICA VELIMIROVIĆ[2]

[1]Faculty of Sciences and Mathematics, University of Priština in Kosovska Mitrovica, Serbia
[2]Faculty of Sciences and Mathematics, University of Niš, Niš, Serbia

ABSTRACT

Infinitesimal bending of curves lying with a given precision on ruled surfaces in 3-dimensional Euclidean space is studied. In particular, the bending of curves on the cylinder, the hyperbolic paraboloid and the helicoid are considered and appropriate bending fields are found. Some examples are graphically presented.

Keywords: Infinitesimal bending, Curve, Ruled surface, Cylinder, Hyperbolic paraboloid, Helicoid.

INTRODUCTION

Infinitesimal bending is a kind of deformations of geometric objects under which the arc length is stationary with appropriate precision which is described by the following equation

$$ds_\epsilon^2 - ds^2 = o(\epsilon),\ \epsilon > 0,\ \epsilon \to 0.$$

It means that the difference of the squares of the line elements of deformed and initial object is an infinitesimal of the order higher then the first with respect to the infinitesimal parameter ϵ. Many other geometric magnitudes stay invariant in the sense that they don't get the variations of the first order (for example, the coefficients of the first fundamental form, Cristoffel's symbols, Gaussian curvature etc.). Many papers are devoted to the infinitesimal bending of curves, surfaces and manifolds (see (Aleksandrov, 1936; Efimov, 1948; Kon-Fossen, 1959; Vekua, 1959; Ivanova-Karatopraklieva & Sabitov, 1995; Velimirović, 2001a,b; Hinterleitner et al., 2008; Rančić et al., 2009; Alexandrov, 2010; Najdanović, 2015; Najdanović & Velimirović, 2017; Kauffman et al., 2019; Najdanović et al., 2019; Rančić et al., 2019; Rýparová & Mikeš, 2019; Belova et al., 2021; Maksimović et al., 2021).

In (Najdanović & Velimirović, 2018) the authors studied the infinitesimal bending of curves that lie on ruled surfaces in Euclidean 3-dimensional space. It was proven that it is possible infinitesimally bend such a curve so that all bent curves remain on the same surface as the initial curve. Corresponding infinitesimal bending field under whose effect all bent curves remain on the same ruled surface was obtained.

The connection between ruled surfaces and infinitesimal bending of curves is also considered in (Gözütok et al., 2020). Some interesting papers on ruled surfaces are (Li & Pei, 2016; Li et al., 2021).

In this paper we observe a curve on a ruled surface and set the condition that all bent curves remain on the initial surface with a given precision. More precisely, let

$$C : \mathbf{r} = \mathbf{r}(t) = (x(t), y(t), z(t)),\ t \in J \subseteq \mathbb{R},$$

be the curve on the surface S given by the implicit equation

$$S : F(x, y, z) = 0.$$

So, it is valid

$$F(x(t), y(t), z(t)) = 0.$$

Suppose that

$$C_\epsilon : \mathbf{r}_\epsilon(t) = (x_\epsilon(t), y_\epsilon(t), z_\epsilon(t))$$

is an infinitesimal bending of the curve C and we get C for $\epsilon = 0$. The problem we pose is to determinate an infinitesimal bending of C so that all bent curves C_ϵ are on the surface S with a given precision, ie. so that the following condition is valid:

$$F(x_\epsilon(t), y_\epsilon(t), z_\epsilon(t)) = o(\epsilon). \tag{1}$$

Below we are going to consider infinitesimal bending of curves on a cylinder, on a hyperbolic paraboloid and on a helicoid. Some examples are graphically presented using program packet *Mathematica*.

INFINITESIMAL BENDING OF CURVES

At the beginning we are giving basic definitions and theorems regarding infinitesimal bending of curves according to (Efimov, 1948; Vekua, 1959; Velimirović, 2001a).

Let a regular curve C be given in the vector form

$$C : \mathbf{r} = \mathbf{r}(t), \quad t \in J \subseteq \mathbb{R} \tag{2}$$

included in the family of the curves

$$C_\epsilon : \mathbf{r}_\epsilon(t) = \mathbf{r}(t) + \epsilon \mathbf{z}(t),\ t \in J, \tag{3}$$

⋆ Corresponding author: marija.najdanovic@pr.ac.rs

where $\epsilon > 0$, $\epsilon \to 0$ is an infinitesimal parameter and we get C for $\epsilon = 0$ ($C = C_0$).

Definition 1. A family of curves C_ϵ given by (3) is called **infinitesimal deformation** of the curve C given by (2). The field $\mathbf{z} = \mathbf{z}(t)$, $\mathbf{z} \in C^1$, is **infinitesimal deformation field** of C.

Definition 2. An infinitesimal deformation C_ϵ given by (3) is called **infinitesimal bending** of the curve C given by (2) if

$$ds_\epsilon^2 - ds^2 = o(\epsilon),$$

where the field $\mathbf{z} = \mathbf{z}(t)$, $\mathbf{z} \in C^1$, is **infinitesimal bending field** of C.

Theorem 3. (Efimov, 1948) *Necessary and sufficient condition for* $\mathbf{z}(t)$ *to be an infinitesimal bending field of the curve C is to be*

$$d\mathbf{r} \cdot d\mathbf{z} = 0, \tag{4}$$

where $\cdot$ *stands for the scalar product in* $\mathbb{R}^3$. □

Definition 4. An infinitesimal bending field is **trivial** if it can be given in the form

$$\mathbf{z} = \mathbf{a} \times \mathbf{r} + \mathbf{b},$$

where $\mathbf{a}$ and $\mathbf{b}$ are constant vectors.

According to Vekua (1959) we have the next theorem.

Theorem 5. *Under infinitesimal bending of curves each line element undertakes a nonnegative addition, which is the infinitesimal value of at least the second order with respect to* ϵ*, i. e.*

$$ds_\epsilon - ds = o(\epsilon) \geq 0.$$

□

Infinitesimal bending field of a curve C is determined in the following theorem.

Theorem 6. (Velimirović, 2001a) *Infinitesimal bending field for the curve C given by (2) is*

$$\mathbf{z}(t) = \int [p(t)\mathbf{n}_1(t) + q(t)\mathbf{n}_2(t)]\, dt, \tag{5}$$

where $p(t)$ *and* $q(t)$ *are arbitrary integrable functions and vectors* $\mathbf{n}_1(t)$ *and* $\mathbf{n}_2(t)$ *are respectively unit principal normal and binormal vector fields of the curve C.* □

INFINITESIMAL BENDING OF CURVES ON CYLINDER

Let be given a cylinder by the implicit equation

$$S : F(x, y, z) \equiv x^2 + y^2 - a^2 = 0, \tag{6}$$

$a > 0$, or by the vector parametric equation

$$S : \mathbf{r}(u, v) = (a\cos u, a\sin u, v),\ u \in [0, 2\pi],\ v \in [0, h]. \tag{7}$$

Let

$$C : \mathbf{r}(t) = \mathbf{r}(u(t), v(t)) = (a\cos u(t), a\sin u(t), v(t)),\ t \in J, \tag{8}$$

be the curve on the cylinder S. Suppose that

$$C_\epsilon : \mathbf{r}_\epsilon(t) = (a\cos u(t) + \epsilon z_1(t), a\sin u(t) + \epsilon z_2(t), v(t) + \epsilon z_3(t)) \tag{9}$$

is an infinitesimal bending of C, where $z_1(t)$, $z_2(t)$, $z_3(t)$ are real continuous differentiable functions. In order to stay on the cylinder S with a given precision, it is necessary to apply the condition (1), so we have

$$(a\cos u(t) + \epsilon z_1(t))^2 + (a\sin u(t) + \epsilon z_2(t))^2 - a^2 = o(\epsilon).$$

From the last equation we obtain the condition

$$\cos u(t) z_1(t) + \sin u(t) z_2(t) = 0 \tag{10}$$

which allows the bent curves to stay on the cylinder S with a given precision. For $\cos u(t) \neq 0$ we can express z_1 as a function of z_2:

$$z_1(t) = -\tan u(t) z_2(t). \tag{11}$$

Therefore, we are looking for the infinitesimal bending field in the following form

$$\mathbf{z}(t) = (-\tan u(t) z_2(t), z_2(t), z_3(t)). \tag{12}$$

In order for the field (12) to be an infinitesimal bending field, it is necessary that the condition $\dot{\mathbf{r}} \cdot \dot{\mathbf{z}} = 0$ is valid. Since $\dot{\mathbf{r}}(t) = (-a\sin u(t)\,\dot{u}(t), a\cos u(t)\,\dot{u}(t), \dot{v}(t))$ and $\dot{\mathbf{z}}(t) = (-\frac{\dot{u}(t)}{\cos^2 u(t)} z_2(t) - \tan u(t)\,\dot{z}_2(t), \dot{z}_2(t), \dot{z}_3(t))$, we obtain

$$a\,\dot{u}(t)^2 \frac{\sin u(t)}{\cos^2 u(t)} z_2(t) + \frac{a\,\dot{u}(t)}{\cos u(t)} \dot{z}_2(t) + \dot{v}(t)\dot{z}_3(t) = 0. \tag{13}$$

This is the relationship between z_2 and z_3. Let us choose arbitrarily z_3 and solve the linear differential equation by z_2. The solution is

$$z_2(t) = e^{-\int \dot{u}(t)\tan u(t)\,dt} \left[c - \frac{1}{a} \int \frac{\dot{v}(t)\cos u(t)}{\dot{u}(t)} \dot{z}_3(t) e^{\int \dot{u}(t)\tan u(t)\,dt} dt \right], \tag{14}$$

$u(t) \neq const$, $\cos u(t) \neq 0$ and c is a constant. If $\dot{v}(t) = 0 \Rightarrow v(t) = const$, the curve C is a circle on the cylinder. In that case we choose z_3 arbitrarily and determine z_2 from

$$z_2(t) = ce^{-\int \dot{u}(t)\tan u(t)\,dt}.$$

If $u(t) = const$, then the equation (13) reduces to $\dot{v}(t)\dot{z}_3(t) = 0$ wherefrom we have $\dot{z}_3(t) = 0 \Rightarrow z_3(t) = const$ and we choose z_2 arbitrarily.

Based on the previous considerations, the following theorems hold.

Theorem 7. *The field* $\mathbf{z}(t) = (z_1(t), z_2(t), z_3(t))$ *whose components* z_1 *and* z_2 *satisfy the condition (10) includes the curve (8) under infinitesimal deformation into the family of deformed curves on the cylinder (6) with a given precision.* □

Theorem 8. *The field* $\mathbf{z}(t)$ *given by (12) where* $z_3(t)$ *is arbitrary real continuous differentiable function, and* $z_2(t)$ *is given in (14), is infinitesimal bending field of the curve (8) so that all bent curves are on the cylinder (6) with a given precision.* □

Example 9. Let be $u(t) = t$, $v(t) = 0$. Then the curve C is a circle $\mathbf{r}(t) = (a\cos t, a\sin t, 0)$. We have

$$z_2(t) = ce^{-\int \tan t\, dt} = \bar{c}\cos t,$$

$$z_1(t) = -c\tan t\cos t = -\bar{c}\sin t,$$

z_3-arbitrarily, c, $\bar{c}$ are constants. So, the infinitesimal bending field is $\mathbf{z}(t) = (-\bar{c}\sin t, \bar{c}\cos t, z_3(t))$. By a simple check, we conclude that the conditions $\dot{\mathbf{r}}\cdot\dot{\mathbf{z}} = 0$ and $(a\cos t - \epsilon\bar{c}\sin t)^2 + (a\sin t + \epsilon\bar{c}\cos t)^2 - a^2 = \epsilon^2\bar{c}^2 = o(\epsilon)$ are satisfied. An illustration of the infinitesimal bending is shown in Figures 1 and 2.

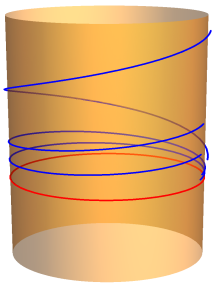

Figure 1. Circle (red) on the cylinder and infinitesimally bent curves (blue), for $\bar{c} = 1$, $z_3(t) = t + 1$ and $\epsilon = 0.05, 0.1, 0.25$.

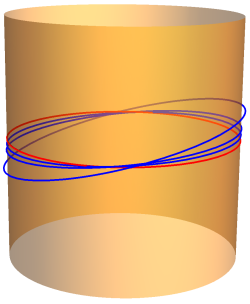

Figure 2. Circle (red) on the cylinder and infinitesimally bent curves (blue), for $\bar{c} = 1$, $z_3(t) = \cos t$ and $\epsilon = 0.05, 0.1, 0.25$.

INFINITESIMAL BENDING OF CURVES ON HYPERBOLIC PARABOLOID

Let the curve $C : \mathbf{r} = \mathbf{r}(t)$ lie on the hyperbolic paraboloid

$$S : F(x, y, z) \equiv xy - z = 0 \tag{15}$$

with the vector parametric equation

$$S : \mathbf{r}(u, v) = (u, v, uv).$$

Of course, the following equation holds

$$C : \mathbf{r} = \mathbf{r}(t) = \mathbf{r}(u(t), v(t)) = (u(t), v(t), u(t)v(t)). \tag{16}$$

Let $\mathbf{z}(t) = (z_1(t), z_2(t), z_3(t))$ be an infinitesimal bending field under which all bent curves are on the surface (15) with a given precision. As the infinitesimal bending is in the following form

$$\mathbf{r}_\epsilon(t) = \mathbf{r}(t) + \epsilon\mathbf{z}(t) \equiv (x_\epsilon(t), y_\epsilon(t), z_\epsilon(t)),$$

the condition (1) reduces to

$$(u(t) + \epsilon z_1(t))(v(t) + \epsilon z_2(t)) - u(t)v(t) - \epsilon z_3(t) = o(\epsilon)$$

ie.

$$z_1(t)v(t) + z_2(t)u(t) - z_3(t) = 0. \tag{17}$$

This is the necessary and sufficient condition which allows that all bent curves are approximately on S. From Eq. (17) we obtain

$$z_3(t) = z_1(t)v(t) + z_2(t)u(t). \tag{18}$$

Therefore,

$$\mathbf{z}(t) = (z_1(t), z_2(t), z_1(t)v(t) + z_2(t)u(t)) \tag{19}$$

is the required field. It is also necessary to apply the condition $\dot{\mathbf{r}}\cdot\dot{\mathbf{z}} = 0$. Since $\dot{\mathbf{r}} = (\dot{u}, \dot{v}, \dot{u}v + u\dot{v})$, and $\dot{\mathbf{z}} = (\dot{z}_1, \dot{z}_2, \dot{z}_1 v + z_1\dot{v} + \dot{z}_2 u + z_2\dot{u}$, we obtain

$$[\dot{v} + (uv)^{\cdot}u]\dot{z}_2 + (uv)^{\cdot}\dot{u}z_2 + \varphi = 0, \tag{20}$$

where

$$\varphi = [\dot{u} + (uv)^{\cdot}v]\dot{z}_1 + (uv)^{\cdot}\dot{v}z_1.$$

If we arbitrarily choose z_1, we obtain the function z_2 by solving the linear differential equation (20), and z_3 from Eq. (18). The equation (20) reduces to

$$\dot{z}_2 + \frac{(uv)^{\cdot}\dot{u}}{\dot{v} + (uv)^{\cdot}u}z_2 = -\frac{\varphi}{\dot{v} + (uv)^{\cdot}u},\ \dot{v} + (uv)^{\cdot}u \neq 0$$

whose solution is

$$z_2 = e^{-\int \frac{(uv)^{\cdot}\dot{u}}{\dot{v}+(uv)^{\cdot}u}dt}\left[c - \int \frac{\varphi}{\dot{v} + (uv)^{\cdot}u}e^{\int \frac{(uv)^{\cdot}\dot{u}}{\dot{v}+(uv)^{\cdot}u}dt}dt\right], \tag{21}$$

c is a constant.

In this way we have proved the following theorems.

Theorem 10. *The field* $\mathbf{z}(t) = (z_1(t), z_2(t), z_3(t))$ *whose components* z_1, z_2 *and* z_3 *satisfy the condition (17) includes the curve (16) under infinitesimal deformation into the family of deformed curves on the hyperbolic paraboloid (15) with a given precision.* □

Theorem 11. *The field* $\mathbf{z}(t)$ *given by (19) where* $z_1(t)$ *is arbitrary real continuous differentiable function, and* $z_2(t)$ *is given in (21), is infinitesimal bending field of the curve (16) so that all bent curves are on the hyperbolic paraboloid (15) with a given precision.* □

Example 12. Let the curve $C : \mathbf{r}(t) = (t, t, t^2)$, $t \in J \subseteq \mathbb{R}$, be given on the hyperbolic paraboloid $S : \mathbf{r}(u, v) = (u, v, uv)$. Let us find the field $\mathbf{z}$ according to the previous theorem.

Let be $z_1(t) = t$. Since $u(t) = t$, $v(t) = t$, $\dot{u} = 1$, $\dot{v} = 1$, $\dot{z}_1 = 1$, we obtain $\varphi = 1 + 4t^2$. Also,

$$z_2 = e^{-\int \frac{2t}{1+2t^2}dt}\left[c - \int \frac{1+4t^2}{1+2t^2} e^{\int \frac{2t}{1+2t^2}dt} dt\right] = \frac{c}{\sqrt{1+2t^2}} - t.$$

Next, we have

$$z_3 = z_1 v + z_2 u = \frac{ct}{\sqrt{1+2t^2}}.$$

Therefore, the corresponding infinitesimal bending field is

$$\mathbf{z}(t) = \left(t, \frac{c}{\sqrt{1+2t^2}} - t, \frac{ct}{\sqrt{1+2t^2}}\right), \tag{22}$$

so

$$\mathbf{r}_\epsilon = \left(t + \epsilon t, t + \epsilon\left(\frac{c}{\sqrt{1+2t^2}} - t\right), t^2 + \epsilon\frac{ct}{\sqrt{1+2t^2}}\right).$$

It is easy to check that the following is true: $\dot{\mathbf{r}} = (1, 1, 2t)$, $\dot{\mathbf{z}} = \left(1, \frac{-2ct}{\sqrt{(1+2t^2)^3}} - 1, \frac{c}{\sqrt{(1+2t^2)^3}}\right)$, $\dot{\mathbf{r}} \cdot \dot{\mathbf{z}} = 0$,

$$(t + \epsilon t)\left(t + \epsilon\left(\frac{c}{\sqrt{1+2t^2}} - t\right)\right) - t^2 - \epsilon\frac{ct}{\sqrt{1+2t^2}} = \epsilon^2 t\left(\frac{c}{\sqrt{1+2t^2}} - t\right) = o(\epsilon).$$

Figure 3 shows infinitesimal bending of curve C under field (22).

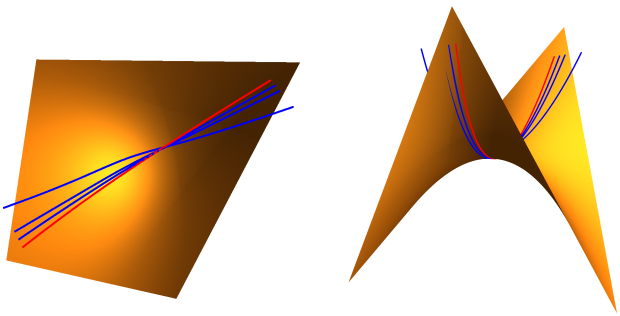

Figure 3. Curve C (red) on the hyperbolic paraboloid and infinitesimally bent curves (blue), for $c = 1$ and $\epsilon = 0.05, 0.1, 0.25$.

INFINITESIMAL BENDING OF CURVES ON HELICOID

Let $C : \mathbf{r} = \mathbf{r}(t)$ be the curve on the helicoid

$$S : F(x, y, z) \equiv \frac{y}{x} - \tan\frac{z}{c} = 0, \tag{23}$$

c-constant, with the vector parametric equation

$$\mathbf{r}(u, v) = (u\cos v, u\sin v, cv).$$

Then the equation of the curve C has the form

$$C : \mathbf{r}(t) = \mathbf{r}(u(t), v(t)) = (u(t)\cos v(t), u(t)\sin v(t), cv(t)). \tag{24}$$

Let $\mathbf{z}(t) = (z_1(t), z_2(t), z_3(t))$ be an infinitesimal bending field which given curve leaves on the helicoid S, where $z_1(t)$, $z_2(t)$, $z_3(t)$ are real continuous differentiable functions. Then will be

$$\mathbf{r}_\epsilon(t) = (u(t)\cos v(t) + \epsilon z_1(t), u(t)\sin v(t) + \epsilon z_2(t), cv(t) + \epsilon z_3(t))$$

the corresponding infinitesimal bending and the condition

$$\frac{u(t)\sin v(t) + \epsilon z_2(t)}{u(t)\cos v(t) + \epsilon z_1(t)} - \tan\frac{cv(t) + \epsilon z_3(t)}{c} = o(\epsilon)$$

must be satisfied. From the last equation we have

$$\frac{u(t)\sin v(t) + \epsilon z_2(t)}{u(t)\cos v(t) + \epsilon z_1(t)} - \frac{\tan v(t) + \tan(\epsilon\frac{z_3(t)}{c})}{1 - \tan v(t)\tan(\epsilon\frac{z_3(t)}{c})} = o(\epsilon),$$

or, after using Maclaurin series for $y = \tan x$:

$$\frac{u(t)\sin v(t) + \epsilon z_2(t)}{u(t)\cos v(t) + \epsilon z_1(t)} - \frac{\tan v(t) + \epsilon\frac{z_3(t)}{c} + o(\epsilon^2)}{1 - \tan v(t)(\epsilon\frac{z_3(t)}{c} + o(\epsilon^2))} = o(\epsilon).$$

From here we obtain

$$z_2(t) - u(t)\frac{\sin^2 v(t)}{\cos v(t)}\frac{z_3(t)}{c} - z_1(t)\tan v(t) - u(t)\cos v(t)\frac{z_3(t)}{c} = 0,$$

ie.

$$z_2(t) = z_1(t)\tan v(t) + \frac{z_3(t)u(t)}{c\cos v(t)}. \tag{25}$$

Thus the field $\mathbf{z}(t)$ has the following form

$$\mathbf{z}(t) = \left(z_1(t), z_1(t)\tan v(t) + \frac{z_3(t)u(t)}{c\cos v(t)}, z_3(t)\right), \tag{26}$$

$\cos v(t) \neq 0$, and the functions $z_1(t)$ and $z_2(t)$ are obtained from the condition

$$\dot{\mathbf{r}} \cdot \dot{\mathbf{z}} = 0,$$

where

$$\dot{\mathbf{r}} = (\dot{u}(t)\cos v(t) - u(t)\dot{v}(t)\sin v(t), \dot{u}(t)\sin v(t) + u(t)\dot{v}(t)\cos v(t), c\dot{v}(t))),$$

$$\dot{\mathbf{z}} = \left(\dot{z}_1(t), \dot{z}_1(t)\tan v(t) + \frac{z_1(t)\dot{v}(t)}{\cos^2 v(t)} + \frac{(\dot{z}_3(t)u(t) + z_3(t)\dot{u}(t))\cos v(t) + z_3(t)u(t)\dot{v}(t)\sin v(t)}{c\cos^2 v(t)}, \dot{z}_3(t)\right).$$

For simplicity, let us consider a helix which is obtained for $u = 1$ and $v = t$. Therefore, the vector parametric equation of a helix is

$$\mathbf{r}(t) = (\cos t, \sin t, ct). \tag{27}$$

The field $\mathbf{z}$ reduces to

$$\mathbf{z} = \left(z_1(t), z_1(t)\tan t + \frac{z_3(t)}{c\cos t}, z_3(t)\right), \tag{28}$$

$\cos t \neq 0$. Since $\dot{\mathbf{r}} = (-\sin t, \cos t, c)$, $\dot{\mathbf{z}} = (\dot{z}_1(t), \dot{z}_1(t)\tan t + \frac{z_1(t)}{\cos^2 t} + \frac{\dot{z}_3(t)\cos t + z_3(t)\sin t}{c\cos^2 t}, \dot{z}_3(t))$, using the condition $\dot{\mathbf{r}}\cdot\dot{\mathbf{z}} = 0$ we get the equation

$$\dot{z}_3 + \frac{1}{1+c^2}z_3(t)\tan t = -\frac{c}{1+c^2}\frac{z_1(t)}{\cos t}. \tag{29}$$

This is the relationship between z_1 and z_3. We choose one of these functions arbitrarily, and we get the other by solving the equation (29). Thus, if z_1 is arbitrary real continuous differentiable function, we obtain

$$z_3(t) = (\cos t)^{\frac{1}{1+c^2}}\left[c_1 - \frac{c}{1+c^2}\int \frac{z_1(t)}{(\cos t)^{\frac{2+c^2}{1+c^2}}}dt\right], \tag{30}$$

where c_1 is a constant.

Theorem 13. *The field* $\mathbf{z}(t) = (z_1(t), z_2(t), z_3(t))$ *whose components* z_1, z_2 *and* z_3 *satisfy the condition (25) includes the curve (24) under infinitesimal deformation into the family of deformed curves on the helicoid (23) with a given precision.* □

Theorem 14. *The field* $\mathbf{z}(t)$ *given by (28) where* $z_1(t)$ *is arbitrary real continuous differentiable function, and* $z_3(t)$ *is given in (30), is infinitesimal bending field of the helix (27) so that all bent curves are on the helicoid (23) with a given precision.* □

Example 15. Let be $z_1(t) = (1 + 2c^2)\sin t\cos^2 t$. Then we obtain after necessary integration (for $c_1 = 0$) $z_3(t) = c\cos^2 t$, and $z_2(t) = (1 + 2c^2)\sin^2 t\cos t + \cos t$.

The corresponding infinitesimal bending field which given helix leaves at the helicoid with a given precision is

$$\mathbf{z}(t) = ((1 + 2c^2)\sin t\cos^2 t, (1 + 2c^2)\sin^2 t\cos t + \cos t, c\cos^2 t). \tag{31}$$

By a simple check, we conclude that this is an infinitesimal bending field and the condition (1) is valid.

Infinitesimal bending of a helix on the helicoid under bending field (31) is shown in Figure 4.

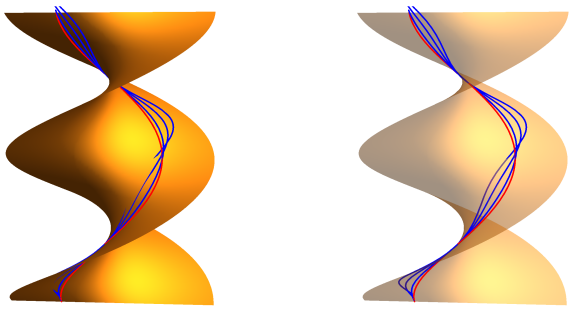

Figure 4. Helix (red) on the helicoid and infinitesimally bent curves (blue), for $\epsilon = 0.05, 0.15, 0.25$.

CONCLUSION

In this paper, infinitesimal bending of curves that are approximately on the cylinder, the hyperbolic paraboloid and the helicoid, respectively, are examined. The corresponding infinitesimal bending fields are obtained and some examples with graphical illustration are considered. This is a continuation of the research published in the paper (Najdanović & Velimirović, 2018).

ACKNOWLEDGEMENT

This work is supported by the Serbian Ministry of Education, Science and Technological Development under the research grant 451-03-68/2020-14/200123 (the first and the second author) and 451-03-68/2020-14/200124 (the third author).

REFERENCES

Aleksandrov, A. D. 1936, O beskonechno malyh izgibaniyah neregulyarnyh poverhnostei, Matem. sbornik, 1(43), pp. 307-321.

Alexandrov, V. 2010, New manifestations of the Darboux's rotation and translation fields of a surface, New Zealand Journal of Mathematics, 40, pp. 59-65.

Belova, O., Mikeš, J., & Sherkuziyev, M. 2021, An Analytical Inflexibility of Surfaces Attached Along a Curve to a Surface Regarding a Point and Plane, Results Math, 76(56). doi:10.1007/s00025-021-01362-0

Efimov, N. 1948, Kachestvennye voprosy teorii deformacii poverhnostei, UMN. 3. 2, pp. 47-158.

Gözütok, U., Çoban, H. A., & Sağiroğlu, Y. 2020, Ruled surfaces obtained by bending of curves, Turk J Math, 44, pp. 300-306. doi:10.3906/mat-1908-21

Hinterleitner, I., Mikeš, J., & Stránská, J. 2008, Infinitesimal Fplanar transformations, Russian Mathematics, 52(4), pp. 13-18. doi:10.3103/s1066369x08040026

Ivanova-Karatopraklieva, I. & Sabitov, I. K. 1995, Bending of surfaces. Part II, Journal of Mathematical Sciences, 74(3), pp. 997-1043. doi:10.1007/bf02362831

Kauffman, L. H., Velimirović, Lj. S., Najdanović, M. S., & Rančić, S. R. 2019, Infinitesimal bending of knots and energy change.,

Journal of Knot Theory and Its Ramifications, 28(11), 1940009. doi:10.1142/S0218216519400091

Kon-Fossen, S. E. 1959, Nekotorye voprosy differ. geometrii v celom (Moskva: Fizmatgiz)

Li, Y. & Pei, D. 2016, Evolutes of dual spherical curves for ruled surfaces, Mathematical Methods in the Applied Sciences 39(11), pp. 3005-3015. doi:10.1002/mma.3748

Li, Y., Wang, Z., & Zhao, T. 2021, Geometric Algebra of Singular Ruled Surfaces, Advances in Applied Clifford Algebras, 31(2), pp. 1-19. doi:10.1007/s00006-020-01097-1

Maksimović, M., Velimirović, Lj., & Najdanović, M. 2021, Infinitesimal bending of DNA helices, Turk J Math, 45, pp. 520-528. doi:10.3906/mat-2003-106

Najdanović, M. 2015, Infinitesimal bending influence on the Willmore energy of curves, Filomat, 29(10), pp. 2411–2419. doi:10.2298/fil1510411n

Najdanović, M. S., Rančić, S. R., Kauffman, L. H., & Velimirović, Lj. S. 2019, The total curvature of knots under second-order infinitesimal bending, Journal of Knot Theory and Its Ramifications, 28(1), 1950005. doi:10.1142/S0218216519500056

Najdanović, M. S. & Velimirović, Lj. S. 2017, On the Willmore energy of curves under second order infinitesimal bending, Miskolc Mathematical Notes, 17(2), pp. 979-987. doi:10.18514/mmn.2017.2133

Najdanović, M. S. & Velimirović, Lj. S. 2018, Infinitesimal bending of curves on the ruled surfaces, University thought - Publication in Natural Sciences, 8(1), pp. 46-51. doi:10.5937/univtho8-17403

Rančić, S., Najdanović, M., & Velimirović, Lj. 2019, Total normalcy of knots, Filomat, 33(4), pp. 1259-1266. doi:10.2298/FIL1904259R

Rančić, S., Velimirović, Lj., & Zlatanović, M. 2009, Curvebend graphical tool for presentation of infinitesimal bending of curves, Filomat, 23(2), pp. 108-116. doi:10.2298/fil0902108r

Rýparová, L. & Mikeš, J. 2019, Infinitesimal Rotary Transformation, Filomat, 33(4), pp. 1153-1157. doi.org/10.2298/FIL1904153R

Vekua, I. 1959, Obobschennye analiticheskie funkcii (Moskva)

Velimirović, Lj. 2001a, Change of geometric magnitudes under infinitesimal bending, Facta universitatis - series: Mechanics, Automatic Control and Robotics, 3(11), pp. 135-148.

Velimirović, Lj. 2001b, Infinitesimal bending of curves, Matematicki bilten Skopje, Makedonija, 25(LI), pp. 25-36.

Bulletin of Natural Sciences Research
Vol.11, No.1, 2021, pp. 44-48.

DOI: https://doi.org/10.5937/bnsr11-28704
Original Scientific Paper

ON THE STARK BROADENING OF Ru III SPECTRAL LINES

MILAN S. DIMITRIJEVIĆ[1,2,⋆]

[1]Astronomical Observatory, Volgina 7, 11060 Belgrade, Serbia
[2]Sorbonne Université, Observatoire de Paris, Université PSL, CNRS, LERMA, F-92190, Meudon, France

ABSTRACT

Stark broadening parameters, full widths at half maximum (FWHM) and shifts for spectral lines within six multiplets of doubly charged ruthenium ions have been calculated, for an electron density of 10^{17} cm^{-3} and temperature range from 10 000 K to 160 000 K. Calculations have been performed with the simplified modified semiempirical (SMSE) approach. In the case of two multiplets, it is possible to apply the full modified semiempirical method. The corresponding calculations have been performed and results are compared in order to test and determine the accuracy of the SMSE approach. The results are also used for the consideration of Stark width and shift regularities in Ru III spectrum.

Keywords: Stark broadening, Spectral lines, Line profiles, Ru III.

INTRODUCTION

Spectral line profiles in spectra emitted from various plasmas are very useful and precious source of informations about plasma conditions, like electron density, temperature and chemical composition. Among different line broadening mechanisms, Stark broadening due to interaction of emitter/absorber with surrounding charged particles has many useful applications in astrophysics (see e.g. Dimitrijević (2017)), as well as for laboratory plasmas investigation and especially diagnostics. Stark broadening data are also useful for different investigations and modelling of fusion plasma, laser produced plasma diagnostic and analysis, as well as for its different applications in industry and technology as for example for welding, melting and piercing of metals by laser produced plasmas (see for example Dimitrijević (2017) and references therein). Such data are also needed for design and development of light sources using different plasmas (Dimitrijević & Sahal-Bréchot, 2014), as well as for development of laser devices.

One of trace elements, which importance for stellar physics increases with the development of spectroscopic possibilities to obtain high resolution spectra using instruments on board of satellites and on large terrestrial telescopes is ruthenium, a transition metal belonging to the platinum group of the periodic table. In industry and technology, ruthenium is used for wear-resistant electrical contacts and thick-film resistors, as well as in platinum alloys and as a chemistry catalyst.

It is created in stellar interiors in r-process (rapid neutron capture) and it is present in stellar plasma. Yet Merril (1947) found ruthenium lines in the spectrum of R Andromedae. Adelman et al. (1979) found that Ru I spectral lines are possibly present in gama Equulei (HD 201601), an Ap star where Stark broadening might be of interest. Biémont et al. (1984) determined that solar abundance of ruthenium is 1.84. With the development of space astronomy and large telescopes of new generation, number of stars where ruthenium is found increased. So Allen & Porto de Mello (2007) determined Ruthenium abundances in a large sample of giant and dwarf barium stars, within a wide range of plasma parameters. The effective temperatures were 4300 K $< T_{eff} <$ 6500 K and logarithm of surface gravity $1.4 \leq \log g < 4.6$. We note that for largest surface gravities and effective temperatures in this sample Stark broadening might be of interest. Roederer et al. (2010) found Ru I lines in the optical spectrum of r-process enriched metal-poor star BD +17 3248, obtained with the High Resolution Echelle Spectrograph on Keck telescope. Hansen et al. (2014) performed a large consistent study of ruthenium abundances in our Galaxy, using a sample of 52 stars with Ru I lines in their spectra. They underlined that ruthenium is important for nucleosynthetic diagnostics. Mishenina et al. (2019) found Ru I spectral lines and determined ruthenium abundance for a sample of 162 F-, G-, and K-stars belonging to different substructures of the Milky Way.

We can see that ruthenium is widely present in stellar plasma and the corresponding Stark broadening data are needed for determination of abundances, radiative transfer calculations, stellar opacity calculations, modelling of stellar atmospheres and stellar spectra analysis and synthesis. Such data are particularly needed for white dwarfs, where the condition for Stark broadening are very favorable so that it is the principal pressure broadening mechanism (Beauchamp et al., 1997; Tankosić et al., 2003; Milovanović et al., 2004; Simić et al., 2006). Stark broadening is often non negligible and in the case of A type and late B type stars (see for example Simić et al. (2005b,a, 2009)).

In spite of its wide presence in stellar plasma, the corresponding atomic data, needed for various problems in astrophysics and physics are scarce and neither experimental nor theoretical data on Stark broadening exist in literature. In order to provide some of the needed data we calculated here Stark full widths at half maximum (FWHM - W) and shifts the for six multiplets in

⋆ Corresponding author: mdimitrijevic@aob.rs

the spectrum of doubly charged ruthenium ion by using the simplified modified semiempirical method - SMSE (Dimitrijević & Konjević, 1987). Additionally, for two multiplets, for which is possible to apply the full modified semiempirical method - MSE (Dimitrijević & Konjević, 1980; Dimitrijević & Kršljanin, 1986; Dimitrijević & Popović, 2001), analyzed in Dimitrijević (2017). The results obtained using both methods are compared in order to test the accuracy of SMSE method. The obtained results are also used for discussion of regularities of Stark broadening parameters. The obtained results for Ru III will be included in the STARK-B (Sahal-Bréchot et al., 2015; Sahal-Bréchot et al., 2020) database.

NOTES ON CALCULATIONS

Ru III has atomic number 44 and belongs to the isoelectronic sequence of molybdenum. Atomic energy levels needed for the corresponding calculations have been taken from Kramida et al. (2020) and Moore (1971). The existing data for atomic energy levels are scarce and not complete. Consequently, it is not possible to use in appropriate way the more accurate semiclassical perturbation method (Sahal-Bréchot, 1969a,b; Sahal-Bréchot et al., 2014).

The modified semiempirical method (MSE) (Dimitrijević & Konjević, 1980; Dimitrijević & Kršljanin, 1986; Dimitrijević & Popović, 2001) is applicable only for two multiplets, for which we performed calculations of full width at half intensity maximum (FWHM) W. Since this method is presented recently in Dimitrijević (2017), we will not repeat this here.

For other four multiplets the simplified modified semiempirical (SMSE) method (Dimitrijević & Konjević, 1987) is the most advanced method that is applicable in an adequate way, without *ab initio* calculations when one first calculates the needed atomic energy levels. This method is applied to all six Ru III multiplets considered here. It is well described recently (Dimitrijević, 2020), so there is no need to describe it again.

For the case of the six Ru III multiplets we checked the validity condition of SMSE method (see e.g. Dimitrijević (2020)):

$$x_{jj'} = E/|E_{j'} - E_j| \leq 2 \tag{1}$$

Here, $E = 3kT/2$, is energy of free electron, j=i,f, where i is for initial atomic energy level of the considered spectral line and f for final, $E_{j'}$ (j′=i′ or f′) is the nearest atomic energy level for which exists possibility of an allowed dipole transition from or to the energy level i or f. So X is ratio of energy of free electron and of energy difference between initial or final level and the nearest perturbing level. As the validity condition we take the higher x value of values for initial and final levels.

We can calculate one value for the whole multiplet if the so called "one electron approximation" (Griem, 1974) is valid,namely if the energy distance between atomic energy levels in particular terms making the considered multiplet is much lower than the closest energy distance between two considered terms. In such a case we calculate an average energy of the term using the expression:

$$E = \frac{\sum_J (2J+1)E_J}{\sum_J (2J+1)}, \tag{2}$$

where E is the averaged energy and E_J and J energy and total angular momentum of a particular energy level.

If we want to obtain Stark broadening parameter, width or shift, for a particular spectral line within the considered multiplet, for the width, for example, we can use the expression:

$$W_{line} = (\lambda^2_{line}/\lambda^2_{mult})W_{mult} \tag{3}$$

where W_{line} and λ_{line} are width and wavelength of a particular line within multiplet, while W_{mult} and λ_{mult} are the corresponding values for the multiplet. The equation for the shift is analogous.

RESULTS AND DISCUSSION

With the help of SMSE approach (Dimitrijević & Konjević, 1987) we calculated Full Stark widths at half intensity maximum (W) and shifts (d) for six multiplets of doubly charged ruthenium (Ru III) with spectral lines broadened due to collisions with electrons, for an electron density of 10^{17} cm^{-3} and plasma temperatures of 10 000, 20 000, 40 000, 80 000 and 160 000 K. Additionally, for multiplets $5s^7S$-$5p^7P^o$ and $5s^5S$-$5p^5P^o$ we calculated Stark widths using more sophisticated MSE method (Dimitrijević & Konjević, 1980), since only for those two multiplets application of this method is adequate.

The obtained results for Stark widths (W) and shifts (d) are presented in Table 1. We note that for high densities linear dependence of Stark widths and shifts in function of density of electrons, may be influenced by Debye screening. In the last column the validity condition of the SMSE method, given by Eq. (1) is presented. We can see that for T = 160 000 K validity condition for SMSE method is not satisfied. These values are given for better interpolation for temperatures larger than 80 000 K.

If we compare the SMSE width with more sophisticated MSE calculations, we can see that in the case of $5s^7S$-$5p^7P^o$ multiplet at the temperature of 10 000 K, SMSE width is 14% larger than MSE width and for 160 000 this difference is only 5.3%. In the case of $5s^5S$-$5p^5P^o$ multiplet, these values are 13.5% and 1.6% respectively. First of all this confirms that more approximate SMSE results are acceptable. An interesting result is that for temperature of 160 000 K, where validity condition is not satisfied the obtained results are even in better mutual agreement which implies that all results for T = 160 000 K in Table 1 are acceptable.

Besides Stark broadening parameters in Å units, which is common presentation, in Table 1 they are given and in angular frequency units (s−1). This is more suitable for discussion of regularities because in such a way the influence of wavelength is avoided. The relation between Stark widths in Å units and in s−1 units is:

Table 1. This table gives electron-impact broadening (Stark broadening) Full Widths at Half Intensity Maximum (W) and shifts (d) for Ru III spectral lines, for a perturber density of 10^{17} cm^{-3} and temperatures from 10 000 to 160 000 K. Also, the $3kT/2\Delta E$, quantity is given, where ΔE is the energy difference between closest perturbing level and the closer of initial and final levels. In order that the used method is valid, this quantity should be less or equal two.

Transition	T(K)	W[Å]	d[Å]	W[10^{12} s^{-1}]	d[10^{12} s^{-1}]	W_{MSE}[Å]	3kT/2ΔE
Ru III 5s^{7}S-5p^{7}P^o	10000.	0.478E-01	-0.116E-01	0.228	-0.553E-01	0.419E-01	0.207
λ = 1988.0 Å	20000.	0.338E-01	-0.821E-02	0.161	-0.391E-01	0.296E-01	0.415
	40000.	0.239E-01	-0.580E-02	0.114	-0.277E-01	0.210E-01	0.829
	80000.	0.169E-01	-0.410E-02	0.805E-01	-0.196E-01	0.148E-01	1.66
	160000.	0.119E-01	-0.290E-02	0.569E-01	-0.138E-01	0.113E-01	3.32
Ru III 5p^{7}P^o-5d^{7}D	10000.	0.495E-01	-0.684E-02	0.335	-0.462E-01		0.207
λ = 1669.2 Å	20000.	0.350E-01	-0.484E-02	0.237	-0.327E-01		0.415
	40000.	0.248E-01	-0.342E-02	0.167	-0.231E-01		0.829
	80000.	0.175E-01	-0.242E-02	0.118	-0.164E-01		1.66
	160000.	0.124E-01	-0.171E-02	0.837E-01	-0.116E-01		3.32
Ru III 5p^{7}P^o-6s^{7}S	10000.	0.102	0.422E-01	0.690	0.286		0.207
λ = 1666.2 Å	20000.	0.719E-01	0.298E-01	0.488	0.202		0.415
	40000.	0.508E-01	0.211E-01	0.345	0.143		0.829
	80000.	0.359E-01	0.149E-01	0.244	0.101		1.66
	160000.	0.254E-01	0.105E-01	0.172	0.716E-01		3.32
Ru III 5s^{5}S-5p^{5}P^o	10000.	0.747E-01	-0.178E-01	0.263	-0.626E-01	0.658E-01	0.241
λ = 2314.1 Å	20000.	0.528E-01	-0.126E-01	0.186	-0.443E-01	0.465E-01	0.483
	40000.	0.374E-01	-0.890E-02	0.131	-0.313E-01	0.329E-01	0.965
	80000.	0.264E-01	-0.629E-02	0.929E-01	-0.221E-01	0.233E-01	1.93
	160000.	0.187E-01	-0.445E-02	0.657E-01	-0.156E-01	0.184E-01	3.86
Ru III 5p^{5}P^o-5d^{5}D	10000.	0.643E-01	-0.801E-02	0.381	-0.475E-01		0.241
λ = 1782.3 Å	20000.	0.454E-01	-0.566E-02	0.269	-0.336E-01		0.483
	40000.	0.321E-01	-0.400E-02	0.191	-0.237E-01		0.965
	80000.	0.227E-01	-0.283E-02	0.135	-0.168E-01		1.93
	160000.	0.161E-01	-0.200E-02	0.953E-01	-0.119E-01		3.86
Ru III 5p^{5}P^o-6s^{5}S	10000.	0.127	0.518E-01	0.736	0.299		0.241
λ = 1806.1 Å	20000.	0.901E-01	0.366E-01	0.521	0.212		0.483
	40000.	0.637E-01	0.259E-01	0.368	0.150		0.965
	80000.	0.451E-01	0.183E-01	0.260	0.106		1.93
	160000.	0.319E-01	0.130E-01	0.184	0.748E-01		3.86

$$W(\mathring{A}) = \frac{\lambda^2}{2\pi c} W(s^{-1}), \quad (4)$$

where c is the speed of light. The corresponding relation for the shifts is analogous.

It is useful to consider regularities of Stark widths and shifts, since when they exist, we can use this for estimates of the unknown values from the known ones. Wiese & Konjević (1982) and Wiese & Konjević (1992) demonstrated that the differences between Stark widths or between shifts, expressed in angular frequency units, are less than 40% within a transitions array, namely the transition of the type nℓ - n'ℓ', where n is principal quantum number and ℓ orbital angular momentum quantum number. In the case of considered Ru III multiplets, for 5s-5p transition array the width for septet is 15.4% larger from the width of quintuplet at 10 000 K and 15.5% at 160 000 K. For the shift these values are 13.2% and 13.0% respectively. For 5p - 5d transition array these values are 13.7% and 13.9% for the width as well as 2.81% and 2.59% for the shift. In the case of 5p -6s transition array we have 6.7% and 6.98% for the width as well as 4.55% and 4.47% for the shift. In all cases these values are well within the limits of ±40% predicted by Wiese & Konjević (1982) and Wiese & Konjević (1992). We can also see that the differences are approximately the same at 10 000 K and 160 000 K. These findings can be used for the estimate of missing widths and shifts from the considered transition arrays.

CONCLUSION

With the help of SMSE theoretical method we have calculated Stark full widths at half intensity maximum and shifts for six Ru III multiplets. For two of them calculations of the line widths have

been performed also using more accurate MSE method. Comparison of MSE and SMSE values confirms that SMSE approach gives correct results even for temperatures slightly beyond the domain of validity of SMSE approach. We investigated also regularities of Stark broadening parameters within Ru III transition arrays and found that differences are within the limits of 15.5%, so that calculated values could be used to estimate the missing ones from the considered transition arrays. The Stark broadening parameters for multiplets of doubly charged ruthenium, obtained in this work, will be implemented in the STARK-B database (Sahal-Bréchot et al., 2015; Sahal-Bréchot et al., 2020) which also can be accessed through the portal (http://portal.vamdc.eu) of the European Virtual Atomic and Molecular Data Center - VAMDC (Dubernet et al., 2010; Rixon et al., 2011; Dubernet et al., 2016; Albert et al., 2020).

REFERENCES

Adelman, S. J., Bidelman, W. P. & Pyper, D. M. 1979. The peculiar A star gamma Equulei: a line identification study of lambda lambda 3086 - 3807. Astrophys. J. Suppl., 40, pp. 371-424. DOI: 10.1086/190592

Albert, D., Antony, B., Ba, Y. A., Babikov, Y.L., Bollard, P., Boudon, V., Delahaye, F., Del Zanna, G., Dimitrijević, M. S. et al. 2020. A decade with VAMDC: results and ambitions. Atoms, 8(4), pp. 76. https://doi.org/10.3390/atoms8040076

Allen, D. M. & Porto de Mello, G. F. 2007. Ruthenium and hafnium abundances in giant and dwarf barium stars. Astron. Astophys., 474, pp. 221-228. https://doi.org/10.1051/0004-6361:20066735

Beauchamp, A., Wesemael, F. & Bergeron, P. 1997. Spectroscopic Studies of DB White Dwarfs: Improved Stark Profiles for Optical Transitions of Neutral Helium. Astrophys. J. Suppl., 108, pp. 559-573. https://doi.org/10.1086/312961

Biémont, E., Grevesse, N., Kwiatkovski, M., & Zimmermann, P. 1984. Lifetime measurements for Ru I and the solar abundance of ruthenium. Astron. Astrophys, 131, pp. 364-366.

Dimitrijević, M. S. 2017. Stark widths of Sc IV spectral lines within 4s-4p transition array. The University Thought - Publication in Natural Sciences, 7(2), pp. 76-80. https://doi.org/10.5937/univtho7-15815

Dimitrijević, M. S. 2020. Stark broadening of Os II spectral lines. The University Thought - Publication in Natural Sciences, 10(2), pp. 65-70. https://doi.org/10.5937/bnsr10-27823

Dimitrijević, M. S. & Konjević, N. 1980. Stark widths of doublyand triply-ionized atom lines. J. Quant. Spectrosc. Radiative Transfer, 24, pp. 451-459. https://doi.org/10.1016/0022-4073(80)90014-X

Dimitrijević, M. S. & Konjević, N. 1987. Simple estimates for Stark broadening of ion lines in stellar plasma. Astron. Astrophys., 172, pp. 345-349.

Dimitrijević, M. S. & Kršljanin, V. 1986. Electron-impact shifts of ion lines - Modified semiempirical approach. Astron. Astrophys., 165, pp. 269-274.

Dimitrijević, M. S., & Popović, L. Č. 2001. Modified Semiempirical Method. J. Appl. Spectrosc., 68, pp. 893-901. https://doi.org/10.1023/A:1014396826047

Dimitrijević, M. S. & Sahal-Bréchot, S. 2014, On the Application of Stark Broadening Data Determined with a Semiclassical Perturbation Approach. Atoms, 2(3), pp. 357-377. https://doi.org/10.3390/atoms2030357

Dubernet, M. L., Antony, B. K., Ba, Y. A., Babikov, Yu. L., Bartschat, K., Boudon, V. et al. 2016. The virtual atomic and molecular data centre (VAMDC) consortium. J. Phys. B, 49(7), 074003. https://doi.org/10.1088/0953-4075/49/7/074003

Dubernet, M. L., Boudon, V., Culhane, J. L., Dimitrijević, M. S., Fazliev, A. Z., Joblin, C. et al. 2010. Virtual atomic and molecular data centre. J. Quant. Spectrosc. Radiative Transfer, 111(15), pp. 2151-2159. https://doi.org/10.1016/j.jqsrt.2010.05.004

Griem, H. R. 1974. Spectral line broadening by plasmas (New York.: Academic Press, Inc.)

Hansen, C. J., Andersen, & Christlieb, A. C. 2014. Stellar abundances and presolar grains trace the nucleosynthetic origin of molybdenum and ruthenium. Astron. Astrophys., 568, A47. DOI: 10.1051/0004-6361/201423535

Kramida, A., Ralchenko, Yu., Reader, J. & -NIST ASD Team 2020. NIST Atomic Spectra Database. Gaithersburg, MD: National Institute of Standards and Technology. (ver. 5.5.1), Retrived from https://physics.nist.gov/asd, 2020, 15th of September.

Merril, P. W. 1947. Atomic lines in the spectrum of R Andromedae. Astrophys. J., 105, pp. 360-375.

Milovanović, N., Dimitrijević, M. S., Popović, L. Č. & Simić, Z. 2004. Importance of collisions with charged particles for stellar UV line shapes: Cd III, Astron. Astrophys., 417, pp. 375-380. https://doi.org/10.1051/0004-6361:20034162

Mishenina, T., Pignatari, M., Gorbaneva, T., Travaglio, C., Côté, B., Thielemann, F.-K. & Soubiran, C. 2019.Enrichment of the Galactic disc with neutron-capture elements: Mo and Ru. Monthly Notices Roy. Astron. Soc., 489, pp. 1697-1708. DOI: 10.1093/mnras/stz2202

Moore, C. E. 1971. Atomic Energy Levels as Derived from the Analysis of Optical Spectra – Molybdenum through Lanthanum and Hafnium through Actinium. Nat. Stand. Ref. Data Ser. 35, Vol. III. Washington: Nat. Bur. Stand. US, pp. 1-245.

Rixon, G., Dubernet, M. L., Piskunov, N., Walton, N., Mason, N., Le Sidaner, P., et al.2011. VAMDC-The Virtual Atomic and Molecular Data Centre-A New Way to Disseminate Atomic and Molecular Data-VAMDC Level 1 Release. AIP Conf. Proc., 1344, pp. 107-115. https://doi.org/10.1063/1.3585810

Roederer, I. U., Sneden, C., Lawler, J. E. & Cowan, J. J. 2010. New abundance determinations of cadmium, lutetium, and osmiumin the r-procss enriched star BD +17 3248. Astrophys. J. Lett., 714, pp. L123-L127. https://doi.org/10.1088/2041-8205/714/1/L123

Sahal-Bréchot, S. 1969a. Impact theory of the broadening and shift of spectral lines due to electrons and ions in a plasma. Astron. Astrophys., 1, pp. 91-123.

Sahal-Bréchot, S. 1969b. Impact theory of the broadening and shift of spectral lines due to electrons and ions in a plasma (continued). Astron. Astrophys., 2, pp. 322-354.

Sahal-Bréchot, S., Dimitrijević, M. S. & Ben Nessib, N. 2014. Widths and Shifts of Isolated Lines of Neutral and Ionized Atoms Perturbed by Collisions With Electrons and Ions: An Outline of the Semiclassical Perturbation (SCP) Method and of the Approximations Used for the Calculations. Atoms, 2, pp. 225-252. DOI: 10.3390/atoms2020225

Sahal-Bréchot, S., Dimitrijević, M. S. & Moreau, N. 2020. Observatory of Paris / LERMA and Astronomical Observatory of Belgrade. Retrieved from http://starkb. obspm.fr, 2020 September 15^{th}. PHYSICS

Sahal-Bréchot, S., Dimitrijević, M. S., Moreau, N. & Ben Nessib, N. 2015. The STARK-B database VAMDC node: a repository for spectral line broadening and shifts due to collisions with charged particles. Physica Scripta, 90(5), 054008. https://doi.org/10.1088/0031-8949/90/5/054008

Simić, Z., Dimitrijević, M. S. & Kovačević, A. 2009. Stark broadening of spectral lines in chemically peculiar stars: Te I lines and recent calculations for trace elements. New Astron. Rev., 53(7-10), pp. 246-251. https://doi.org/10.1016/j.newar.2009.08.005

Simić, Z., Dimitrijević, M. S., Milovanović, N. & Sahal-Bréchot, S. 2005a. Stark broadening of Cd I spectral lines. Astron. Astrophys., 441(1), pp. 391-393. https://doi.org/10.1051/0004-6361:20052701

Simić, Z., Dimitrijević, M. S., Popović, L. Č. & Dačić, M. 2005b. Stark Broadening of F III Lines in Laboratory and Stellar Plasma. J. Appl. Spectrosc., 72(3), pp. 443-446. https://doi.org/10.1007/s10812-005-0095-4

Simić, Z., Dimitrijević, M. S., Popović, L. Č. & Dačić, M. 2006. Stark broadening parameters for Cu III, Zn III and Se III lines in laboratory and stellar plasma. New Astron. 12(3), pp. 187-191. https://doi.org/10.1016/j.newast.2006.09.001

Tankosić, D., Popović, L. Č. & Dimitrijević, M. S. 2003. The electron-impact broadening parameters for Co III spectral lines. Astron. Astrophys., 399(2), pp. 795-797. https://doi.org/10.1051/0004-6361:20021801

Wiese, W. L. & Konjević, N. 1982. Regularities and similarities in plasma broadened spectral line widths (Stark widths). J. Quant. Spectrosc. Radiative Transfer, 28(3), pp. 185-198. https://doi.org/10.1016/0022-4073(82)90022-X

Wiese, W. L. & Konjević, N. 1992.Regularities in experimental Stark shifts. J. Quant. Spectrosc. Radiative Transfer, 47(3), pp. 185-200. https://doi.org/10.1016/0022-4073(92)90028-3

Bulletin of Natural Sciences Research
Vol.11, No.1, 2021, pp. 49-53.

DOI: https://doi.org/10.5937/bnsr11-31433
Original Scientific Paper

ON SCALING OF SCHRÖDINGER EQUATION AND SOME RESULTS FOR HEAVY QUARKS MESONS

NICOLA FABIANO[1,⋆], STOJAN RADENOVIĆ[2]

[1]"Vinča" Institute of Nuclear Sciences - National Institute of the Republic of Serbia, University of Belgrade, Mike Petrovića Alasa 12–14, 11351 Belgrade, Serbia
[2]Faculty of Mechanical Engineering, University of Belgrade, Kraljice Marije 16, 11120 Beograd 35, Serbia

ABSTRACT

We consider the scaling of the Schrödinger equation in order to explicitly compute the energy density levels for a specific class of potentials. The resulting eigenvalues spectrum is compared to the heavy quarks mesons spectroscopy, showing a fair agreement with experimental data for the J/ψ and, for the heavier case Υ, an excellent agreement with the experimental data.

Keywords: Schrödinger equation, Semiclassical methods, Heavy quarks.

DETERMINATION OF THE POTENTIAL ENERGY FROM THE PERIOD OF OSCILLATION

In this paper we will consider the Schrödinger equation with a class of power law potential

$$H = \frac{p^2}{2m} + Ax^\gamma = -\hbar^2\left(\frac{d}{dx}\right)^2 + Ax^\gamma \,, \tag{1}$$

(A is a constant) whose energy eigenvalues will be compared to the ones of heavy quark mesons. Consider the energy conservation equation

$$E = \frac{m\dot{x}^2}{2} + V(x)$$

and solve for $\dot{x}$:

$$\dot{x} = \left[\sqrt{\frac{2(E - V(x))}{m}}\right] .$$

In order to obtain the period of motion we solve for dt/dx:

$$\int_0^{T(E)} dt = T(E) = 4\left(\frac{m}{2}\right)^{1/2}\int_0^{x(E)} \frac{1}{\sqrt{E - V(x)}}dx = 2(2m)^{1/2}\int_{V(0)=0}^{E} \frac{(dx/dV)}{\sqrt{E - V}}dV \,, \tag{2}$$

here $x = x(V)$ is the inverse function of the potential and we assume for simplicity that $V(0) = 0$. In order to write explicitly this integral, divide the equation by $\sqrt{\alpha - E}$ where α is a parameter such that

$$0 \le V \le E \le \alpha$$

and integrate first over the energy $\int_0^\alpha dE$ swapping integration order (Landau & Lifshitz, 1960):

$$\int_0^\alpha \frac{T(E)}{\sqrt{\alpha - E}}dE = 2(2m)^{1/2}\int_0^\alpha dV(dx/dV)\int_V^\alpha dE[(E - V)(\alpha - E)]^{-1/2} \,. \tag{3}$$

Last integral of eq. (3) in dE yields:

$$\int_V^\alpha dE[(E - V)(\alpha - E)]^{-1/2} = -2\arcsin(-1) = \pi$$

for a final result of

$$2\pi(2m)^{1/2}x(\alpha) \,.$$

Replacing α with V we obtain an expression for the shape of the potential in terms of the period

$$x(V) = \frac{1}{2\pi(2m)^{1/2}}\int_0^V \frac{T(E)}{\sqrt{V - E}}dE \,.$$

For example, if the period T is independent of energy, then

$$x(V) = C\int_0^V \frac{1}{\sqrt{V - E}}dE = 2C\sqrt{V}$$

where C is a constant. Inverting the above relation we recover the usual harmonic oscillator

$$V(x) = Ax^2$$

SEMICLASSICAL APPROACH TO QUANTUM ENERGY DENSITY LEVELS

A similar method achieves results in semiclassical approximation WKB of a symmetric monotonic potential in one dimension. Starting from the Bohr–Sommerfeld quantisation condition

$$\frac{1}{2\pi}\oint pdx = \left(n + \frac{1}{2}\right)\hbar \,, \text{ for } n = 0, 1, 2, \ldots \tag{4}$$

noticing that $\oint pdx = 2\int_a^b pdx$, where a and b are the turning points which solve the equation $E - V(x) = 0$, and working with the units where $\hbar = 1$ one has

$$\int_0^{x_0} dx[2m(E_n - V(x))]^{1/2} = \left(n + \frac{1}{2}\right)\pi \tag{5}$$

⋆ Corresponding author: nicola.fabiano@gmail.com

x_0 being the classical inversion point $V(x_0) = E$, $V(0) = 0$, and differentiating both sides with respect to n we have

$$\frac{1}{2}\int_0^{x_0}\left[\frac{2m}{E-V}\right]^{1/2}\left(\frac{\partial E}{\partial n}\right)dx = \pi\ ,$$

that could be rewritten as

$$\int_{V(0)=0}^{E} dV(dx/dV)\left[\frac{2m}{E-V}\right]^{1/2} = \frac{2\pi}{\partial E/\partial n}$$

which in form is quite similar to eq. (2), and we will proceed as before. Inserting a term $\int_0^\alpha dE(\alpha - E)^{-1/2}$ and interchanging the order of integration we find

$$\int_0^\alpha dV(dx/dV)\int_V^\alpha \frac{1}{(\alpha-E)^{1/2}(E-V)^{1/2}}dE = 2\pi\int_0^\alpha \frac{1}{[2m(\alpha-E)]^{1/2}(\partial E/\partial n)}dE\ . \tag{6}$$

The integral in dE on lhs has already been encountered in (3) and its value is π. Upon renaming $\alpha \to V$ we are left with the result

$$x(V) = 2\int_0^V \frac{1}{[2m(V-E)]^{1/2}(\partial E/\partial n)}dE = 2\int_0^V \frac{(\partial n/\partial E)}{[2m(V-E)]^{1/2}}dE \tag{7}$$

where $(\partial n/\partial E)$ is the density of eigenvalues function.

Consider for instance a constant level density, i.e. where $(\partial E/\partial n)$ is constant. Then the above integral furnishes us with the result

$$x(V) = A'\sqrt{V}$$

where A' is some constant. Inverting the relation we obtain the harmonic oscillator as expected

$$V(x) = Ax^2\ .$$

SOME NOTABLE RESULTS

The results obtained so far are valid in one dimensional quantum mechanics, therefore they also hold for symmetric central potentials for the radial part. We should recall some notable results for integrable systems.

Coulombic potential

$$V(x) = -\frac{A}{x}$$

$$E_n = -\frac{R}{n^2} \text{ implies } n(E) \sim E^{-1/2}$$

Harmonic oscillator

$$V(x) = Ax^2$$

$$E_n = \left(n + \frac{1}{2}\right)\hbar\omega \text{ implies } n(E) \sim E$$

Infinite square well

$$V(x) = 0 \text{ if } 0 < x < L, \text{ else } +\infty$$

$$E_n = Cn^2 \text{ implies } n(E) \sim E^{1/2}$$

General results

Those potentials have been listed for energy E ordered as increasing function of n.

With the knowledge of density function and main equation (7) we could infer some general results. First, with the change of variable

$$\xi = \frac{E}{V}$$

and considering the Jacobian, we are left with

$$x(V) = C\sqrt{V}\int_0^1 d\xi(1-\xi)^{-1/2}\left[\frac{\partial n(\xi V)}{\partial E}\right] \tag{8}$$

C being a constant. Now when the density function has some homogenity properties one could infer some actual results. With the power law Ansatz

$$\frac{\partial n(E)}{\partial E} \sim E^a$$

that is

$$n(E) \sim E^{a+1}$$

and inverting the relation one obtains

$$E(n) \sim n^{\left(\frac{1}{a+1}\right)}\ ,$$

$$\frac{\partial E(n)}{\partial n} \sim n^{\left(-\frac{a}{a+1}\right)}$$

for $a \neq -1$, from eq. (8) we obtain

$$x(V) = CV^{(a+\frac{1}{2})}\int_0^1 d\xi(1-\xi)^{-1/2}\xi^a = CV^{(a+\frac{1}{2})}\beta\left(\frac{1}{2}, a+1\right)\ , \tag{9}$$

which leads to

$$x(V) \sim V^{(a+\frac{1}{2})} \tag{10}$$

and inverting the equation we obtain the potential as a function of x

$$V(x) \sim x^{\left(\frac{2}{2a+1}\right)}\ . \tag{11}$$

Being a semiclassic approximation, the larger n the better agreement with the exact result is obtained.

A few examples

• For a linear potential:

$$V(x) \sim x \text{ implies } a = \frac{1}{2}$$

$$n(E) \sim E^{(3/2)}\ ;\ \frac{\partial n(E)}{\partial E} \sim E^{(1/2)}\ ;\ E(n) \sim n^{(2/3)}\ .$$

• For an anharmonic potential:

$$V(x) \sim x^4 \text{ implies } a = -\frac{1}{4}$$

$$n(E) \sim E^{(3/4)} \; ; \; \frac{\partial n(E)}{\partial E} \sim E^{(-1/4)} \; ; \; E(n) \sim n^{(4/3)} \; .$$

• For $E \sim 1/n$:

$$E(n) \sim \frac{1}{n} \text{ implies } a = -2$$

$$V(x) \sim x^{(-2/3)}$$

$$n(E) \sim E^{(-1)} \; ; \; \frac{\partial n(E)}{\partial E} \sim E^{(-2)} \; ; \; E(n) \sim n^{(-1)}$$

less singular in the origin than the Coulombic case $1/x$.

• Suppose we search a potential for which the energy density increases slightly with the energy, (that is indistinguishable from a logarithm) i.e.

$$\frac{\partial n(E)}{\partial E} \sim E^{\varepsilon}$$

where $\varepsilon > 0$ is small (the analog case with slight decrease is obtained for $\varepsilon < 0$). Then we obtain

$$V(x) \sim x^{\left(\frac{2}{1+2\varepsilon}\right)} \approx x^{2(1-2\varepsilon)}$$

$$n(E) \sim E^{(1+\varepsilon)} \; ; \; \frac{\partial n(E)}{\partial E} \sim E^{\varepsilon} \; ; \; E(n) \sim n^{\left(\frac{1}{1+\varepsilon}\right)} \approx n^{(1-\varepsilon)} \; .$$

• Observe that for the case of an infinite square well where $E \sim n^2$ the power law potential resulting from (11) has a singularity.

In table 1. we present the scaling results obtained for some power law potentials.

Table 1. Scaling for different potentials, ranging from anharmonic x^4 to Coulombic potential $1/x$.

Potential	$E(n) \sim n^{1/(a+1)}$	$\partial E/\partial n$	a
x^4	$n^{(4/3)}$	$n^{(1/3)}$	-1/4
x^2	n^1	const	0
x^1	$n^{(2/3)}$	$n^{(-1/3)}$	+1/2
x^{-1}	$n^{(-2)}$	$n^{(-3)}$	−3/2

BEYOND LEADING ORDER

The quantisation condition met in (4) is only the first order approximation of the whole WKB procedure. To summarize the method, consider the eigenvalues problem of the Schrödinger equation

$$\hbar^2 y''(x) = 2m[V(x) - E]y(x) = -p^2(x)y(x) \tag{12}$$

with the wavefunctions $y(x)$ obeying the boundary conditions $y(\pm\infty) = 0$. For the WKB procedure we will consider $\hbar$ as an expansion parameter, eventually letting its value to $\hbar \to 1$ (Bender et al., 1977). The series expansion for the wavefunction is given by

$$y(x) = \exp\left[\frac{1}{\hbar}\sum_{k=0}^{+\infty}\hbar^k S_k(x)\right] , \tag{13}$$

plugging back (13) in (12) and comparing the coefficients of the same power of $\hbar$ one obtains the equation

$$S_0'(x) = [-p^2(x)]^{1/2} \tag{14}$$

together with the recursive relation valid for any order of $S_k(x)$:

$$2S_0'S_k' + \sum_{j=1}^{k-1} S_j'S_{j-k}' + S_{k-1}'' = 0 \text{ , for } k \geq 0 \; . \tag{15}$$

The first computed terms up to $O(\hbar^3)$ are given by

$$S_1' = -\frac{1}{2}\frac{p'}{p} = -\frac{1}{2}(\ln p)' \; , \tag{16}$$

$$S_2' = -\frac{i}{8p^3}\left[2pp^{(2)} + 3(p')^2\right] \; , \tag{17}$$

$$S_3' = \frac{1}{16p^6}\left[2p^3p^{(4)} - 16p^2p'p^{(3)} - 10p^2(p^{(2)})^2 + 67p(p')^2p^{(2)} - 45(p')^4\right] \; . \tag{18}$$

Once solved for $S_k'(x)$ one obtains a generalization of the formulæ (4),(5) to all orders of WKB expansion:

$$\frac{1}{2i}\oint\sum_{k=0}^{+\infty} S_k(x)'dx = n\pi \; . \tag{19}$$

For the energy eigenvalues of the power law potential (1) one obtains the following result (Parisi G. in: Chudnovsky & Chudnovsky, 2006) in the limit $n \to +\infty$

$$E_n = n^{2\gamma/(\gamma+2)}\left[C_0 + \frac{C_1}{n^2} + O\left(\frac{1}{n^4}\right)\right] \; , \tag{20}$$

where C_0, C_1 are constants. Observe that the first term coincides with the results obtained in Section (**Some Notable Results**).

RELATION TO HEAVY MESONS

In order to verify the results obtained so far, we will make use of a comparison to the values of some heavy meson states. It is well known that (Fabiano, 1998) heavy mesons, i.e. $q\overline{q}$ states can be well described by an effective radial potential $V(r)$ in a Schrödinger equation

$$H\psi = \left[-\frac{\nabla^2}{2\mu} + V(r)\right]\psi = E\psi \; , \tag{21}$$

μ being the reduced mass of the state, mimicking the QCD phenomenology, incorporating short distance behaviour, that is approaching a Coulombic potential for $r \to 0$, and long distance behaviour, approaching a linear nonperturbative term due to QCD confinement for large values of r. The heavier the meson, the closer the $q\overline{q}$ pair orbits together, and is better described by a semiclassical picture. Moreover, the relativistic effects are less relevant in those heavier cases (Fabiano, 2001).

The mass of an nS quark bound state is given by the expression (Fabiano, 1998)

$$M(n) = 2m + E(n) \tag{22}$$

$M(n)$ being the mass of the n level bound state, m the quark mass and $E(n)$ the binding energy of the state. We will make use of the results obtained in Section (**Some Notable Results**) for a power

law potential and make a fit to J/ψ and Υ nS states and their excitations as a function of $n = 1 \ldots 4$, with data provided in (Particle Data Group et al., 2020; Barnes, 2006). The power law potential will average between the two behaviours depicted above, for small and large values of the quark–antiquark distance r, providing a kind of "effective potential". Our aim is not to introduce another power law potential (see (Fabiano, 1998) and references therein for a partial list), but rather to verify the validity of the WKB procedure and its accuracy within the approximation order considered and when n is not going to infinity.

Beginning with J/ψ state we have the following results for the mass of its excited levels nS as a function of the quantum number n, together with the first order approximation fit obtained for a power law potential presented in fig. 1.

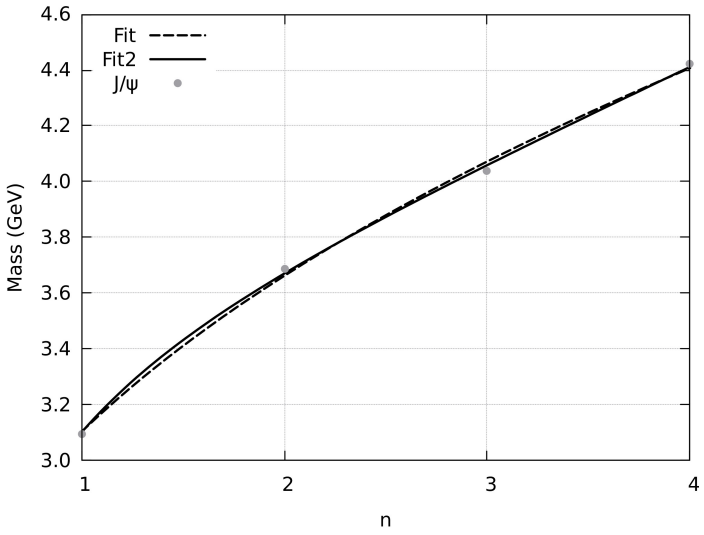

Figure 1. J/ψ nS states mass and fit of a power law potential as a function of n, for first (Fit) and second order energy spectrum (Fit2)

The resulting energy scaling and potential from the J/ψ fit is given by

$$E(n) \sim n^{0.413} \text{ yields } V(r) \sim r^{0.520} . \tag{23}$$

The other fit parameters from equations (20) and (22) are $m = 0.706$, $\gamma = 0.520$, $C_0 = 1.690$.

Comparing the results obtained for the J/ψ excited states in fig. 1. we can see that the second order approximation gives a more accurate fit than the first order one, as expected. The second order approximation curve is even closer to the experimental values, almost passing through all data points. The resulting energy scaling and potential from the J/ψ fit with a second order approximation is given by

$$E(n) \sim n^{1.398} \text{ yields } V(r) \sim r^{4.643} , \tag{24}$$

which is rather different from the previous results of the first order, showing that to achieve a better accuracy for the J/ψ states effective potential some relativistic effects should be considered as well. The other fit parameters are $m = 2.058$, $\gamma = 4.643$, $C_0 = 0.113$, $C_1 = -1.130$. Because of its relatively low mass the J/ψ state is not completely a "nonrelativistic state" (Fabiano, 1998, 2001) as discussed above.

Concerning the semiclassical approximation, as there are four experimental points, it is not possible to proceed further in the approximation order of (20) as there would be more variables than data points, leaving some of them with arbitrary values, leading to multiple (maybe infinitely many) solutions that fit the data equally well, that is a so called "underdetermined" problem. Another remark is that as the fit for equation (22) is not given by a polynomial function, even if there are an equal number of variables and points, there is no guarantee that the fit will pass exactly though all those points.

For the Υ state and its nS excitations, and the fit for a power law potential we obtain the results shown in fig. 2.

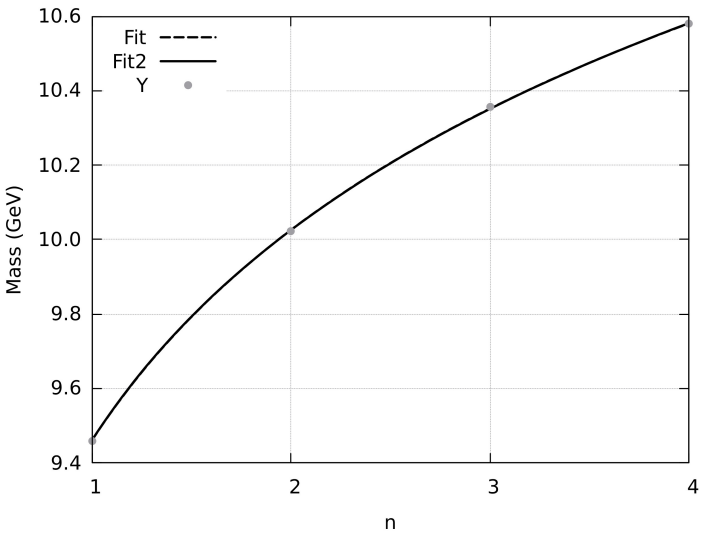

Figure 2. Υ nS states mass and fit of a power law potential as a function of n, for first (Fit) and second order energy spectrum (Fit2)

The resulting energy scaling and effective potential from the Υ fit at first order approximation is given by

$$E(n) \sim n^{0.011} \text{ yields } V(r) \sim r^{0.011} . \tag{25}$$

The other fit parameters from equations (20) and (22) are $m = -33.448$, $\gamma = 0.011$, $C_0 = 76.359$.

The comparison of the Υ excited states in fig. 2. shows a different scenario with respect to the J/ψ one of fig. 1.: the result of first order approximation is already a very good one, as it completely overlaps with the experimental points. The second order approximation is virtually indistinguishable from the first one. The resulting energy scaling and potential from the Υ fit with a second order approximation is given by

$$E(n) \sim n^{0.017} \text{ yields } V(r) \sim r^{0.017} , \tag{26}$$

which is quite close to the one obtained by the first order approximation. The other fit parameters are $m = -18.159$, $\gamma =$

0.017, $C_0 = 45.807$, $C_1 = -0.028$. Therefore, the Υ states actually behave like "nonrelativistic semiclassical states", providing with an excellent agreement with the energy levels and a good approximation for the purely power law potential.

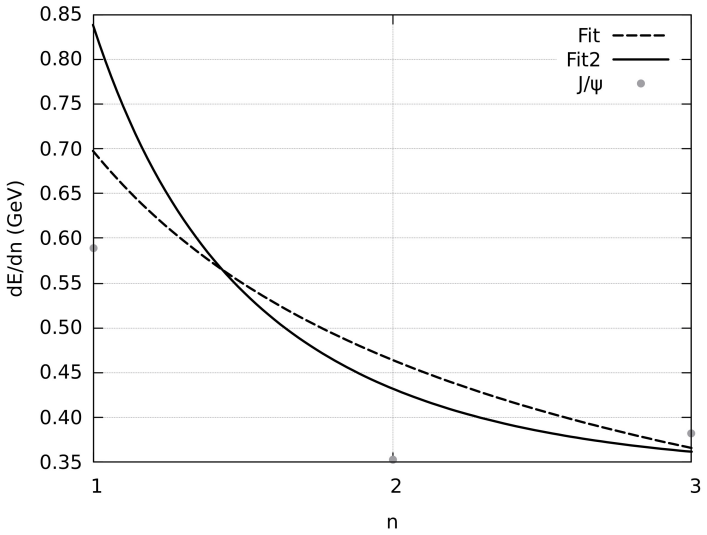

Figure 3. Derivative of J/ψ nS energy levels with respect to n and fit of a power law potential as a function of n, for first (Fit) and second order energy spectrum (Fit2)

We therefore evince from figs 1. and 2. that there is a good agreement with the J/ψ data and an excellent agreement with the Υ states, and the latter behaves, as expected because much heavier, more like a nonrelativistic semiclassical system. The lower exponent of the power law potential in the latter case is also to be expected, as could be seen in table 1.

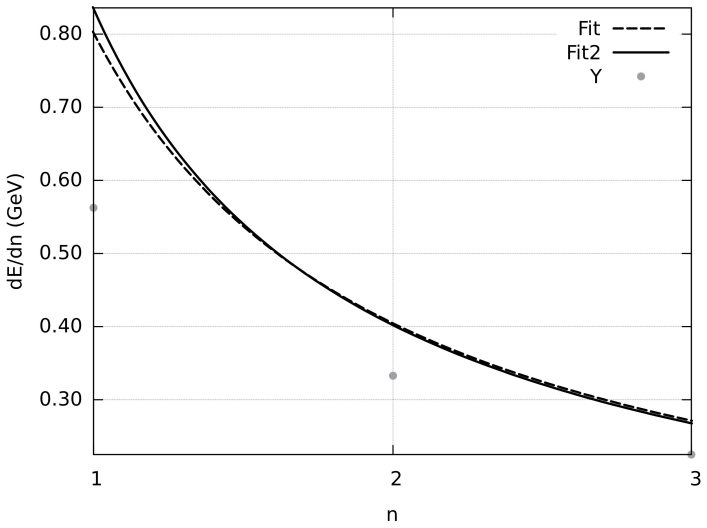

Figure 4. Derivative of Υ nS energy levels with respect to n and fit of a power law potential as a function of n, for first (Fit) and second order energy spectrum (Fit2)

Then we consider the derivative of the density of states $\partial E/\partial n$. The data for nS excited states of J/ψ and Υ can not provide us with a proper derivative, but rather with a discrete approximation of energy differences divided by unitary step, $\Delta n = 1$. This should suffice for our analysis, where we compare the results obtained from the experimental data to the fitted curve of eq. (22) once taken the derivative with respect to n.

Starting from the J/ψ excitations from fig. 3. one could observe that, even if the two fits do not meet the experimental points (as expected because they are not proper derivatives) they both reproduce the behaviour of the points as a function of n, with the second order approximation being closer to the data.

For the Υ case the same reasoning of the J/ψ case is valid. This time however there is almost not difference between first and second order approximation as expected, and the agreement with the experimental points is also better fig. 4.

CONCLUSIONS

We have considered the behaviour of the energy spectrum of a Schrödinger equation with a particular class of potential. The results for the energy levels have been obtained with the aid of the WKB technique. The spectrum has been compared to the heavy meson nS states of J/ψ and Υ providing, at least for the energy levels, respectively a very good and an excellent agreement with data, even though the quantum number n does not tend to infinity and is not very high either. We have checked the validity of the WKB results used even when not employing a high approximation order. Those results prove once more the validity and the accuracy of the Schrödinger equation approach for a phenomenological description of some QCD phenomena.

REFERENCES

Barnes, T. 2006, The XYZs of charmonium at BES, International Journal of Modern Physics A, 21(27), pp. 5583-5591. https://doi.org/10.1142/S0217751X0603477X

Bender, C. M., Olaussen, K., & Wang, P. S. 1977, Numerological analysis of the WKB approximation in large order, Physical Review D, 16(6), pp. 1740.

Fabiano, N. 1998, Top Mesons, The European Physical Journal C-Particles and Fields, 2(2), pp. 345-350.

Fabiano, N. 2001, Estimates of threshold cross section for stoponium production at e+e- colliders, The European Physical Journal C-Particles and Fields, 19 (3), pp. 547-551. https://doi.org/10.1007/s100520100638

Landau, L. D. & Lifshitz, E. M. 1960, Mechanics. Vol. 1 of: Course of Theoretical Physics, Pergamon Press Ltd.

Parisi G. in: Chudnovsky, D. & Chudnovsky, G. 2006, The Riemann Problem, Complete Integrability and Arithmetic Applications: Proceedings of a Seminar Held at the Institut Des Hautes Etudes Scientifiques, Bures-sur-Yvette, France and at Columbia University, NY, USA, 925, pp. 1979-1980. Springer

Particle Data Group, Zyla, P. A., & Barnett, R. M. 2020, Review of Particle Physics, Progress of Theoretical and Experimental Physics, 2020(8), https://doi.org/10.1093/ptep/ptaa104

CIP - Каталогизација у публикацији
Народна библиотека Србије, Београд

5

BULLETIN of Natural Sciences Research / editor in chief Branko V. Drljača. - [Štampano izd.]. - Vol. 10, no. 2 (2020)- . - Kosovska Mitrovica : Faculty of Sciences and Mathematics, University of Priština, 2020- (Kruševac : Sigraf). - 29 cm

Polugodišnje. - Je nastavak: The University thought. Publication in natural sciences = ISSN 1450-7226. – Drugo izdanje na drugom medijumu: Bulletin of Natural Sciences Research (Online) = ISSN 2738-1013
ISSN 2738-0971 = Bulletin of Natural Sciences Research (Štampano izd.)
COBISS.SR-ID 28586505

Available Online

This journal is available online. Please visit http://www.bulletinnsr.com to search and download published articles.